ABSTRACT

GAS FLUIDIZATION OF NANOPARTICLES

by
Qun Yu

The primary objective of this study is to perform a systematic investigation on the gas fluidization of various nanoparticle agglomerates. Firstly, the gas fluidization characteristics and regime classifications without any additional external force fields are identified using both experimental measurements and modeling. Secondly, the effect of introducing certain external force fields on nanoparticle fluidization is experimentally investigated. Two external force fields were applied: sound waves from a loud speaker (acoustic assistance) and in-bed magnets that were excited by an external oscillating magnetic field (magnetic assistance). Thirdly, exploratory experimental research on the use of nanoparticle agglomerates as a granular filtration media for airborne fine particles is conducted. The last part of this dissertation is an exploratory modeling study to interpret the newly-found core-annulus-wall flow structure in gas fluidization.

The experimental study on the gas fluidization of nanoparticles shows that most nanoparticles can be fluidized in the form of nanoparticle agglomerates. For those agglomerates (fluffy carbon black and very large agglomerates) that are difficult to fluidize, channeling always occurs. For those nanoparticle agglomerates that can be fluidized, the fluidization behaviors can be classified into two general categories, namely, agglomerate particulate fluidization (APF) and agglomerate bubbling fluidization (ABF). The classification appears to be depend mainly on the primary nanoparticle size and the bulk density.

Nanoparticle agglomerates have a special structure with extremely high porosity. In this study, an analytical model is developed to calculate the flow partition through and around the porous agglomerates, as well as the drag force on an agglomerate of nanoparticles in a swarm of other similar agglomerates. Also, an analytical model based on the Richardson-Zaki equation has been developed to predict the fluidizing agglomerate size, the voidage around the agglomerates, and the minimum fluidization velocities of APF nanoparticles.

The introduction of an external field such as sound excitation and magnetic excitation with in-bed magnets can significantly change the fluidization characteristics of nanoagglomerates, including a significant reduction in the minimum fluidization velocity and agglomerate size. The intensity and frequency of the external sound and magnetic fields will influence the fluidization quality of the nanoparticles.

In this study, a series of exploratory experiments have been conducted to remove sub-micron particles (including solid particles and liquid droplets) generated by burning incense. The results show that nanoparticle agglomerates in a packed bed can be used successfully as a filter media for airborne submicron particulates.

In addition, this study interprets the formation mechanism of the recently discovered core-annulus-wall structure in a circulating fluidized bed, which originates from the wall region mixing of a down flow of solids from the top section of a riser and the upward solids flow near the bottom of the riser, and the strong solid particle collisions in the dense phase suspension. A mathematic model of this phenomenon has been successfully developed and solved numerically.

GAS FLUIDIZATION OF NANOPARTICLES

by
Qun Yu

A Dissertation
Submitted to the Faculty of
New Jersey Institute of Technology
in Partial Fulfillment of the Requirements for the Degree of
Doctor of Philosophy in Mechanical Engineering

Department of Mechanical Engineering

May 2005

APPROVAL PAGE

GAS FLUIDIZATION OF NANOPARTICLES

Qun Yu

Dr. Chao Zhu, Dissertation Advisor Date
Associate Professor of Mechanical Engineering, NJIT

Dr. Rajesh N. Dave, Dissertation Co-Advisor Date
Professor of Mechanical Engineering, NJIT

Dr. Robert Pfeffer, Committee Member Date
Distinguished Professor of Chemical Engineering, NJIT

Dr. Teh C. Ho, Committee Member Date
Senior Research Associate, ExxonMobil R&D Corporation, Annandale, NJ

Dr. Rong-Yaw Chen, Committee Member Date
Professor of Mechanical Engineering, NJIT

BIOGRAPHICAL SKETCH

Author:	Qun Yu
Degree:	Doctor of Philosophy
Date:	May 2005

Undergraduate and Graduate Education:

- Doctor of Philosophy in Mechanical Engineering,
  New Jersey Institute of Technology, Newark, NJ, USA, 2005
- Master of Engineering in Experimental Mechanics,
  Dalian University of Technology, Dalian, P.R. China, 1996
- Bachelor of Engineering in Engineering Mechanics,
  Dalian University of Technology, Dalian, P.R. China, 1993

Major: Mechanical Engineering

Presentations and Publications:

Yu Q., Quevado J., Pfeffer R., Dave R., Zhu C.,
"Enhanced Fluidization of Nanoparticles in an Oscillating Magnetic Field,"
AIChE Journal, 51 (2005), 1-9.

Zhu C., Yu Q., Pfeffer R., Dave R.,
"Gas Fluidization Characteristics of Nanoparticle Agglomerates,"
AIChE Journal, 51(2005), 426-439.

Zhu C., Liu G., Yu Q., Pfeffer R., Dave R., Nam C.,
"Sound Assisted Fluidization of Nanoparticle Agglomerates,"
Powder Technology, 141 (2004) 119-123.

Dukhin S., Zhu C., Dave R., Yu Q.,

"Hydrodynamic Fragmentation of Nanoparticle Aggregates at Orthokinetic Coagulation,"

Advances in Colloid and Interface Science, in press.

Yu Q., Zhu C., Pfeffer R., Dave R.,

"Modeling on Agglomerate Particulate Fluidization of Nanoparticles: Determination of Agglomerates Size and Internal Structure,"

Circulating Fluidized Bed VIII, May 10-13, 2005, Hangzhou, China.

Zhu C., Yu Q., Fan L.S.,

"Modeling on Core-Annulus-Wall Structure in Circulating Fluidized Bed Riser,"

Circulating Fluidized Bed VIII, May 10-13, 2005, Hangzhou, China.

Pfeffer R., Dave N., Zhu C., Yu Q., Quevado J., Nam C.,

"Fluidization of Nanoparticle Agglomerates with the Assistance of Magnetic Particles in an Oscillating Magnetic Field,"

2005 NSF Design, Service and Manufacturing Grantees and Research Conference, January 3-6. 2005, Scottsdale, Arizona, USA.

Yu Q., Zhu C., Fan L.S., Du B.,

"Modeling on Core-Annulus-Wall Structure in Circulating Fluidized Bed Riser near Choking,"

the Ninth Asian Conference on Fluidized-Bed and Three-Phase Reactors, November 21-24, 2004, Wanli, Taiwan.

Yu Q., Zhu C., Pfeffer R., Dave R.,

"Fluidization Characteristics of Nanoparticle Agglomerates,"

the Ninth Asian Conference on Fluidized-Bed and Three-Phase Reactors, November 21-24, 2004, Wanli, Taiwan.

Yu Q., Quevado J., Nakamura H., Dave R., Pfeffer R., Watano S., Zhu C.,

"Fluidization of Nanoparticles under Magnetic or Centrifugal Fields,"

2004 AICHE Annual Meeting, November 7-12, Austin, TX, USA.

Yu Q., Zhu C., Pfeffer R., Dave R.,
"Experimental Study on Fluidization Characteristics of Nanoparticles,"
Proceedings of HTFED04 2004 ASME Heat Transfer/Fluids Engineering Summer Conference, July 11–15, 2004, Charlotte, NC, USA.

Rafique Q., Lee T., Yu Q., Zhu C.,
"Measurements of Gas Entrainment in Evaporating Spray Jets,"
Proceedings of HTFED04 2004 ASME Heat Transfer/Fluids Engineering Summer Conference, July 11–15, 2004, Charlotte, NC, USA.

Liu G., Yu Q., Zhu C., Pfeffer R., Dave R.,
"Fluidization Characteristics of Nanoparticle Agglomerates in Acoustic Fields,"
2004 PARTECH Annual Meeting, March 16-18, 2004, Nurenburg, Germany.

Liu G., Yu Q., Zhu C., Pfeffer R., Dave R.,
"Sound-Assisted Fluidization of Nanoparticles,"
2003 AICHE Annual Meeting, November 16-21, 2003 San Francisco, CA, USA.

Ryu Y. S., Ji Z., Yu Q.,
"Application of Learning Control to a Robotic Arm for Exercises,"
2002 ASME International Mechanical Engineering Congress and Exposition, November 17-22, 2002, New Orleans, Louisiana, USA.

Chen J., Gong Z., Qu M., Yu Q., Qu Y., Fang D.,
"Effect of Vibratory Welding on Mechanical Properties of Welding Lines,"
Journal of Dalian University of Technology, China, 41(2005) 1-5.

Chen J., Yu Q., Fang D.,
"The Research on Vibratory Welding to Release Residual Stress and Reduce Distortion of Mechanical Components,"
9th China National Experimental Mechanics Conference, November 1998, Guangzhou, China.

This dissertation is dedicated to my father Liangqing Yu, who passed away in 1995 before my graduation with Master's degree, my mother Xuewen Cheng, and my beloved wife Fei Jin.

ACKNOWLEDGMENT

I wish to express my sincere appreciation to my advisors Dr. Chao Zhu and Dr. Rajesh N. Dave, and Dr. Robert Pfeffer, for their remarkable guidance, constant supervision, friendship and moral support throughout this research. Without their guidance, it would have been impossible to finish this program so smoothly. Special thanks are given to Dr. Teh C. Ho, Dr. Rong-Yaw Chen, for their active participation in my dissertation committee. I am also thankful to Dr. L. S. Fan at Ohio State University for his valuable suggestions in this study.

I am grateful to the supported from Graduate Office and Mechanical Engineering Department of New Jersey Institute of Technology for TA Scholarships, from New Jersey Center for Engineered Particulates (NJECP) for Summer RA Scholarship, from National Science Foundation for financial support through Grant # 0210400, NIRT - Collaborative Research: Experimental and Computational Investigations of Fluid Interactions/Transport in Nanodomains and Around Nanoparticles, and from ExxonMobil R&D Incorporation and Petroleum Research Fund for the research fund. I also appreciate the friendship and cooperation of Dr. S. Dukhin, Dr. Guangliang Liu, Dr. Caroline H. Nam, Mr. Jose A. Quevedo, Mr. Yueyang Shen and Dr. Jun Yang during this study.

I would like to express my endless gratitude to my parents, Liangqing Yu who passed away ten years ago, and Xuewen Cheng, who has always supported my academic pursuits and helped me in every possible way. Last, I would like to say most sincere thanks to my lovely wife, Fei Jin, for her love and encouragement throughout these years.

TABLE OF CONTENTS

TABLE OF CONTENTS
(Continued)

TABLE OF CONTENTS
(Continued)

TABLE OF CONTENTS
(Continued)

TABLE OF CONTENTS
(Continued)

TABLE OF CONTENTS
(Continued)

Chapter **Page**

LIST OF TABLES

LIST OF TABLES
(Continued)

LIST OF FIGURES

LIST OF FIGURES
(Continued)

LIST OF FIGURES
(Continued)

Figure **Page**

LIST OF FIGURES
(Continued)

LIST OF FIGURES
(Continued)

LIST OF FIGURES
(Continued)

LIST OF NOMENCLATURE

a	agglomerate radius
A	area
A_s	cross-section area of a solid particle
C_D	drag coefficient for solid sphere in gas flow
d_a	average size of fluidized agglomerates
d_s	average size of solid particles
d_{sub}	average size of subagglomerates
d_t	diameter of vessel (chamber)
D_s	solid diffusion coefficient
e	restitution coefficient
F_{Dp}	drag force exerted on a permeable sphere in a swarm of permeable spheres
F_{Ds}	drag force exerted on a solid sphere in a swarm of solid spheres
F_f	force due to energy dissipation
Fr_{mf}	Froude number at minimum fluidization velocity, $Fr_{mf} = \frac{u_{mf}^2}{d_a g}$,
g	gravitational constant
g_0	radial distribution function, $g_0=1.0$
H	height of fluidized bed
H_0	initial height of bed
H_{mf}	bed height at minimum fluidization velocity
k	permeability of porous sphere
k'	solid convention coefficient
l'	inter-particle distance, center to center
$\dot{m}_s$	solid transportation across interface
$\dot{M}_g$	gas-feeding rate
$\dot{M}_s$	solid-feeding rate
n	exponent in the Richardson-Zaki equation
P	pressure
Re_{mf}	Reynolds number at minimum fluidization velocity
T_c	granular temperature
U_g	superficial gas velocity
U_{pt}	terminal velocity for a single agglomerate
U_{mf}	minimum fluidization velocity of agglomerates
Us	solid particle velocity
$U's$	solid particle velocity flutuation
V	superficial fluid velocity for the swarm
z	bed height
dP/dZ	pressure drop
α_s	solid concentration
β	permeability related dimensionless radius of sphere
β'	pressure drop partition due to energy dissipation
γ	kinetic energy dissipation rate

δ	pressure drop partition due to solid holdup
η	a bed voidage dependent parameter, dimensionless, $\eta = (1-\varepsilon_g)^{1/3}$
ε_g	volume fraction of gas in fluidized bed
ε_{g0}	initial volume fraction of gas in fluidized bed
ε_{gmf}	volume fraction of gas in fluidized bed at the minimum fluidization velocity
$\varepsilon_{g,sub}$	volume fraction of gas around sub-agglomerates in a single agglomerate
μ	viscosity of fluid
ρ	density
ρ_a	density of agglomerate in fluidized bed
ρ_{a0}	initial density of agglomerate in fluidized bed
ρ_b	bulk density of bed
ρ_g	density of gas
ρ_m	material density of primary particle
χ	pressure drop partition due to solid particle acceleration
Ω_p	drag force correction factor for permeable spheres in a swarm of permeable spheres
Ω_s	drag force correction factor for solid spheres in a swarm of solid spheres
Ω	ratio of F_{Dp} to F_{Ds}, $\Omega \equiv \frac{F_{Dp}}{F_{Ds}} = \frac{\Omega_p}{\Omega_s}$
Π	$Fr_{mf}\,\mathrm{Re}_{mf}\,\frac{\rho_a-\rho_g}{\rho_g}\,\frac{H_{mf}}{d_t}$

Subscripts

0	initial
a	annulus region
agg	agglomerate
b	bulk
c	core region
g	gas phase
p	permeable
pt	particle terminal
s	solid phase
sub	sub-agglomerate
w	wall region

CHAPTER 1

INTRODUCTION

1.1 Background and Dissertation Structure

Gas fluidization of small solid particles has been widely used in a variety of industrial applications because of its unusual capability of continuous powder handling, good mixing, large gas-solid contact area and very high rates of heat and mass transfer. Extensive research has been done in the area of gas fluidization, and the fluidization behavior of classical powders in the size range of 30 to 1000 μm (such as Geldart group A and B powders) is relatively well understood (Fayed and Otten, 1997; Fan and Zhu, 1998). However, the fluidization behavior of ultrafine particles, including nanoparticles, is much more complex and has received relatively little attention in the literature.

Because of their unique properties of very small primary particle size and very large surface area per unit mass, nanostructured materials are already being used in the manufacture of drugs, cosmetics, foods, plastics, catalysts, energetic and bio materials and in mechatronics and micro-electro-mechanical systems (MEMS) (Jung and Gidaspow, 2002; Wang *et al.,* 2002a; Nam *et al.,* 2004). Therefore, it is necessary to develop processing technologies, which can handle large quantities of nanosized particles, e. g., mixing, transporting, modifying the surface properties (coating) and downstream processing of nanoparticles to form nano-composites. But before processing of nanostructured materials can take place, the nanosized particles have to be well dispersed. Gas fluidization is one of the best techniques available to disperse and process powders belonging to the Geldart group A and B classifications. Based on their primary particle size and material density, nanosized powders, however, fall under the Geldart group C (<30 microns) classification, which means that fluidization is expected to be difficult due to cohesive forces that become more prominent as the particle size decreases, as shown in Figure 1.1.

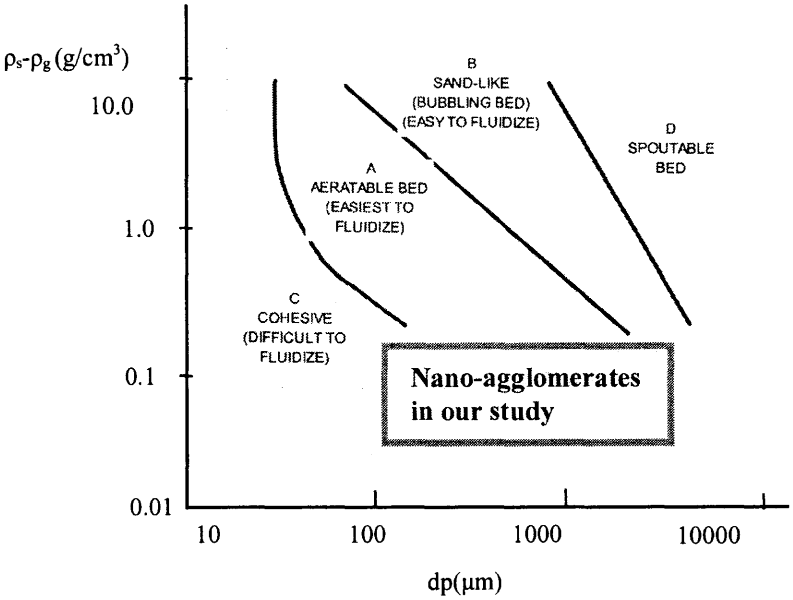

Figure 1.1 Geldart's classification on fluidizing particles.

Due to the strong interparticle forces such as van der Waals, electrostatic and moisture-induced surface tension forces, nanoparticles are always found to be in the form of large-sized agglomerates, rather than as individual nano-sized particles in a gaseous medium. Hence, gas fluidization of nanoparticles actually refers to the fluidization of nanoparticle agglomerates.

However, only limited and scattered experimental data on the fluidization characteristics, such as the minimum fluidization velocity, agglomerate size, hysteresis effects, and effect of nanoparticle material properties, are available (Jung and Gidaspow, 2002; Wang *et al.,* 2002a; Nam *et al.,* 2004), which calls for a systematic experimental study over a wide spectrum of nanoparticle materials. Moreover, since the fluidization of nanoparticle agglomerates is a relatively new research area, although several researchers made some modeling efforts (Jung and Gidaspow, 2002; Wang *et al.,* 2002a; Nam *et al.,* 2004), the theoretical studies in this area are still in the early stage, especially the hydrodynamic analysis of highly porous nanoparticle agglomerates.

For the same reason, studies on new techniques to improve the fluidization quality of nanoparticles, and potential applications of nanoparticles (in the dry state) utilizing their unique properties, are also in an early stage, and demand more research efforts.

Hence, this dissertation firstly aims to conducting a systematic study of gas fluidization of nanoparticle agglomerates using a wide range of different nanoparticles by means of both experimental and modeling approaches, which will be included in Part I; secondly, the effects of external excitations, particularly the effect of sound and magnetic assisted fluidization, are experimentally investigated in Part II; and thirdly, in Part III, a preliminary experimental study is carried out on filtration of airborne submicron particles (burning incense) using the fractal nanoparticle agglomerates as a granular filtration medium; and fourthly, to further understand the general structure in circulating fluidization systems, a preliminary mechanistic modeling is proposed and discussed in Part IV. Finally, conclusions are drawn in the last part, and future research directions are proposed as well.

1.2 Conventional Fluidization of Nanoparticles

Because of the limited and scattered experimental data on the fluidization behavior, one of the primary objectives of this study therefore is to experimentally determine the fluidization characteristics of a variety of different nanoparticles and to correlate the macroscopic fluidization behavior of the nanoagglomerates with the properties of the primary nanoparticles in a conventional gravity-driven fluidized bed without any additional external forces present. For nanoparticles which can be fluidized, Wang *et al.* (2002a) have already classified them as either agglomerate particulate fluidization (APF) or agglomerate bubbling fluidization (ABF), but the complete fluidization characteristics have never been investigated in a systematic manner. Therefore, in this study, the fluidization characteristics of both APF and ABF nanoparticles, such as the minimum fluidization velocity, agglomerate size, hysteresis effects, and effect of nanoparticle material properties, are systematically studied

Another task is to develop a simple and effective method to estimate the average size of the agglomerates and the bed voidage around the agglomerates which can then be used in models to determine the minimum fluidization velocity, pressure drop and other pertinent variables of the fluidization process.

The classical Richardson-Zaki equation is based on the hydrodynamic force analysis of solid particles in a liquid; however, nanoparticle agglomerates are hollow structures with typical porosities up to 98% or higher (Jung and Gidaspow, 2002; Wang *et al.*, 2002a; Nam *et al.*, 2004). While it may be assumed that nanoparticle agglomerates in fluidization behave similarly to solid particles of the same size and bulk density in published model approaches, a rigorous hydrodynamic analysis of nanoparticle agglomerate fluidization has not yet been done. Therefore this study is also aimed to provide an analysis of flow partition through and around an agglomerate of nanoparticles during fluidization as well as the resulting hydrodynamic force on the agglomerate. A simple model is also developed to estimate the size and minimum fluidization velocity of nanoparticle agglomerates, which is also validated experimentally. All of the work on conventional fluidization of nanoparticle agglomerates is included in Part I.

1.3 Fluidization of Nanoparticles with External Excitation

In addition to conventional gravity-driven fluidization, nanoparticle agglomerates can also be fluidized in a rotating or centrifugal fluidized bed where the centrifugal force acting on the agglomerates can be set much higher than gravity (Quevado *et al.*, 2005, in preparation). It is also found that the minimum fluidization velocity of nanoparticle agglomerates in a conventional fluidized bed can be significantly reduced by introducing external force excitations to the bed, such as vertical, sinusoidal vibration, (Nam *et al.*, 2004).

So far all studies on sound-assisted fluidization have been focused on the fluidization of micron or sub-micron sized particles (Chirone *et al.*, 1994; Levy *et al.*, 1997) No results have been reported on the effects of sound on the fluidization of nanoparticle agglomerates. This study presents an investigation of sound-assisted fluidization of nanoparticle agglomerates and their fluidization characteristics, which are not only different from those observed using other fluidization enhancement methods for nanoparticle agglomerates, but are also different from sound-assisted fluidization of micron or sub-micron sized particles. The effects of sound frequency and sound pressure level on the fluidization behavior, such as the minimum fluidization velocity, the bubbling regime, pressure drop across the bed, and bed expansion, is demonstrated.

All previous studies of improving fluidization by applying magnetic excitation with in-bed magnetic particles have been conducted on micron-sized particles where the magnetic particles are also fluidized (Filippov, 1960; Arnaldos *et al.*, 1985; Liu *et al.* 1991; Saxena *et al.,* 1994). To our knowledge, no one has studied the effect of adding large magnetic particles to a bed of nanoparticles, which do not fluidize, but serve to disrupt the interparticle forces between the nanoparticles, so that smooth fluidization of nanoagglomerates can occur. Therefore, another objective of this study is to experimentally determine the fluidization behavior of both APF and ABF nanosized particles by applying an oscillating magnetic field to the nanoparticles that have been premixed with some very large magnetic particles. It is anticipated that the excitation of the magnets will provide sufficient energy to the system to overcome the interparticle forces and form stable smaller agglomerates that will fluidize smoothly at a lower minimum fluidization velocity.

This study presents an investigation of the fluidization behavior of nanoparticle agglomerates with the assistance of millimeter-sized magnetic particles excited by an oscillating magnetic field. The effects of the intensity and frequency of the oscillating magnetic field and the weight of magnets, on important fluidization parameters such as the minimum fluidization velocity, pressure drop across the bed, and bed expansion, are demonstrated. The fluidization of nanoparticle agglomerates with external excitations are discussed in Part II.

1.4 Nanoparticle Filtration

It is well known that submicron size particles (0.1 to 1 μm) are the most difficult to filter, and are commonly known as the most penetrating particle size (MPPS) (Tardos *et al.*, 1979; Flagen and Seinfeld, 1988; Tien, 1989). The nanoagglomerates which are formed during fluidization are hierarchical fractal structures consisting of sub-agglomerates or aggregates at a number of different length scales (Wang *et al.,* 2002a; Nam *et al.,* 2004), and based on this fact, it occurred to us that they should behave as an ideal filter media to remove particles (solid and liquid) from industrial gas streams, especially MPPS. The nanoagglomerates are relatively large in size, which would result in a low gas pressure drop; they are extremely porous with an overall internal porosity greater than 0.99 which suggests that some of the "dusty" gas would flow through them; and if used for filtering liquid particles (mists) that wet their surface, they would act as a sponge and suck in the liquid drops by capillary action. Best of all, because of the relatively large distance between adjacent nanoagglomerates (high external porosity), they should act as a deep bed filter (unlike fiber-based HEPA filters) without surface cake formation, which invariably causes HEPA filters to clog rather quickly (Penicot *et al.,* 1999).

Based on these favorable properties and structure, it is anticipated that the nanoagglomerates will perform well (high collection efficiency) as fiber media for filtration of submicron particles and liquid droplets in gas stream. In this study, a set of preliminary experiments has demonstrated the validity of these ideas; these are described in Part III.

1.5 Core-Annulus-Wall Model for General CFB Riser Flows

Recent experimental studies using Electrical Capacitance Tomography (ECT) show that there exists a double ring structure in solids concentration in a circulating fluidized bed riser (Du *et al.*, 2004). It was found that the solid concentrations at the dense core region can be as high as five times those at the dilute annulus region, which indicates that the radial flow structure for dense circulating fluidized bed should be treated as a core-annulus-wall three-region structure, instead of the well-known core-wall two-region structure. In Part IV, the formation mechanisms of the core-annulus-wall structure in a CFB riser are discussed. An analytic model is developed for quantifying the flow structure in the developing regime, especially the solids concentration in the core. In addition, this study provides a rough evaluation of the effect of solids acceleration on the solid holdup measurement that is determined from pressure gradient measurements in a CFB riser.

CHAPTER 2

LITERATURE REVIEW

Previous studies of gas fluidization of nanoparticle agglomerates have found that the minimum fluidization velocity is about several orders of magnitude higher than the minimum fluidization velocity of primary nanoparticles (Chaouki *et al.,* 1985; Wang *et al.,* 2000; Wang *et al.,* 2002a; and Nam *et al.,* 2004). The size of the fluidized nanoparticle agglomerates is typically from about 100 to 700 μm, while the primary particle size ranges from 7 to 500 nm (Chaouki *et al.,* 1985; Wang *et al.,* 2002a; Jung and Gidaspow, 2002; and Nam *et al.,* 2004). For some nanoparticles, very smooth fluidization occurs with extremely high bed expansion, practically no bubbles are observed, and the velocity as a function of voidage around the fluidized agglomerates obeys the Richardson-Zaki equation (Chaouki *et al.,* 1985; Wang *et al.,* 2002a; and Nam *et al.,* 2004). This type of fluidization of nanoparticle agglomerates has been termed agglomerate particulate fluidization (APF) by Wang *et al.,* 2002a, and some fluidization characteristics have also been given although they are not complete and have not been studied systematically.

For other nanoparticles, fluidization results in a very limited bed expansion, and large bubbles rise up very quickly through the bed (Pacek and Nienow, 1990). This type of fluidization has been termed agglomerate bubbling fluidization (ABF) by Wang *et al.,* 2002a. Here again, experimental studies and the understanding of ABF nanoparticle fluidization are far from complete. However, even for homogeneously fluidized nanoparticles, relatively large powder elutriation occurs at the high gas velocities required to fluidize the nanoagglomerates. This loss of particles may hinder the applicability of fluidization of nanoparticle agglomerates in industrial processes.

A number of studies dealing with modeling and numerical simulation of the fluidization of nanoparticle agglomerates can be found in the literature. These models are based either on force (Chaouki *et al.,* 1985; Zhou and Li, 2002; and Nam *et al.,* 2004) or energy balances (Morooka *et al.,* 1988; Matsuda *et al.,* 2002) around individual agglomerates, the use of the Richardson-Zaki equation (Wang *et al.,* 2002a), or a combination of the Richardson-Zaki equation with fractal analysis (Nam *et al.,* 2004) for APF fluidization, or a modified kinetic theory (Jung and Gidaspow, 2002).

However, not much experimental data on the fluidization characteristics and differences between APF and ABF nanoparticles, such as minimum fluidization velocity, agglomerate size, hysteresis effects, and the effect of nanoparticle material properties are available, which calls for a systematic and experimental study of a wide spectrum of nanoparticle materials. The primary objective of this study therefore is to experimentally determine the fluidization characteristics of a variety of different nanoparticles (silica, alumina, titania, and carbon black nanoparticles), and to correlate the macroscopic fluidization behavior (APF or ABF) of the nanoagglomerates with the properties of the primary nanoparticles in a conventional gravity-driven fluidized bed without any additional external forces present.

Another task is to develop a simple and effective method to estimate the average size of the agglomerates and the bed voidage around the agglomerates which can then be used in models to determine the minimum fluidization velocity, pressure drop and other pertinent variables of the fluidization process. Furthermore, since nanoparticle agglomerates are hollow structures with typical porosities up to 98% or higher, it is necessary to determine the difference in the hydrodynamic force between the porous nanoparticle agglomerates in fluidization and solid particles of the same size and bulk density. To accomplish this, an analytical model of flow partitions through and around an agglomerate of nanoparticles in fluidization as well as the hydrodynamic force on the porous agglomerates is developed in this study and the results of the model will be discussed below.

CHAPTER 3

EXPERIMENTAL SETUP

A schematic diagram of the experimental fluidization system for conventional fluidization is shown in Figure 3.1. The system consists of a fluidized bed of nanoparticle agglomerates, flow and pressure measurement devices, a flow visualization system, and an optical sensor system for in-situ size measurement of agglomerates.

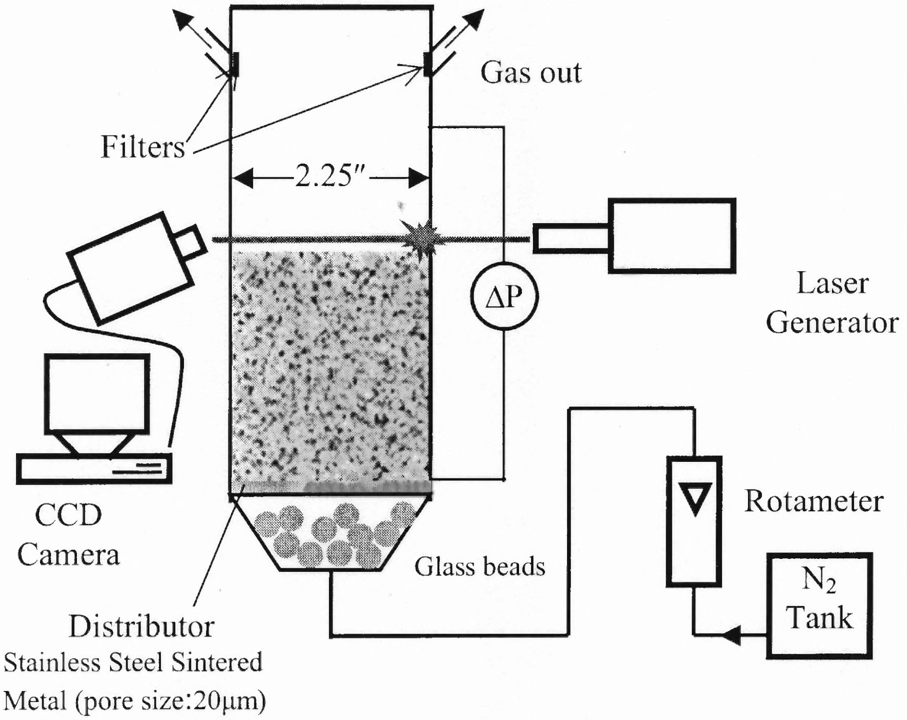

Figure 3.1 Systematic diagram of experimental system for conventional nanofluidization.

3.1 Fluidized Bed

The fluidized bed is a vertical transparent column with a distributor at the bottom consisting of a sintered stainless steel metal plate of 2 mm thick having a pore size of 20 μm. The column is a section of acrylic pipe with an inner diameter of 57 mm and a height of 910 mm. To generate a uniform gas field, glass beads of diameter between 2.5 and 3.5 mm are charged into a chamber placed below the distributor and above the gas inlet to form a packed bed about 100 mm high. An ultra-fine mesh filter is located at the gas outlet to filter out any elutriated nanoparticle agglomerates. Figure 3.2 is a photograph of the experimental system. To minimize any effect of humidity on the fluidization, pure dry nitrogen from a compressed nitrogen tank is used as the fluidizing gas.

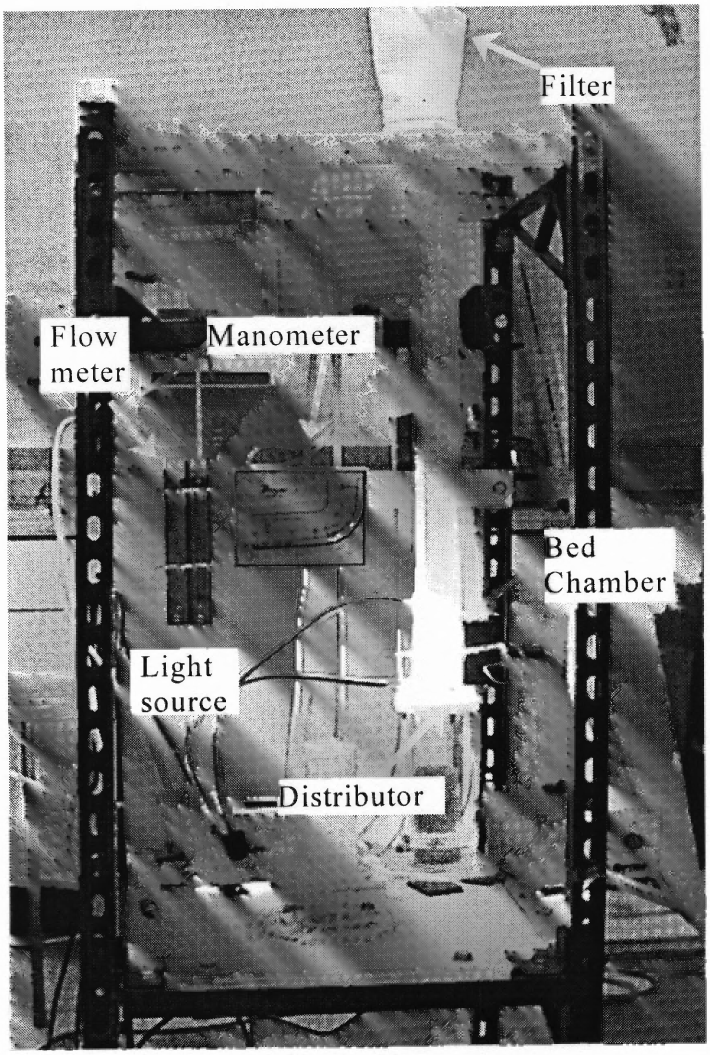

Figure 3.2 Experimental system for conventional nanofluidization.

3.2 Flow and Pressure Measurement Devices

The gas flow rate is measured and adjusted by two calibrated rotameters (Gilmont, Type23200-23210, and 014191-014200) placed in parallel with a combined flow range of up to 30 liters per minute. The bed pressure drop is measured between the two pressure taps, one located at the top of the column near the flow exit and the other located slightly above (3 mm) the distributor, so that it is not necessary to measure the pressure drop across the distributor. A digital manometer (Cole Parmer, 1.0 in. WC) is used to measure lower pressure drops (up to 25 mm H_2O) and an inclined tube manometer (Dewyer Mark-II) is used for higher pressure drops. The flow fluidization structure is visualized with the aid of a lighting device (Illumination Technologies, Model 150SX), recorded by a digital camcorder (Sony, Digital 8), and analyzed by a PC-based image processing software. Figure 3.3 is the photograph of the measurement devices of the pressure drop and flow rate. The left picture shows the digital pressure transducer and the right one shows the flow meters with the inclined manometer.

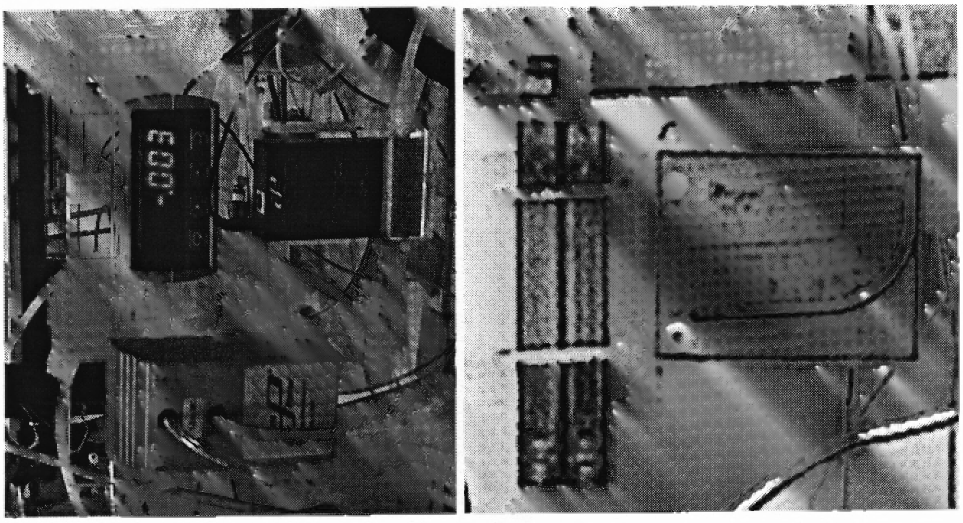

Figure 3.3 Digital pressure drop transducer and flow meters.

3.3 Optical Sensor System for In-situ Size Measurement

In-situ images of fluidized agglomerates are obtained with the aid of a laser source (Laser Physics Reliant 1000m) focused on the fluidized bed surface, a CCD camera (LaVision FlowMaster 3S), and an image processing system (Dual Xeon CPU). Figure 3.4 is a photograph of the in-situ size measurement system. Since the fluidized bed is relatively dense, the laser beam can not penetrate the bed effectively. Therefore it is difficult to measure the size of agglomerates throughout the bed; hence, the size of the agglomerates near the bed surface is measured instead.

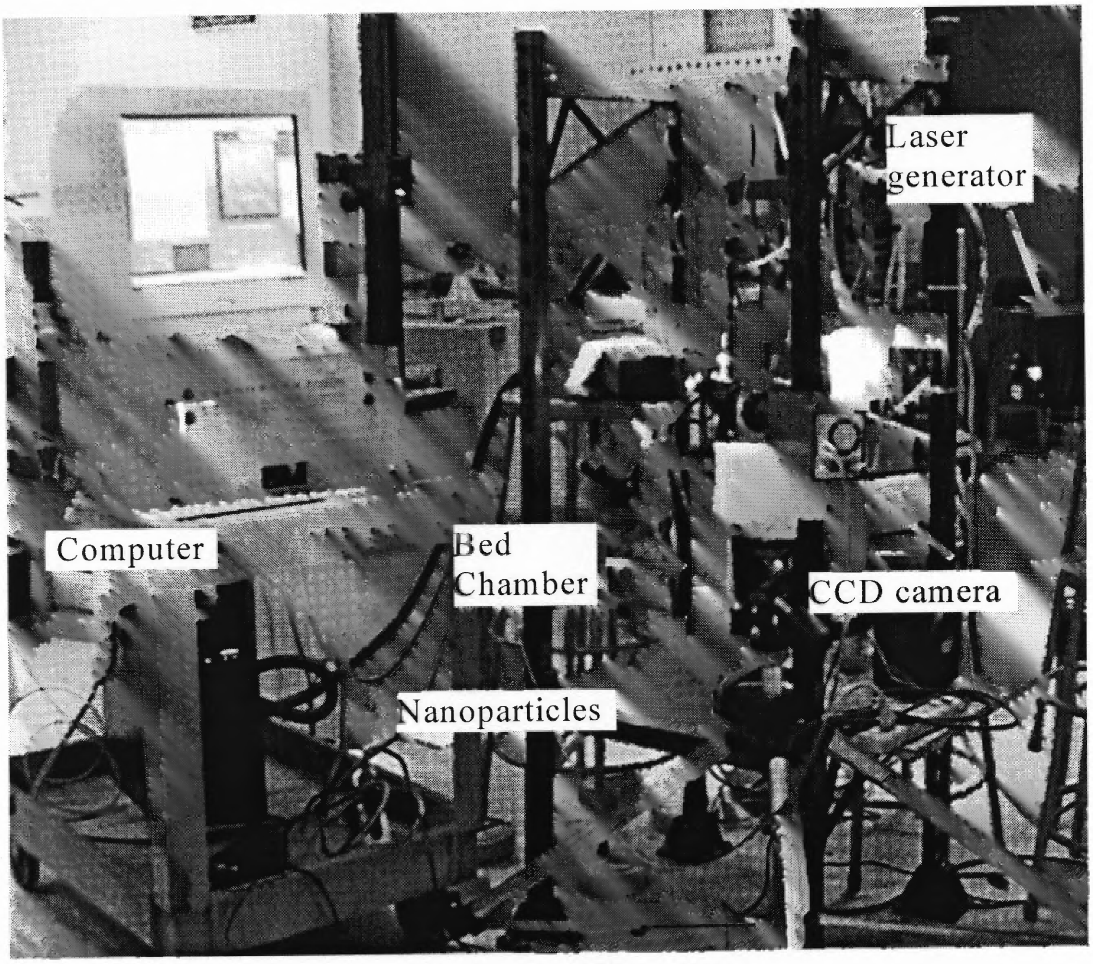

Figure 3.4 Photograph of the in-situ size measurement system.

3.4 Preparation of Nano-powder

In this study, eleven types of nanoparticle agglomerates are tested. Before the experiments, the particles were sieved using a shaker (Octagon 2000) and a 35-mesh sieve opening (about 500 μm). The sieving process serves to remove very large agglomerates, which may have been generated during packing, storage, and transportation. However, it should be noted that even after sieving, due to fragmentation and re-agglomeration during fluidization, some agglomerates in the bed might still exceed the sieve openings. The selection of a mesh opening of 500 μm is based on previous experimental findings that the typical size of fluidized nanoparticle agglomerates is between 100 to 400 μm. This typical size range of fluidized nanoparticle agglomerates is also validated in the current study, with the help of a laser source (Laser Physics Reliant 1000m), a CCD camera and an image processing system.

The bulk densities of the different sieved nanoparticles varied from 30 to 250 kg/m^3. Due to surface treatment by the manufacturer, the nanoparticles are either hydrophobic or hydrophilic. Fourteen different nanoparticles of various materials, primary particle size, and surface modification are investigated in this study; their properties are listed in Table 3.1.

Table 3.1 Properties of nanoparticles.

(DDS: Dimethyl-dichlorosilane; OCS: Octamethylcy-clotetrasiloxane; MCS: methacrylsilane)

Powder	Wettability	BET m^2/g	Size nm	Bulk Density kg/m^3	Mater -ial	Mater-ial Density kg/m^3	Surface Modifi -cation
R974	Hydrophobic	170	12	33.24	SiO_2	2560	DDS
R805	Hydrophobic	150	12	45.88	SiO_2	2560	DDS
R104	Hydrophobic	150	12	62.90	SiO_2	2560	OCS
R711	Hydrophobic	150	12	45.88	SiO_2	2560	MCS
COK 84	Hydrophilic	170	12	37.86	SiO_2-Al_2O_3 : 7-1	2740	None
R106	Hydrophobic	250	7	41.49	SiO_2	2560	OCS
A 300	Hydrophilic	300	7	39.00	SiO_2	2560	None
R972	Hydrophobic	110	16	39.00	SiO_2	2560	DDS
OX50	Hydrophilic	50	40	121.33	SiO_2	2560	None
A 90	Hydrophilic	90	20	52.00	SiO_2	2560	None
TiO_2	Hydrophilic	50	21	128.29	TiO_2	4500	None
Al_2O_3	Hydrophilic	150	13	29.10	Al_2O_3	3690	None
PEARLS 2000*	Hydrophobic	----	12	73.2	C	2250	None
REGAL 99R*	Hydrophobic	----	35-40	250.0	C	2250	None

Note:
* PEARLS 2000 and REGAL 99R carbon black are provided by Cabot Company, and all of the other particles are provided by Degussa Company, with trademark as Degussa Aerosil®.

CHAPTER 4

MODELING WORK

There are two objectives in this chapter: the first one is to investigate the hydrodynamic behavior of hollow nanoparticle agglomerates as compared to those of solid particles with the same size and density; the second objective is to estimate the size of the fluidizing nanoparticle agglomerates and the minimum fluidization velocity.

While the hydrodynamic analysis of solid particles in fluidization has been extensively performed (Happel, 1958; Davis and Birdsell, 1988; Fan and Zhu, 1998; and Rhodes *et al.,* 1998), hydrodynamic studies of agglomerates (i.e., effect of porosity) are very limited. Hence, in Section 4.1, a simple model is developed to show that drag force on a porous nanoparticle agglomerate in a swarm of nano-agglomerates (with a porosity up to 99% and bed voidage up to 0.8 in the fully fluidized bed) is close to that on a solid sphere in a similar swarm of solid spheres with a difference of less than 20%. Therefore, within an error margin of 20%, all of the existing modeling approaches based on classical solid particles in fluidization may be extended to nanoparticle agglomerates.

Agglomerate size is one of the key factors that influence the fluidization behavior of nanoparticles, and some models to predict the agglomerate size have been proposed for cohesive micron-size particles (Zhou and Li, 2002), and for nanoparticles (Chaouki *et al.,* 1985; Wang *et al.,* 2002a; and Nam *et al.* 2004). Chaouki *et al, 1985* proposed a mechanistic model to theoretically predict agglomerate size based on using the Richardson-Zaki equation without experimental validation, but it was assumed that the initial bed voidage is 0, which is not physically possible. Wang *et al.,* 2002a applied this model to predict the agglomerate size using their experimental data, but also assumed the initial bed voidage is 0, and this incorrect assumption lead to some unreasonable results. Nam *et al.,* 2004a proposed a model, which combined the Richardson-Zaki equation with fractal analysis, and successfully predicted the agglomerate size based on their own experimental data, but the mathematic derivation and calculation was relatively complicated. In this study, a simpler analytical model is developed to predict the size of the agglomerates, and is described in Section 4.2.

4.1 Drag Force Correction on Porous Nanoparticle Agglomerate in a Swarm in Creeping Flow

From SEM analysis, as shown in Figure 4.1, it appears that most nanoparticle agglomerates have highly porous structures, and exist in the form of multi-stage sub-agglomerates. The primary (normally, less than 20 nm) nanoparticles form chainlike clusters, and these three-dimensional netlike structures agglomerate into simple sub-agglomerates of a size range between 1 and 100 μm, but typically around 20 to 40 μm, and then these sub-agglomerates group together to generate large, 100 to 400 μm, porous floc-like agglomerates (Wang *et al.,* 2002a; Nam *et al.,* 2004). Even though it is well known that these large agglomerates are highly porous structures, with a typical porosity about 99% or higher, previous studies of nanoagglomerate fluidization have always assumed that the agglomerates are solid particles for the purposes of hydrodynamic analysis. Although some researchers (Wu and Lee, 1998; Wu and Lee, 2001) point out that treating porous floc-like nanoparticle agglomerates as solid particles may lead to oversimplification, no one has actually calculated the effect of the flow through the porous agglomerates of nanoparticles. Using a simple model, the drag force correction factor for the hydrodynamic force on highly porous floc-like agglomerate in a swarm of other similar agglomerates is estimated.

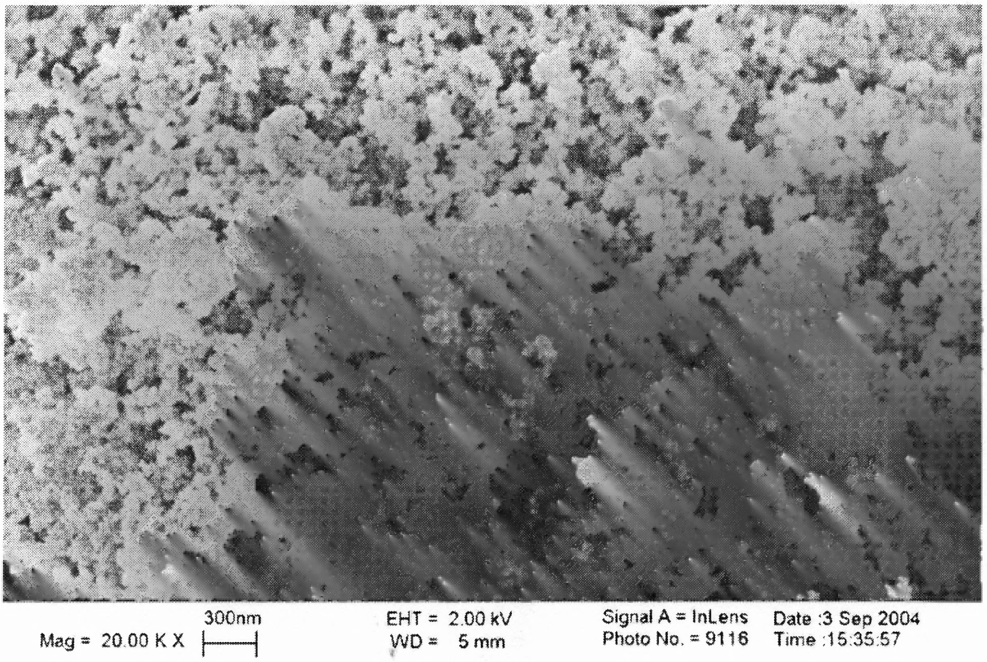

Figure 4.1 Porous structure of nanoparticle agglomerates. (Degussa Aerosil® A300, SiO_2, primary nanoparticle size 7 nm)

Based on Happel's free surface cell model (Happel, 1958), Neale *et al.*, 1973) proposed a model to evaluate the drag force F_{Dp} exerted on a permeable sphere in a swarm of permeable spheres in creeping flow (low Reynolds number):

$$F_{Dp} = 3\pi\mu d_a V \Omega_p \tag{4.1}$$

where V is the superficial fluid velocity flowing through the swarm, and Ω_p is the drag force correction factor due to the permeability of the sphere and the effect of neighboring spheres, and is given by:

$$\Omega_p = \frac{2\beta^2 + \frac{4}{3}\beta^2\eta^5 + 20\eta^5 - \frac{\tanh\beta}{\beta}(2\beta^2 + 8\beta^2\eta^5 + 20\eta^5)}{\left(\begin{array}{l} 2\beta^2 - 3\beta^2\eta + 3\beta^2\eta^5 - 2\beta^2\eta^6 + 90\beta^{-2}\eta^5 + 42\eta^5 - 30\eta^6 + 3 - \\ -\frac{\tanh\beta}{\beta}(-3\beta^2\eta + 15\beta^2\eta^5 - 12\beta^2\eta^6 + 90\beta^{-2}\eta^5 + 72\eta^5 - 30\eta^6 + 3) \end{array}\right)} \tag{4.2}$$

Here, β is a permeability dependent dimensionless sphere radius:

$$\beta = \frac{d_a}{2\sqrt{k}} \tag{4.3}$$

d_a is the sphere diameter, k is the permeability of single permeable sphere, and η is a bed voidage dependent dimensionless parameter defined as:

$$\eta = (1-\varepsilon_g)^{1/3} \tag{4.4}$$

where ε_g is the bed voidage around the whole swarm.

For very large β (very low k) the hydrodynamic behavior of a permeable sphere in a swarm of permeable spheres is similar to that of a solid sphere in a swarm of solid spheres; therefore, as $\beta \to \infty$, Equation (4.2) will reduce to Happel's formula for a solid sphere in a swarm of solid spheres:

$$\Omega_s = \frac{2 + \frac{4}{3}\eta^5}{2 - 3\eta + 3\eta^5 - 2\eta^6} \tag{4.5}$$

where Ω_s is the drag force correction factor for a solid sphere in a swarm of solid spheres due to the effect of neighboring spheres. Hence, the drag force F_{Ds} can be expressed as:

$$F_{Ds} = 3\pi\mu d_a V\Omega_s \tag{4.6}$$

If Ω is defined as the ratio of the drag force for a permeable sphere in a swarm of permeable spheres (F_{Dp}) to the drag force for a solid sphere in a swarm of solid spheres (F_{Ds}), then Ω can be obtained by combining Equation (4.1) and (4.6):

$$\Omega \equiv \frac{F_{Dp}}{F_{Ds}} = \frac{\Omega_p}{\Omega_s} \tag{4.7}$$

Hence, from Equations (4.2), (4.3), and (4.5), to get the value of Ω, the value of the permeability related dimensionless agglomerate radius β and the permeability of single permeable sphere k has to be obtained.

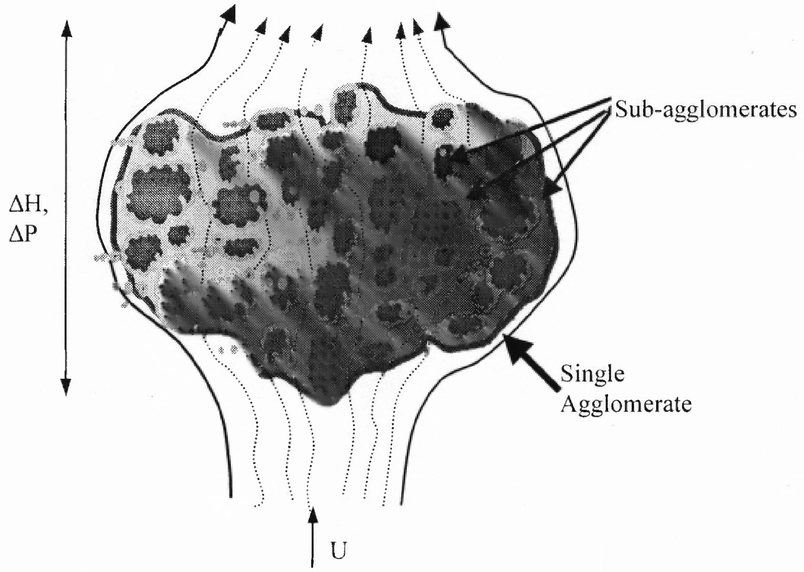

Figure 4.2 Schematic diagram of flow around and through a nanoparticle agglomerate.

Figure 4.2 is the schematic diagram of flow around and through a nanoparticle agglomerate. For a single agglomerate, most of fluid will pass around the agglomerate, but some of fluid may penetrate through the agglomerate because of the high porosity. This flow partition between flowing around and passing through the agglomerate will cause a drag force reduction compared with a solid particle. From Equations (4.2) and (4.5), if the permeability dependent dimensionless sphere radius β can be determined, then for any particle bed voidage, the drag correction factor can be obtained.

From Darcy's law, the pressure drop per unit length over porous agglomerate is related to the superficial fluid velocity as:

$$V = -\frac{k}{\mu}\frac{dP}{dz} \tag{4.8}$$

If it is assumed that the single agglomerate represents a packed bed, and we treat the sub-agglomerates as individual solid (impermeable to the gas) particles in this packed bed, then the Ergun equation (for low Reynolds number) can be applied to obtain a relation between the pressure drop per unit length, the voidage, and the sub-agglomerate size as:

$$\frac{dP}{dz} = 150\frac{(1-\varepsilon_{g,sub})^2}{\varepsilon_{g,sub}^3}\frac{\mu V}{d_{sub}^2} \tag{4.9}$$

Here, the volume fraction of gas (voidage) within the single large agglomerate but surrounding the sub-agglomerates (which are assumed to be solid) is defined as $\varepsilon_{g,sub}$ and the size of the sub-agglomerate as d_{sub}. It should be noted that $\varepsilon_{g,sub}$ is the gas phase volume fraction around the sub-agglomerates in a single porous nanoparticle agglomerate and is neither the gas phase volume fraction for the entire fluidized bed, which is expressed as ε_g, nor the gas phase volume fraction surrounding primary nanoparticles.

Combining Equations (4.8) and (4.9), we obtain a relation between the permeability, *k*, of single porous agglomerate, the sub-agglomerate porosity, $\varepsilon_{g,sub}$ and the sub-agglomerate size, d_{sub}:

$$k = \frac{\varepsilon_{g,sub}^3}{\left(1-\varepsilon_{g,sub}\right)^2}\frac{d_{sub}^2}{150} \tag{4.10}$$

The permeability related dimensionless agglomerate radius β can be calculated from Equation (4.3), as:

$$\beta = \frac{1}{2\sqrt{\dfrac{\varepsilon_{g,sub}^{3}}{150\left(1-\varepsilon_{g,sub}\right)^{2}}}} \cdot \frac{d_a}{d_{sub}} \tag{4.11}$$

Hence, if the size of agglomerate, the size of sub-agglomerate, and the porosity around a sub-agglomerate is known, then the drag correction factor can be obtained. The quantitative analysis is given in Chapter 5.

4.2 Analytical Model to Predict the Agglomerate Sizes for APF Nanoparticles (Modified Richadson-Zaki Equation)

It is well known that the Richardson-Zaki equation and the Ergun equation are applicable for solid (non-permeable) particles, but whether or not these equations are still valid for permeable nanoparticle agglomerates has not been addressed in the previous literature. It have been shown (see Section 4.1 and Chapter 5) that the error in assuming that the nanoparticle agglomerates behave as solid particles for the purposes of hydrodynamic analysis is very small for ABF nanoparticles (within 5%), and is also small for APF nanoparticles (within 20%) when they fluidize at very high bed expansions. This implies that the Richardson-Zaki and Ergun equations derived for solid particles should be applicable to these porous nanoparticle agglomerates.

By ignoring any elutriation and/or adhesion on the walls of the vessel, an overall mass balance on the powder in the fluidized bed is given by:

$$\rho_a\left(1-\varepsilon_g\right)HA = \rho_b H_0 A = \rho_{a0}\left(1-\varepsilon_{g0}\right)H_0 A \tag{4.12}$$

where ρ_a is the bulk density of the agglomerates and ε_g is the bed voidage around the agglomerates. It should be noted that ε_g excludes the voidage within the agglomerates themselves. In the model of Wang *et al.*, 2002a), they assume that $\rho_a \approx \rho_b$ so that

$$1\text{-}\varepsilon_g = H_0/H \tag{4.12a}$$

and the initial bed voidage (when H = H_0) ε_{g0}= 0 or α_{p0} = 1, which is physically unrealistic. When the nanoparticle agglomerates are loosely packed in the fluidizing vessel (chamber), the volume fraction of the particles can never reach 1 (ε_{g0} = 0), and the specific value will depend on the particle size distribution, sphericity of the particles, packing method, dimensions of the chamber, surface interaction with the chamber and other factors.

Normally, for "hard" solid particles, the typical bed voidage ε_{g0} in a loose packed bed is within the range of 0.35 to 0.5 (Fayed and Otten, 1997). However, for highly deformable particles (such as clay) and/or particles of different sizes, the voidage can be very much smaller (Fayed and Otten, 1997). Therefore, due to the highly porous and fragile structure of the nanoparticle agglomerates, and the relatively wide particle size distribution, it is possible that the initial packed bed voidage is much lower than the typical voidage of monodisperse hard solid particles.

An important assumption, which is made here, is that for a nanoparticle bed, the density of the agglomerates ρ_a remains almost constant before and during the fluidization so that:

$$\rho_a \approx \rho_{a0} \tag{4.13}$$

and Equation (4.12) can be written in the form:

$$\varepsilon_g = 1 - \frac{H_0}{H}\left(1-\varepsilon_{g0}\right) \tag{4.14}$$

Since it has been observed that APF nanoparticle agglomerates fluidize smoothly without any bubbles, and behave similar to particles fluidized by liquids, we also assume that the well-known Richardson-Zaki equation is valid. This equation relates the superficial gas velocity U_g with the bed voidage (around the agglomerates) and the terminal velocity for a single agglomerate U_{pt} as:

$$U_g = U_{pt}\,\varepsilon_g^n \tag{4.15}$$

Davis and Birdsell, 1988 have shown that a Richardson-Zaki exponent of n = 5.0 ± 0.1 should be used for the Stokes flow regime. Nam *et al.*, (2004) have also shown that a Richardson-Zaki exponent of n = 5 is valid for APF nanoparticle agglomerates.

Combining Equations (4.14) and (4.15), the relation between the superficial gas velocity and the particle terminal velocity can be written as:

$$U_{pt}^{\frac{1}{n}} - U_{pt}^{\frac{1}{n}}(1-\varepsilon_{g0})\frac{H_0}{H} = U_g^{\frac{1}{n}} \tag{4.16}$$

which reduces to a linear equation:

$$y = B - Ax \tag{4.17}$$

where

$$y = U_g^{\frac{1}{n}}\ ,\quad x = \frac{H_0}{H}\ ,\quad A = U_{pt}^{\frac{1}{n}}(1-\varepsilon_{g0})\ ,\quad B = U_{pt}^{\frac{1}{n}} \tag{4.18}$$

Hence, for each of the APF nanoparticle agglomerates, a plot of $U_g^{\frac{1}{n}}$ versus $\frac{H_0}{H}$ can be drawn, and from a linear regression, the slope $-A$ and the y-intercept B can be found. From these values the particle terminal velocity U_{pt} and the initial bed voidage ε_{g0} can be calculated as:

$$U_{pt} = B^n \tag{4.19}$$

$$\varepsilon_{g0} = 1 - \frac{A}{B} \tag{4.20}$$

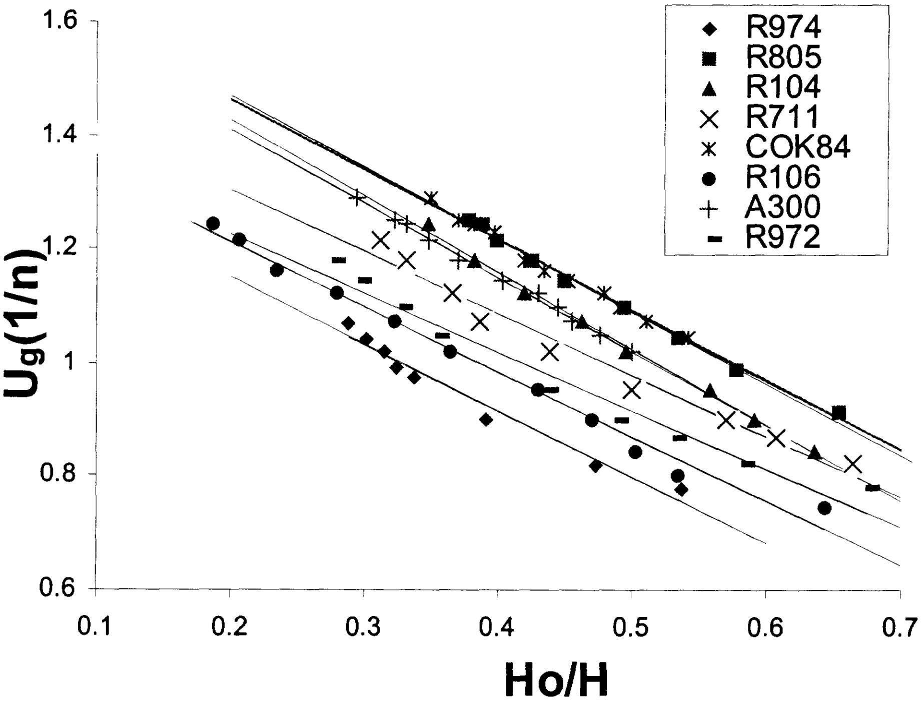

Figure 4.3 $U_g^{1/n}$ vs. H_0/H for APF nanoparticles. Solid lines are linear regression results, and data points are experimental results, for a Richardson-Zaki exponent n = 5.

Figure 4.2 is a typical plot of $U_{pt}^{1/n}$ vs. H_0/H for the eight different APF nanoparticles (primary size 7- 16 nm, bulk density 33.24 – 62.90 kg/m^3), with n=5; all of the data points fall within the zone between the inner and outer solid lines. The figure also shows that all of the straight lines (for each of the eight nanoparticle agglomerates) intersect the y-axis fairly close to each other, indicating that the terminal velocities for these eight nanoparticles are roughly of the same order of magnitude. The curves for each of the nanoparticles also have similar slopes, and since the terminal velocities are close to each other, the initial bed voidages are also close to one another.

From the values of U_{pt}, obtained from the y-intercepts in Figure 4.3 and assuming Stokes law, the average size of the agglomerates can be calculated from:

$$d_a = \sqrt{\frac{18\mu U_{pt}}{(\rho_a - \rho)g}} \tag{4.21}$$

The above derivation is the methodology of estimating agglomerate size, and once the agglomerate size is known, then for APF nanoparticles at low Reynolds numbers, the minimum fluidization velocity U_{mf} can be calculated from the simplified Ergun equation:

$$U_{mf} = \frac{\Delta P}{H} \frac{{d_a}^2}{150\mu} \frac{\varepsilon_{gmf}^3}{(1-\varepsilon_{gmf})^2} \tag{4.22}$$

CHAPTER 5

RESULTS AND DISCUSSION

The experimental results, as well as some modeling results of conventional fluidization of nanoparticle agglomerates will be discussed in this chapter, and the corresponding conclusion remark will also be included in this chapter.

5.1 Fluidization Behavior

As listed in table 3.1, in this study, fourteen types of nanoparticles (Silica, Alumina, Titania, and carbon black nanoparticles) are tested. Among these fourteen nanoparticles, only Cabot Carbon Black ® REGAL 99R could not be fluidized, and since this study aims to study the fluidization behavior of nanoparticles, so, in this chapter, only the nanoparticles could be fluidized will be discussed.

As already discussed in the above chapters, nanoparticles can only be fluidized in the form of large porous agglomerates due to the very strong interaction forces between them. Typical fluidization curves, i.e., bed expansion and pressure drop curves, for APF and ABF nanoparticles are shown in Figures 5.1 and 5.2, respectively. For both APF and ABF nanoparticle agglomerates, the pressure drop increases with increasing superficial gas velocity and then reaches a plateau and becomes independent of the gas velocity. The value of the pressure drop plateau is usually close to the weight of the bed per unit area, indicating that the total weight of the particles is balanced by the pressure drop, all of the solid particles are suspended, and the bed is fully fluidized. The critical velocity beyond which a pressure drop plateau is reached is defined as the minimum fluidization velocity.

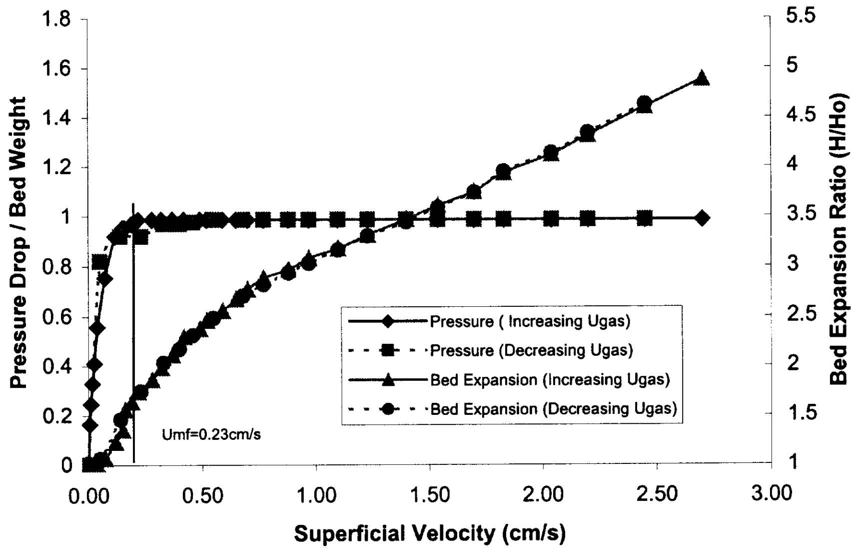

a. Degussa Aerosil® R974.

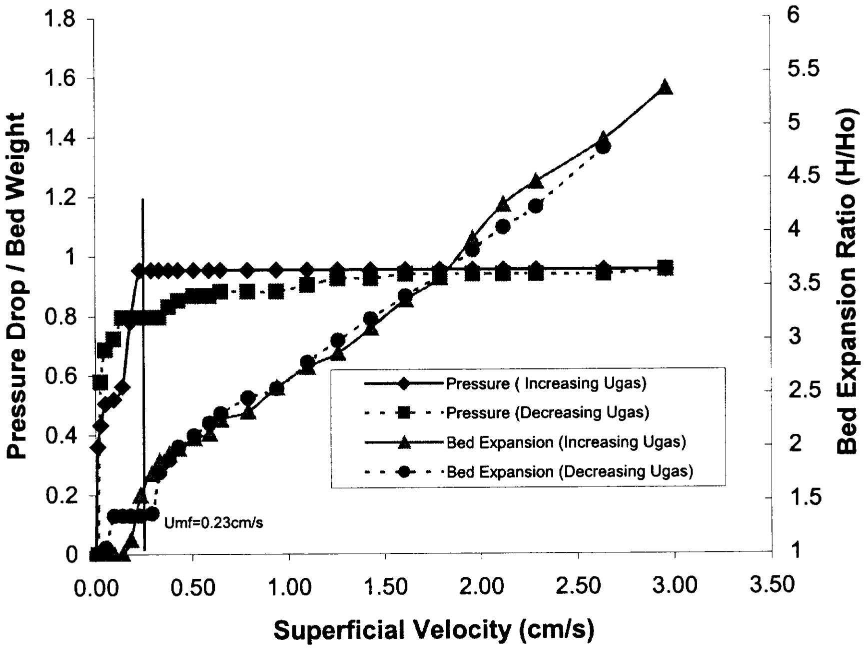

b. Degussa Aerosil® R106.

Figure 5.1 Typical fluidization curves for APF nanoparticles.

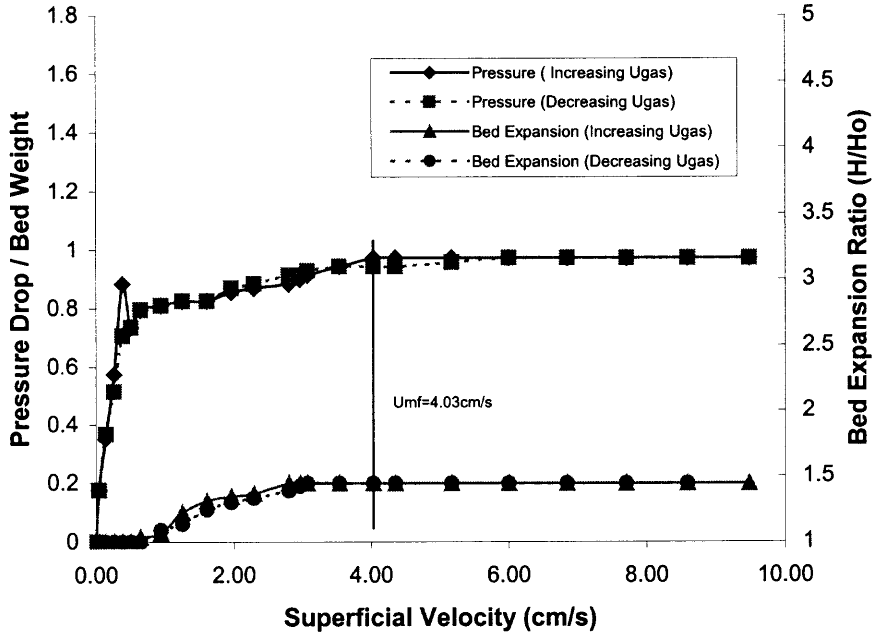

a. Degussa Aerosil ® OX50.

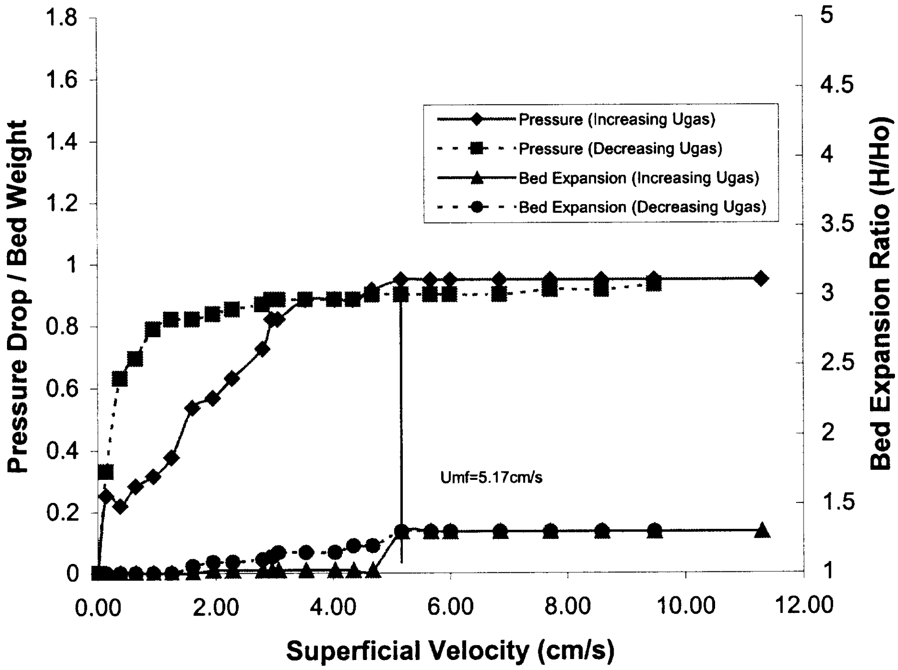

b. Degussa Titanium Dioxide P25.

Figure 5.2 Typical fluidization curves for ABF nanoparticles.

For APF nanoparticles, it is observed that the bed fluidizes and expands very uniformly without bubbles with a large expansion ratio of up to 500% or more, the bed expansion increases with increasing gas velocity, and the agglomerates distribute uniformly within the bed. Figure 5.1 shows that the bed starts to expand at a gas velocity much smaller than the minimum fluidization velocity; hence the bed exhibits a fluid-like behavior at velocities much lower than the minimum fluidization velocity. As shown in Figure 5.2, for ABF nanoparticles, the bed expands very little with increasing gas velocity (less than 50%), and large bubbles rise up very quickly through the bed, and the agglomerates distribute non-uniformly within the bed, the smaller agglomerates appear to be smoothly fluidized in the upper part of the bed, while the larger agglomerates could be found moving slowly at the bottom.

Table 5.1 Properties of nanoparticles.
(DDS: Dimethyl-dichlorosilane; OCS: Octamethylcy-clotetrasiloxane; MCS: methacrylsilane)

Powder	Wettability	BET m^2/g	Size nm	Bulk Density kg/m^3	Material	Material Density kg/m^3	Fluidization Type	Surface modification	Measured Umf (cm/s)
R974	Hydrophobic	170	12	33.24	SiO_2	2560	APF	DDS	0.23
R805	Hydrophobic	150	12	45.88	SiO_2	2560	APF	DDS	0.65
R104	Hydrophobic	150	12	62.90	SiO_2	2560	APF	OCS	0.43
R711	Hydrophobic	150	12	45.88	SiO_2	2560	APF	MCS	0.38
COK 84	Hydrophilic	170	12	37.86	SiO_2-Al_2O_3 : 7-1	2740	APF	None	1.26
R106	Hydrophobic	250	7	41.49	SiO_2	2560	APF	OCS	0.23
A 300	Hydrophilic	300	7	39.00	SiO_2	2560	APF	None	1.10
R972	Hydrophobic	110	16	39.00	SiO_2	2560	APF	DDS	0.29
Al_2O_3	Hydrophilic	150	13	29.10	Al_2O_3	3690	APF	None	3.54
C *	Hydrophilic	-	12	73.0	C	2250	APF	-	3.86
OX50	Hydrophilic	50	40	121.33	SiO_2	2560	ABF	None	4.03
A 90	Hydrophilic	90	20	52.00	SiO_2	2560	ABF	None	7.71
TiO_2	Hydrophilic	50	21	128.29	TiO_2	4500	ABF	None	5.17

* Cabot Carbon Black ® PEARLS 2000.

It appears that the difference in fluidization behavior between APF and ABF depends largely on the bulk density and the primary particle size. The fluidization of relatively small (less than 20 nm) nanoparticles with a bulk density less than 100 kg/m^3 (see Table 5.1) appear to behave as APF, whereas larger and heavier nanoparticles are likely to behave as ABF.

5.2 Hysteresis Phenomena and Definition of Minimum Fluidization Velocity

A hysteresis in fluidization is referred to the phenomenon where the bed pressure drop or bed height depends on the mode of changing fluidizing velocity, namely, whether the velocity is increased from a packed state to a fluidized state or vice versa (Heck and Onken, 1987; Petrovic *et al.,* 1989; Peng and Fan, 1995). A theoretical model for the hysteresis phenomenon is given by Loezos *et al.* (2002), based on the role of contact stresses and wall friction in fluidization. Some hysteresis effects have been observed in the pressure drop and bed height measurements for all of the eleven different nanoparticle agglomerates used in this study, but different nanoparticle agglomerates show large differences in the hysteresis curves obtained (see Figures 5.1 and 5.2). For example, for some nanoparticles, such as Degussa Aerosil® R974, the pressure drop curves for both the fluidization branch and the defluidization branch are quite close, and the hysteresis phenomenon is negligible, but for other nanoparticles, such as Degussa Aerosil® Titanium Dioxide P25, the deviation of the pressure drop curves for the fluidization and defluidization branch is fairly large. Generally, nanoparticle agglomerates (ABF behavior), which are more difficult to fluidize, show a stronger hysteresis.

When the superficial gas velocity is decreased after the bed has been fluidized, the pressure drop will first remain constant, and then decline upon a further decrease in gas velocity indicating defluidization has occurred. It is observed, however, that for some nanoparticles the pressure drop begins to decline upon decreasing the gas velocity even though the bed still appears to be fully fluidized (see Figure 5.1b) or remains at the plateau level at velocities much lower than those needed to attain fluidization (see Figure 5.2b). Hence, in this study, the fluidization branch of the pressure drop cycle has been chosen as the reference to define the minimum fluidization velocity as the superficial gas velocity beyond which the bed pressure drop is no longer dependent upon velocity and becomes constant.

5.3 Estimation of Drag Correction Factor for Nanoparticle Agglomerates

The voidage $\varepsilon_{g,sub}$ is very difficult to determine, so it is assumed to be 0.5, a typical value for a loosely packed bed of solid particles (Fayed and Otten, 1997; Fan and Zhu, 1998). d_{sub} is chosen to be 30 μm (the average sub-agglomerate size), based on SEM measurements by Nam *et al.* (2004). The size of the large agglomerates, d_a, is obtained from the calculated results in Table 5.4 and β is calculated using Equation 4.3. Hence once β is obtained, then the drag force correction factor can be calculated from Equation 4.2.

Table 5.2 presents the calculated results of the permeability related dimensionless radius β for eleven of the nanoparticles studied; all of the values of β are in the range of 50 to 260. Table 5.3 presents the calculated results of the drag force correction factor, Ω, for permeable agglomerates in a swarm. β is selected as 58.8 and

258 (the lower and upper limit for the eleven nanoparticles), and ε_g was varied between 0.5 and 1.0. The results show that for the lower limit of β=58.8 (R106, APF nanoparticles), the correction factors Ω for the drag force vary between 0.79, and 0.98 and increase with increasing bed voidage ε_g; for the upper limit of β =258 (A90, ABF nanoparticles), the correction factors Ω are all higher than 0.95.

Hence, for ABF nanoparticles, and also for APF nanoparticles, which fluidize at very high bed expansions (high ε_g), it appears that the error in assuming the highly porous nanoparticle agglomerates behave as solid particles for the purposes of hydrodynamic analysis is small. This implies that the Richardson-Zaki and Ergun equations derived for solid particles should be applicable to these porous nanoparticle agglomerates.

Table 5.2 Permeability related dimensionless radius β for nanoparticle agglomerates.

Powder	Primary Size (nm)	Agglomerate Size (μm)	Permeability Related Dimensionless Radius β
R974	12	211	60.9
R805	12	279	79.9
R104	12	245	67.9
R711	12	207	60.4
COK84	12	316	92.1
R106	7	201	58.8
A 300	7	296	86.5
R972	16	195	67.0
OX50	40	300(estimated)	86.6
A 90	20	896(measured)	258.
TiO_2	21	195(measured)	56.2

Table 5.3 Drag force correction factors for nanoparticle agglomerates.

ε_g	$\beta = 58.8$ (R106, APF)			$\beta = 258$ (A90, ABF)		
	Ω_p	Ω_s	$\Omega = \frac{\Omega_p}{\Omega_s}$	Ω_p	Ω_s	$\Omega = \frac{\Omega_p}{\Omega_s}$
0.5	30.3	37.9	0.79	36.1	37.9	0.95
0.6	16.1	18.9	0.85	18.3	18.9	0.97
0.7	9.06	10.1	0.89	9.89	10.1	0.98
0.8	5.22	5.60	0.92	5.54	5.60	0.98
0.9	2.96	3.11	0.97	3.08	3.11	0.99
1.0	0.98	1.00	0.98	1.00	1.00	1.00

5.4 Size of Nanoparticles Measurement

Agglomerate size is one of the key factors that influence the fluidization behaviors of nanoparticles. We have obtained *in situ* measurements of agglomerate size in a fluidized bed of nanoparticles, using an optical system to image the agglomerates on the surface of the fluidized bed (Zhu *et al.,* 2004). Figure 5.3 shows typical images of the APF and ABF agglomerates on the fluidized bed surface. The images show that although the agglomerates are not spherical, due to the random orientation of the irregular agglomerates in the gas flow, it is assumed that the agglomerates can be represented as spheres. Figure 5.4 shows the size distribution of one type of nanoparticles studied; Table 5.4 summarizes the results for all of the other nanoparticles.

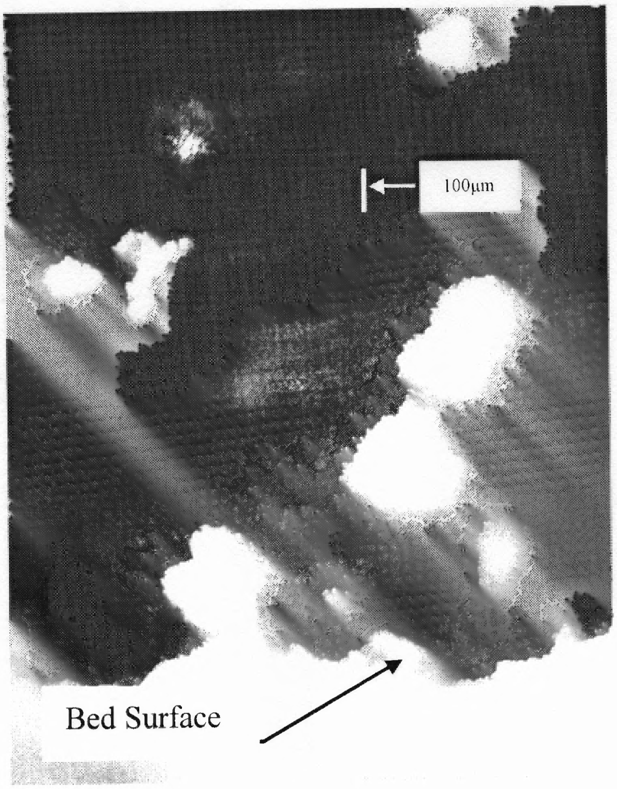

Figure 5.3a. Images of APF nanoagglomerates near the fluidized bed surface (Degussa Aerosil ® R974).

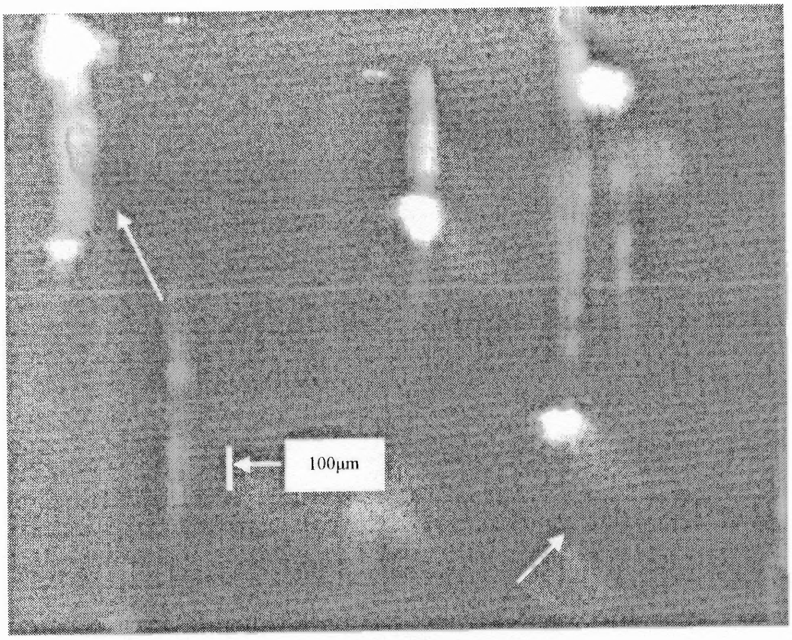

Figure 5.3b. Images of ABF nanoagglomerates near the fluidized bed surface (Degussa Titanium Dioxide P25).

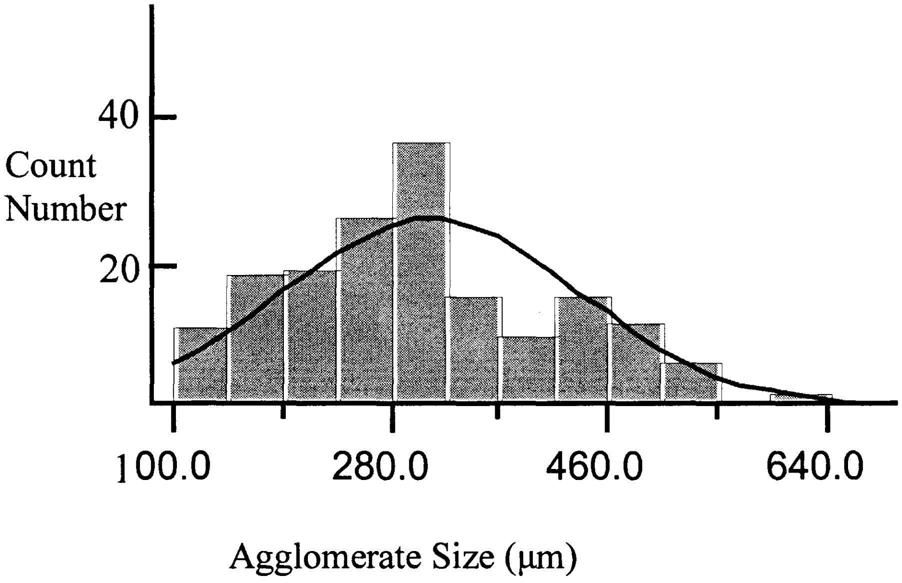

Figure 5.4 Typical agglomerate size distribution (Degussa Aerosil® R974).

Table 5.4 Statistics of measured agglomerate sizes.

Powder	Sampling Number	Experimental Agglomerate Mean Size (µm)	Standard Error Mean (µm)	Upper 95% Mean (µm)	Lower 95% Mean (µm)
R974	193	315	8.8	333	298
R805	108	218	7.9	234	202
R104	427	226	3.7	233	219
R711	250	274	10.8	296	253
COK84	59	320	20.9	362	278
R106	179	172	5.7	183	160
A 300	230	585	15.7	616	554
R972	139	422	15.2	452	392
A 90	189	896	33.2	961	830
TiO_2	144	195	5.4	205	184

5.5 Agglomerate Size Prediction for APF Nanoparticle Agglomerates

Most of the predicted results in Table 5.5 compare reasonably well with the measurements, although some differ by as much as a factor of 2. Given the limitations of the measurement technique and uncertainties in the model assumptions, this discrepancy is considered satisfactory. Both the calculated and experimental mean sizes of the fluidized nanoparticle agglomerates are from 200 to 600 μm, which are about four orders of magnitude larger than the primary particle sizes.

Table 5.5 Calculated agglomerate sizes and initial bed voidage for APF nanoparticles (n=5).

Powder	U_{pt} (cm/s) Calculated	ε_{g0} Calculated	d_a (μm) Calculated	d_a (μm) Measured
R974	5.09	0.152	211	315
R805	14.6	0.277	279	218
R104	14.1	0.206	245	226
R711	8.16	0.285	207	274
COK84	15.1	0.266	316	320
R106	6.21	0.206	201	172
A 300	12.9	0.223	296	585
R972	6.04	0.278	195	422
Mean		0.237 (Std. Dev. = 0.046)		

To investigate the sensitivity of the Richardson-Zaki exponent on the calculated mean agglomerate size, two different values of n = 4 and n = 6 are selected and the linear regression analysis is repeated. Table 5.6 shows the calculated results for the mean agglomerate diameters for n = 4, 5, and 6. Surprisingly, the diameter of the agglomerates was found to be relatively insensitive to the value of the Richardson-Zaki exponent. For example, for R974 nanoparticles, the mean agglomerate size is 217 μm for n = 4, 211 μm for n = 5, and 204 μm for n = 6, respectively. Nam *et al.*, 2004 also studied the sensitivity of the value of n, and drew a similar conclusion. Table 5.6 shows a comparison of the results for the mean agglomerate size based on our model with those obtained from the fractal analysis model proposed by Nam *et al.* (2004) for all three values of n = 4, 5 and 6; the difference is within 2% which lends confidence to using our simpler model for predicting the agglomerate size of APF nanoparticles. It should be noted, however, that the model cannot be used to predict the mean agglomerate size of ABF nanoparticles.

Table 5.6 Comparison of models used to predict the agglomerate size of R974 nanoparticles.

R974	Agglomerate diameter (μm) Based on present model	Agglomerate diameter (μm) Based on fractal analysis model Nam *et al.* (2004)	Agglomerate diameter (μm) Experimental measurement
n = 4	218	214	315
n = 5	211	208	315
n = 6	204	202	315

5.6 Minimum Fluidization Velocity for APF and ABF Nanoparticles

For APF nanoparticles at low Reynolds numbers, the minimum fluidization velocity U_{mf} can be calculated from the simplified Ergun equation (4.22), and here the measured pressure drop and bed height at minimum fluidization (obtained from plots similar to Figure 5.1 for each of the APF nanoparticles), and values of ε_{gmf} taken from Figure 5.1 at the minimum fluidization velocity, U_{mf} are used. The calculated minimum fluidization velocities are compared with the experimental measurements in Table 5.7, which show a fairly good agreement between the two. Table 5.7 also lists the Reynolds numbers for each of the APF nanoparticles (ranging from 0.05 to 0.35 and thus in the creeping motion regime), and the bed expansion ratios at the minimum fluidization velocity.

Table 5.7 Fluidization characteristics of APF nanoparticles.

Powder	Measured U_{mf} (cm/s)	Calculated U_{mf} (cm/s)	Measured $\frac{H_{mf}}{H_0}$	Re_{mf} $(\frac{\rho_a d_a V}{\mu})$	Fr_{mf} $(\frac{u_{mf}^2}{d_a g})$	$\frac{\rho_a - \rho_g}{\rho_g}$	$\frac{H_{mf}}{d_t}$	Π
R974	0.23	0.17	1.73	0.05	0.0013	31.7	3.71	0.008
R805	0.65	0.56	1.53	0.19	0.0109	51.9	2.27	0.246
R104	0.43	0.42	1.57	0.13	0.0068	65.0	3.41	0.197
R711	0.38	0.31	1.51	0.08	0.0045	52.5	2.24	0.043
COK84	1.26	0.94	1.84	0.35	0.0316	42.0	3.32	1.55
R106	0.23	0.17	1.55	0.05	0.0015	42.6	2.55	0.008
A 300	1.1	0.83	2.00	0.29	0.0288	40.8	3.5	1.19
R972	0.29	0.24	1.48	0.05	0.0021	44.1	2.2	0.010

Table 5.8 gives the measured mean agglomerate size, minimum fluidization velocity, and the bed expansion ratio and Reynolds number at minimum fluidization for the three ABF nanoparticles. In addition to exhibiting much lower bed expansions and much higher minimum fluidization velocities, these nanoagglomerates also have much higher Reynolds numbers (1.7 to 16) at minimum fluidization.

Table 5.8 Fluidization characteristics of ABF nanoparticles.

Powder	Measured Agglomerate size (μm)	Measured U_{mf} (cm/s)	Measured $\frac{H_{mf}}{H_0}$	Re_{mf} $(\frac{\rho_a d_a V}{\mu})$	Fr_{mf} $(\frac{u_{mf}^2}{d_a g})$	$\frac{\rho_a - \rho_g}{\rho_g}$	$\frac{H_{mf}}{d_t}$	Π
OX50	300*	4.03	1.44	1.81	0.552	131.	3.02	398
A 90	896	7.71	1.11	16.5	0.677	55.8	2.31	1441
TiO_2	195	5.17	1.3	1.74	1.4	139.	2.73	927

* Estimated, could not be measured.

It is also noted from Table 5.1, the average U_{mf} of the six hydrophobic (due to surface modification) APF nanoparticles (Degussa Aerosil® R974, R805, R104, R711, R106, R972) is 0.37 cm/s whereas the average U_{mf} for the two hydrophilic (without surface modification) nanoparticles (Degussa Aerosil® COK84, A300) is much higher at 1.18 cm/s. This difference is probably due to the better flowability of the hydrophobic nanoparticles after surface modification. There may also be some moisture trapped within the hydrophilic particles making them more cohesive than the hydrophobic particles.

5.7 Classification Criterion to Differentiate APF and ABF Nanoparticles

Earlier it has been stated that the difference in fluidization behavior between smooth, liquid like, bubbleless, particulate fluidization with high bed expansion (APF), and non-homogeneous, bubbling, aggregative fluidization with low bed expansion (ABF) depends largely on the bulk density and the primary particle size. Based on the experimental results, it is concluded that the fluidization of relatively small (less than 20 nm) nanoparticles with a bulk density less than 100 kg/m^3 (see Table 5.1) appear to behave as APF, whereas larger and heavier nanoparticles are likely to behave as ABF. Of course, this hypothesis is based only on experimental data using thirteen different nanoparticles, and more research is needed to confirm that this classification criterion is indeed applicable for all nanoparticles.

On the basis of experimental data using classical fluidized particles such as FCC catalyst, UOP catalyst, and hollow resin, Romero and Johanson (1958) present a criterion to characterize the quality of fluidization as either smooth or bubbling, depending on the value of a combination of dimensionless groups. These dimensionless groups consist of the product (Π) of the particle to fluid density ratio, the Reynolds and Froude number at minimum fluidization, and the bed height to bed diameter ratio:

$$\begin{aligned} \Pi &= Fr_{mf}\,\mathrm{Re}_{mf}\,\frac{\rho_a-\rho_g}{\rho_g}\,\frac{H_{mf}}{d_t}<100, && \textit{smooth fluidization} \\ \Pi &= Fr_{mf}\,\mathrm{Re}_{mf}\,\frac{\rho_a-\rho_g}{\rho_g}\,\frac{H_{mf}}{d_t}>100, && \textit{bubbling fluidization} \end{aligned} \qquad (5.1)$$

Although the porous nanoparticle agglomerates behave differently than the classical solid particles used to obtain equation (5.1), there are some definite similarities, and the values of the combination of dimensionless groups (which is designated as Π) for all eleven nanoparticles used in the experiments are calculated. The calculated results (see Tables 5.7 and 5.8) agree remarkably well with this criterion. For the eight APF nanoparticles, the values of Π are within the range of 0.008 ~ 1.55, which is much less than 100, whereas, for the three ABF nanoparticles, the values of Π are within the range of 398 ~ 1441, which is much larger than 100. Hence, this criterion may also be valid for nanoparticle agglomerates, and therefore could be used to check whether a nanoparticle of interest will behave as APF or ABF. Of course, this hypothesis is based only on experimental data using eleven different nanoparticles, and more research is needed to confirm that this classification criterion is indeed applicable for all nanoparticles.

5.8 Concluding Remarks

Highly porous nanoparticle agglomerates exhibit two distinct fluidization behaviors, APF (smooth fluidization without bubbles at minimum fluidization) and ABF (bubbles at minimum fluidization). APF agglomerates show very large bed expansions, up to five times the initial bed height as the superficial gas velocity is raised, and the Reynolds numbers for these nanoagglomerates at minimum fluidization are very low (0.05 to 0.35), which indicate that the agglomerates are in creeping flow. ABF nanoagglomerates fluidize with large bubbles and show very little bed expansion as the superficial gas velocity is raised and the Reynolds numbers at minimum fluidization are close to or higher than 2.0, which indicate that hydrodynamic inertial effects cannot be neglected.

A model for a permeable sphere in a swarm of permeable spheres shows that fluidized APF nanoparticle agglomerates (at large ε_g) can be treated as solid particles for hydrodynamic analysis with little error, so that the Ergun and Richardson-Zaki equations derived for solid particles should also be applicable to porous nanoparticle agglomerates. For APF nanoparticles, a model based on the initial bed voidage around the agglomerates and the Richardson-Zaki equation was used to predict the mean agglomerate size in the fluidized bed. The analysis is relatively insensitive to the value of the Richardson-Zaki exponent and in this study $n = 5$ is used, since the flow is in the creeping motion regime. It is found that the initial bed voidage for the nanoparticle agglomerates is around 0.2 to 0.25, which is lower than the theoretical packing voidage of spheres of uniform size, but is reasonable for soft agglomerates of wide size distribution. Agglomerate sizes on the fluidized bed surface are measured using an in-situ optical measurement method and compared fairly well with the model predictions. Typical sizes of the nanoparticle agglomerates are within the range of 200 to 600μm.

The Ergun equation, based on the agglomerate size and voidage at minimum fluidization predicted by the model, can be used to calculate the minimum fluidization velocity for APF nanoparticle agglomerates. The calculated results agree very well with the experimental results. It was also found that the hydrophobic nanoparticles with surface modification result in a lower minimum fluidization velocity as compared to hydrophilic particles because of improved flowability (less moisture uptake).

A classification criterion based on the value of a combination of dimensionless groups to differentiate between particulate and bubbling fluidization for classical solid fluidized particles appears to also predict remarkably well whether nanoparticles will behave as APF or ABF. This criterion may be superior to simply using the size and bulk density of the nanoparticles to predict their fluidization behavior.

5.9 Limitation of this Study and Future Research Directions

There are lots of unknowns in the study of conventional fluidization of nanoparticle agglomerates, and extensive experimental investigations and more modeling efforts are needed. One very important unknown is the mechanism of agglomeration and de-agglomeration of nanoparticles, which will determine the size of stable fluidizing agglomerates, and therefore provide the information to determine the required external forces to break up the agglomerates. In order to investigate the mechanism of agglomeration and de-agglomeration, we need to perform nanoscale mechanical experiments to investigate the forces among nanoparticles or sub-agglomerates.

Additional experiments to test other types of nanoparticle agglomerates are also recommended, which may provide more information on the fluidization behavior and how to predict it from the properties of the individual Nan particles. Finally, the general theory of conventional fluidization of nanoparticle agglomerates, especially models of the inter-agglomerate and inter-sub-agglomerate hydrodynamic forces, and the hydrodynamic force among primary nanoparticles, needs to be developed. This may also help to investigate the effect of external excitations.

CHAPTER 6

LITERATURE REVIEW

Previous literature with regard to sound assisted fluidization will be summarized in section 6.1, and magnetic assisted fluidization related literature will be summarized in section 6.2.

6.1 Sound Assisted Fluidization

Cohesive micron or even sub-micron sized fine particles, typically known as Group C particles, according to the Geldart classification, have been successfully fluidized by the assistance of acoustic fields (Chirone *et al.,* 1992;Chirone and Russo, 1995; Levy *et al.,* 1997; Herrera and Levy, 2002). At a low sound frequency, typically from 50 to 400 Hz, and a high sound pressure level, typically above 110 dB, sound waves can improve the fluidization of fine particles, which otherwise showed intense channeling or slugging rather than fluidization (Morse, 1955). Standing waves are generated in the experimental column. At a fixed sound pressure level, sound assisted fluidization can only occur within a certain range of low sound frequencies. Channeling is found above and below this frequency range (Russo *et al.*, 1995). At the natural frequency of a bed of micron sized particles, high intensity sound waves lead to reductions in both the minimum bubbling velocity and the minimum fluidization velocities (Levy *et al.*, 1997). An increase in sound pressure level may also yield a decrease in bed expansion, an increase in bubble frequency and an increase in bubble size (Levy *et al.*, 1997; Herrera and Levy, 2001). In addition, high intensity sound can also effectively reduce the elutriation of fine particles (Chirone *et al.*, 1992).

So far all studies on sound-assisted fluidization have been focused on the fluidization of micron or sub-micron sized particles (Chirone *et al.,* 1992;Chirone and Russo, 1995; Levy *et al.,* 1997; Herrera and Levy, 2002). No results have been reported on the effects of sound on the fluidization of nanoparticle agglomerates. This study presents an investigation of sound-assisted fluidization of APF and ABF nanoparticle agglomerates and their fluidization characteristics, which are not only different from those observed using other fluidization methods for nanoparticle agglomerates, but are also different from sound- assisted fluidization of micron or sub-micron sized particles (Zhu *et al.,* 2004). The effects of sound frequency and sound pressure level on the fluidization behavior, such as the minimum fluidization velocity, bubbling regime, pressure drop across the bed, and bed expansion, will all be demonstrated in this study.

6.2 Magnetic Assisted Fluidization

One of the objectives of this study is to experimentally determine the fluidization behavior of a nanosized powder by applying an oscillating magnetic field to the nanoparticles that have been premixed with some very large magnetic particles. It is anticipated that the excitation of the magnets will provide sufficient energy to the system to overcome the interparticle forces and to form smaller agglomerates (fragment or break the very large agglomerates) that will fluidize smoothly at a lower minimum fluidization velocity. We believe that during fluidization there is a dynamic balance between fragmentation and re-agglomeration of the nanoagglomerates. This study aims to enhance the fragmentation of agglomerates, and avoid re-agglomeration.

Before describing our experiments using magnetically assisted fluidization of nanoagglomerates, it is important to review the previous work in this area. The idea of using a magneto-fluidized bed was first proposed in 1960 (Filippov, 1960) and became popular as a means of suppressing bubbles in gas fluidized beds for a variety of industrial applications, as reviewed by Rosensweig (1995), although the process never really became commercially viable. Other review papers describe the fundamental and practical development of magneto-fluidized beds (Liu *et al.* 1991; Ganzha and Saxena, 1998).

Generally, the particles to be fluidized were either magnetic particles or a mixture of magnetic and non-magnetic particles, and the magnetic field was usually generated by DC current (Arnaldos *et al.*, 1985;Wu *et al.,* 1997; Ganzha and Saxena 1998; Lu and Li 2000). For example, Arnaldos *et al.,* 1985 studied the fluidization behavior of a mixture of magnetic and non-magnetic particles of several hundred microns in size, such as sintered nickel-silica, steel-copper and steel-silica particles. The fluidization of larger (Geldart group D) particle mixtures of millimeter size, such as iron-copper shot of 0.935 to 1.416 mm in diameter is described in Wu *et al.,* 1997, and Lu and Li (2000) studied the fluidization of very fine (Geldart group C) particle mixtures of $CaCO_3$-Fe_2O_3 in a transverse rotating magnetic field. However, in all of these studies, the magnetic particles were fluidized along with the non-magnetic particles.

No studies have been found on the effect of adding large magnetic particles to a bed of nanoparticles for the purpose of disrupting the interparticle forces between the nanoparticles so that smooth fluidization of nanoagglomerates can occur. Here an investigation of the fluidization behavior of nanoparticle agglomerates with the assistance of millimeter-sized magnetic particles excited by an oscillating magnetic field is presented (Yu *et al.*, 2005). The effects of the intensity and frequency of the oscillating magnetic field and the weight ratio of magnets to non-magnetic APF and/or ABF nanoparticles on important fluidization parameters such as the minimum fluidization velocity, pressure drop across the bed, and bed expansion will be demonstrated in this part.

CHAPTER 7

SOUND ASSISTED FLUIDIZATION OF NANOPARTICLES

7.1 Experimental System

The experimental system for sound assisted fluidization includes a fluidized bed of nanoparticle agglomerates, flow and pressure measurement devices, a flow visualization system, a sound generation system and an optical sensor system for in-situ size measurement of agglomerates.

A schematic diagram of the experimental fluidization system for sound assisted fluidization is shown in Figure 7.1, and the real experimental system is shown in Figure 7.2. A 63 mm loudspeaker, powered by a sound excitation system (Bently Navada, Series 7000) with a signal generator, is installed on the top of the fluidized bed. A precision sound pressure level meter (Brüel & Kjær, Type 2232) is used to measure the sound pressure level. The sound excitation system is capable of generating a sound wave in the fluidized bed with a sound pressure level up to 125 dB. The sound frequency from the signal generator can be adjusted from 10 to 2MHz. Figure 7.3 is the response curve of the loud speaker, and working in a particular frequency range, from 80 Hz to about 1k Hz, the loudspeaker can generate a strong sound field, which is used to investigate the effect of sound on the fluidization behavior of nanoparticle agglomerates.

Figure 7.4 is the sound intensity distribution along the chamber (without nanoparticles). Because of the standing wave effect, the sound intensity varies along the chamber, but still, the sound field is relatively strong near the surface of the bed of nanoparticle agglomerates. Since we mostly care about the sound intensity near the fluidized bed surface, this type of sound intensity distribution is beneficial to our experiments.

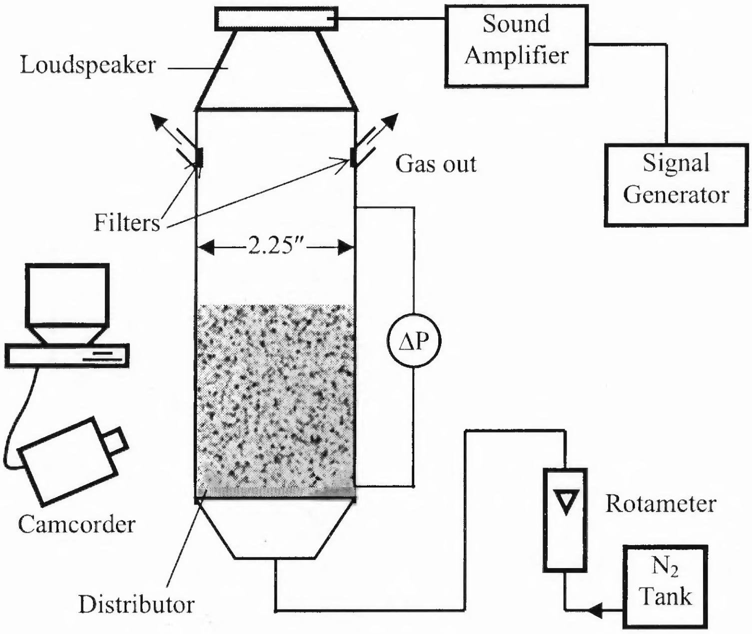

Figure 7.1 Systematic diagram of experimental system for sound assisted fluidization of nanoparticles.

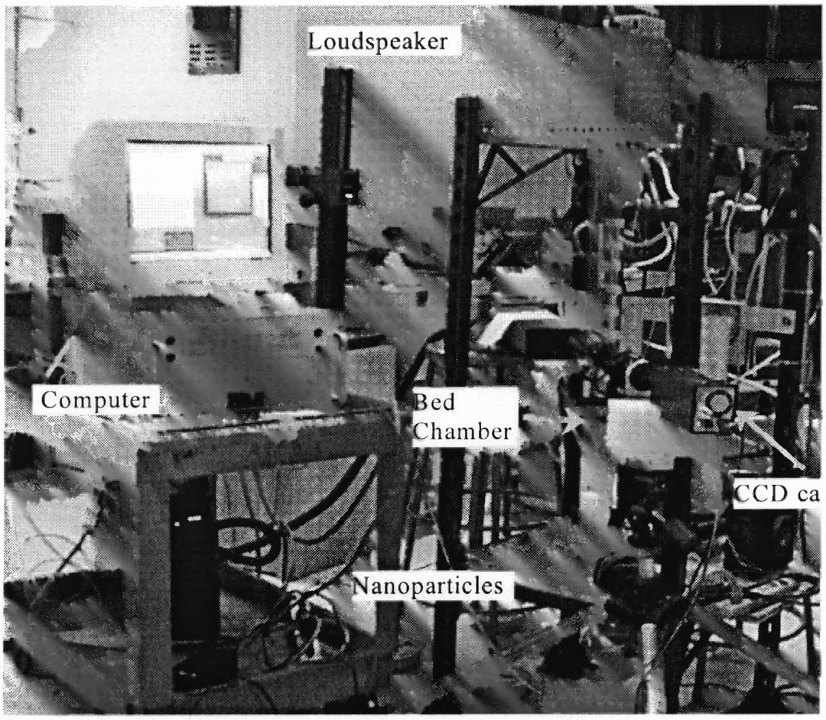

Figure 7.2 Experimental system for sound assisted fluidization of nanoparticles.

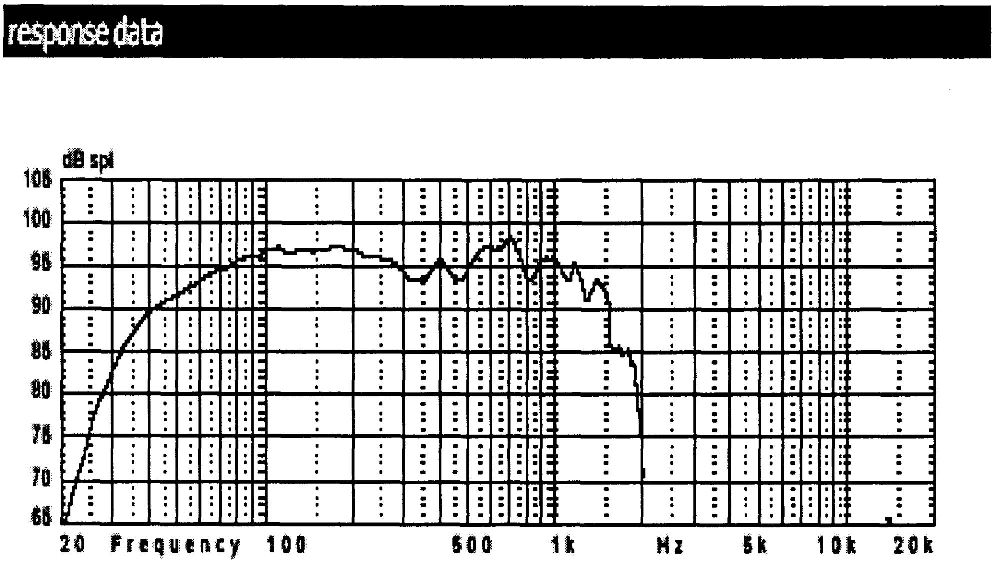

Figure 7.3 Loudspeaker frequency responses

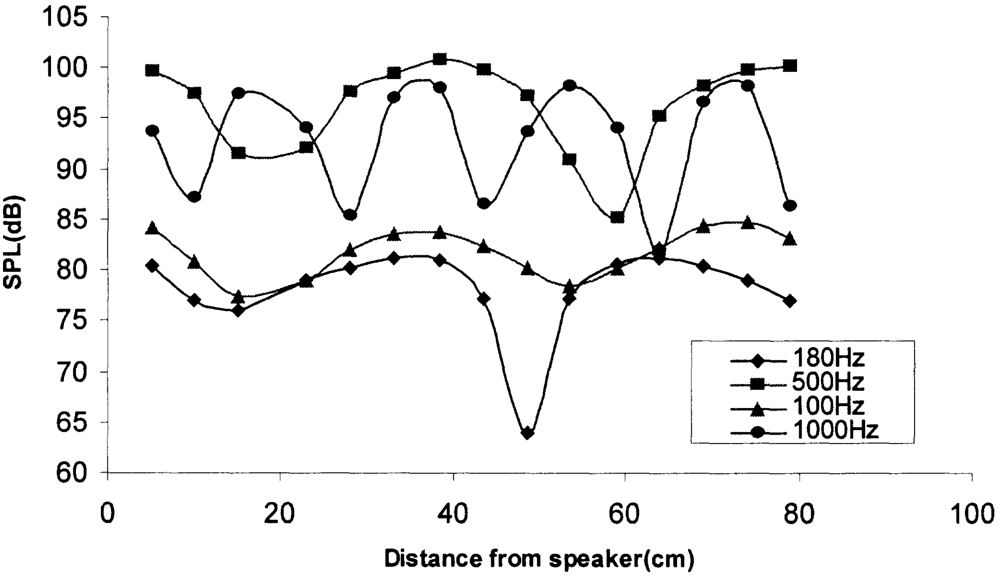

Figure 7.4 SPL distributions along chamber at different frequencies.

The fluidized bed of nanoparticle agglomerates, the flow and pressure measurement devices, the flow visualization system, the optical sensor system for in-situ size measurement of agglomerates, and the preparation of nanoparticles are the same as those described for the conventional fluidization system, which is found in Chapter 3. Using the above sound generating system with the fluidization system, a series of experiments using APF and ABF nanoparticle agglomerates are conducted.

7.2 Results and Discussion

7.2.1 Fluidization Behavior

Typical bed behavior of SiO_2 nanoparticle agglomerates (Degussa Aerosil® SiO_2 R974, APF) with and without sound excitation is shown in Figure 7.5. The nanoparticle agglomerates were first lifted in a slugging mode and then the bed disintegrated to form stable channels. The bed expands slightly with an uneven surface, as shown in Figure 7.5(a). Once a sufficiently strong sound field is applied, the bed collapses in a couple of seconds, the channels disappear, and the bed expands rapidly and uniformly until it reaches its full expansion. A homogenous fluidization state is easily established, as shown in Figure 7.5(b).

For ABF nanoparticles, the fluidization behavior shows similar improvement, but the improvement is not significant as for APF nanoparticles.

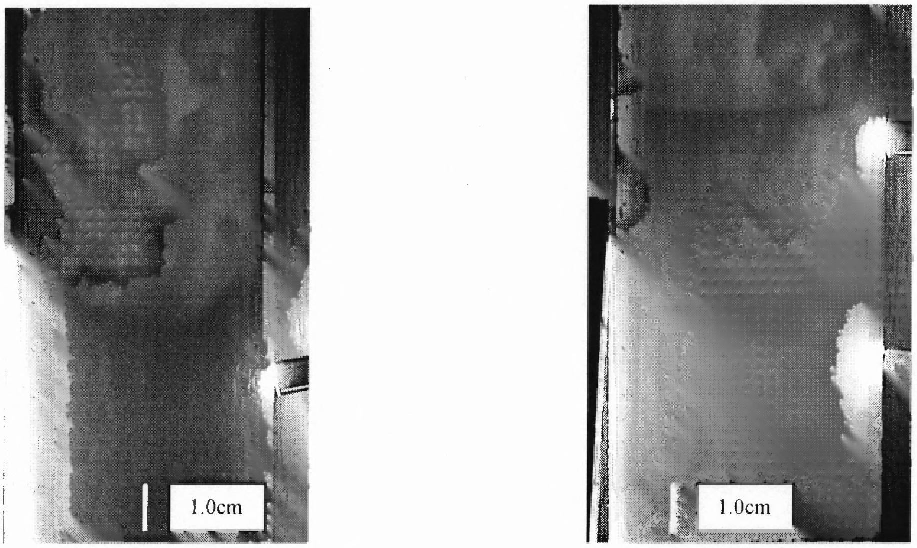

(a) Without sound (b) With sound, 100Hz, 122dB, Uair=0.054cm/s

Figure 7.5 Fluidization of SiO_2 nanoparticles.

7.2.2 Minimum Fluidization Velocity

For Degussa Aerosil® SiO_2 R972 (APF nanoparticles without sieving), Figure 7.6 illustrates the relationships between superficial gas velocity and bed height and bed pressure drop, and shows a substantial reduction of the minimum fluidization velocity when the sound with a frequency of 100 Hz and nearly 140 dB was turned on. Without acoustic agitation, the minimum fluidization velocity is around 1.2 cm/s, while with acoustic agitation it reduces to 0.62 cm/s. For both cases, the bed expansion increases linearly with gas velocity when it is over their minimum fluidization velocity. Figure 7.6 also shows that before fluidization the pressure drop for the no-sound case remains constant for a certain superficial gas velocity range. When the gas velocity reaches a certain value, some channels will form. Therefore, the extra gas accompanied with a further increase in gas velocity will pass through these channels and will have no effect on the pressure drop across the bed, until the break-up force created by the gas flow in the channels is high enough to destroy the channels and fluidize the bed. After the bed is fully fluidized, the pressure drop approximately equals the bed weight.

A similar improvement can be found for ABF nanoparticles as shown in Figure 7.7, which is a comparison of pressure drop and bed height with and without sound excitation for Degussa Aerosil® TiO_2 P25 (ABF nanoparticles). With the assistance of sound, bed expansion increases and the minimum fluidization velocity decreases.

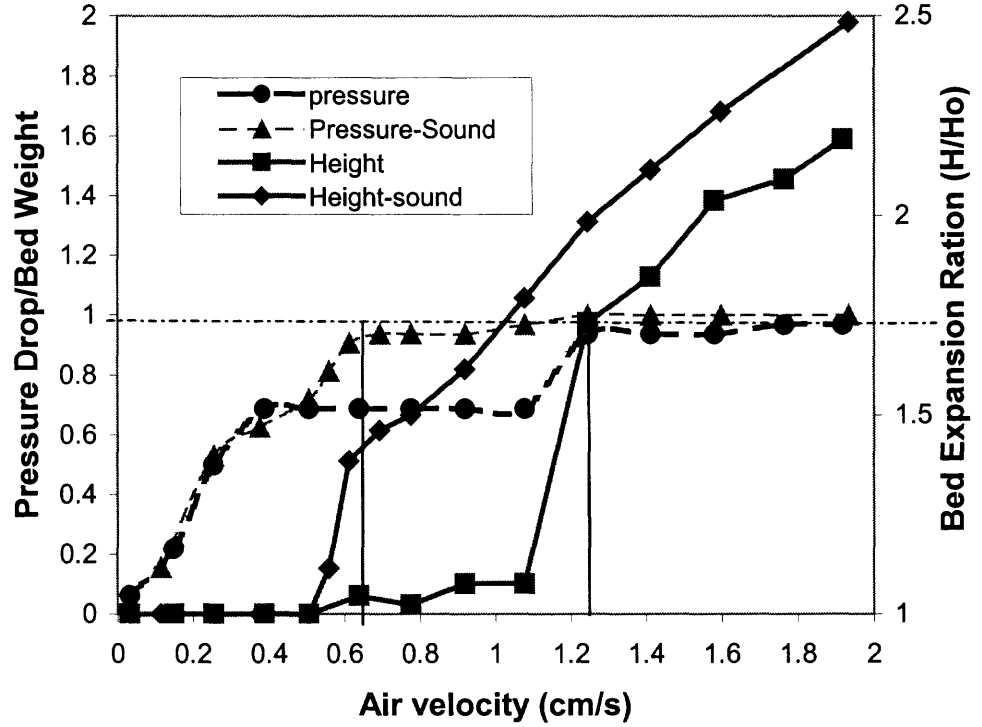

Figure 7.6 Bed expansion with and without sound excitation for APF nanoparticles. Degussa Aerosil® R972, SiO_2,16nm.

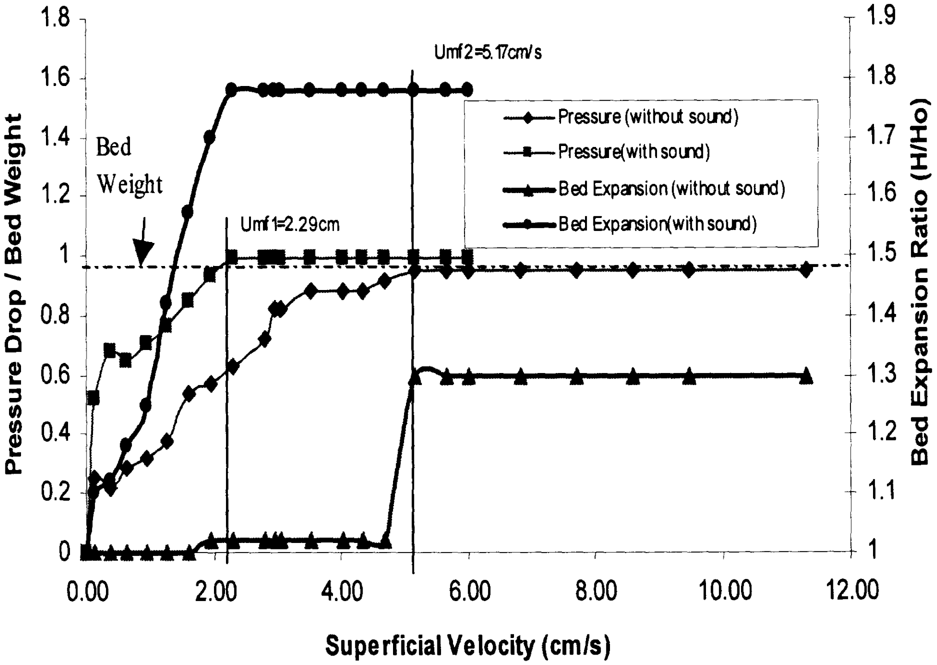

Figure 7.7 Bed expansion with and without sound excitation for ABF nanoparticles. Degussa Aerosil® P25, TiO_2, 21nm.

The effect of acoustic agitation on the minimum fluidization velocity of different nanoparticles is listed in Table 7.1.

Table 7.1 Minimum fluidization velocities of nanoparticle agglomerates (U_{mf}) with and without sound excitation (120 dB, 200 Hz).

Nanoparticle	U_{mf} (cm/s) Without sound	U_{mf} (cm/s) With sound (120 dB, 200 Hz)
SiO_2 R972 (APF)	1.2	0.6
SiO_2 R104 (APF)	1.1	0.6
SiO_2 R805 (APF)	0.65	0.3
SiO_2 COK 84 (APF)	1.0	0.6
TiO_2 P25 (ABF)	5.2	2.1

For sieved nanoparticle (fine agglomerates sieved by a 500 μm sieve), sound excitation also can improve the fluidization quality, decrease the minimum fluidization velocity and increase the bed expansion. Typical fluidization characteristics of sieved nanoparticles, including minimum fluidization velocities, bed expansions and bed pressure drops with and without sound excitation are illustrated in Figure 7.8 and Figure 7.9. With the aid of sound, a substantial reduction in the minimum fluidization velocity can be observed. For Degussa Aerosil® R974, the minimum fluidization velocity is reduced from 0.14 cm/s in the absence of sound to 0.054 cm/s with sound excitation. Here, the minimum fluidization velocity is defined as the gas superficial velocity beyond which the bed pressure drop is no longer dependent upon the gas velocity and becomes constant.

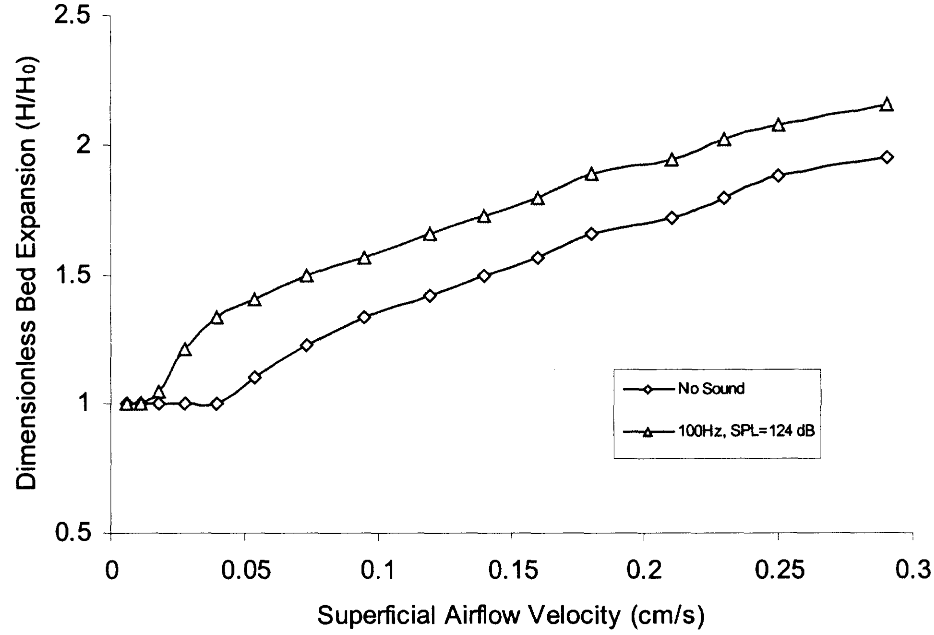

Figure 7.8 Bed expansions with and without sound excitation. (Degussa Aerosil® R974, fine agglomerates sieved by 500 μm sieve, H_0 is the initial bed height, which is 12.0 cm in this study)

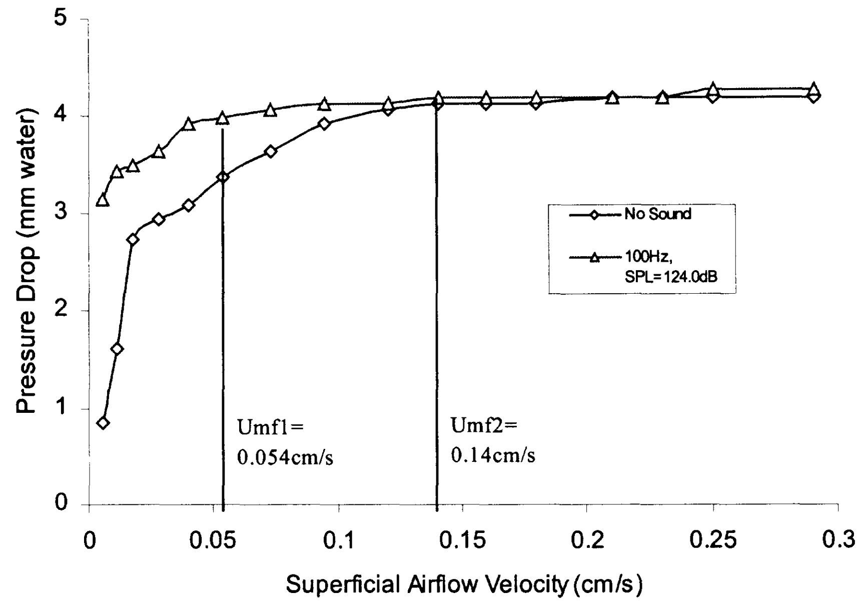

Figure 7.9 Pressure drop with and without sound excitation. (Degussa Aerosil® R974, fine agglomerates sieved by 500 μm sieve, U_{mf1} is the minimum fluidization velocity with sound agitation; U_{mf2} is the minimum fluidization velocity without sound agitation.)

To summarize, typical fluidization characteristics, including minimum fluidization velocities, bed expansions and bed pressure drops with and without sound excitation are shown in the above Figures and Table. A substantial reduction in the minimum fluidization velocity with the aid of sound can be observed. For APF nanoparticle, DeGussa Aerosil® R972, the minimum fluidization velocity is reduced from 1.2 cm/s in the absence of sound to 0.6 cm/s with sound excitation. For ABF nanoparticles, Degussa Aerosil® P25, TiO_2, the minimum fluidization velocity is reduced from 5.2 cm/s in the absence of sound to 2.3 cm/s with sound excitation.

As mentioned earlier, at low gas velocities, only slugging and channeling occur in a fluidized bed of nanoparticle agglomerates while, at sufficiently high gas velocities, the bed can be fluidized smoothly. Fluidization of nanoparticle agglomerates occurs due to the effective breakup of large agglomerate clusters by the large hydrodynamic forces at high gas velocities. With the aid of sound, the breakup of large agglomerate clusters takes place due to a combined effect of hydrodynamic forces and acoustic excitation. A more comprehensive explanation of this combined effect requires further experimental and modeling efforts.

7.2.3 Effects of Sound Frequency

Figure 7.10 shows a series of representative snapshots of the fluidizing bed at different sound frequencies. At a fixed sound level output (e.g., 125 dB in Figure 7.10), the bed of nanoparticle agglomerates can only be fluidized in a relatively narrow band of low sound frequency from 20 to 1000 Hz. Furthermore, bubbles appear in an even narrower range, 200-600 Hz, and as seen in Figure 7.10, both the occurrence of bubbling and the bubble size are strongly dependent on the sound frequency. Due to the relatively high bed voidge observed when fluidizing nanoparticle agglomerates, in the bubbling fluidization regime, the bubble size and the bubble rising velocity can be easily determined using our visualization technology. The bed expansion is also strongly dependent on the sound frequency, as seen in Figure 7.11. It appears that both bed expansion and bubble formation could be linked to the wave modes of the sound in the bed, the resonance frequencies of the agglomerate clusters, and the resonance frequencies of the bed.

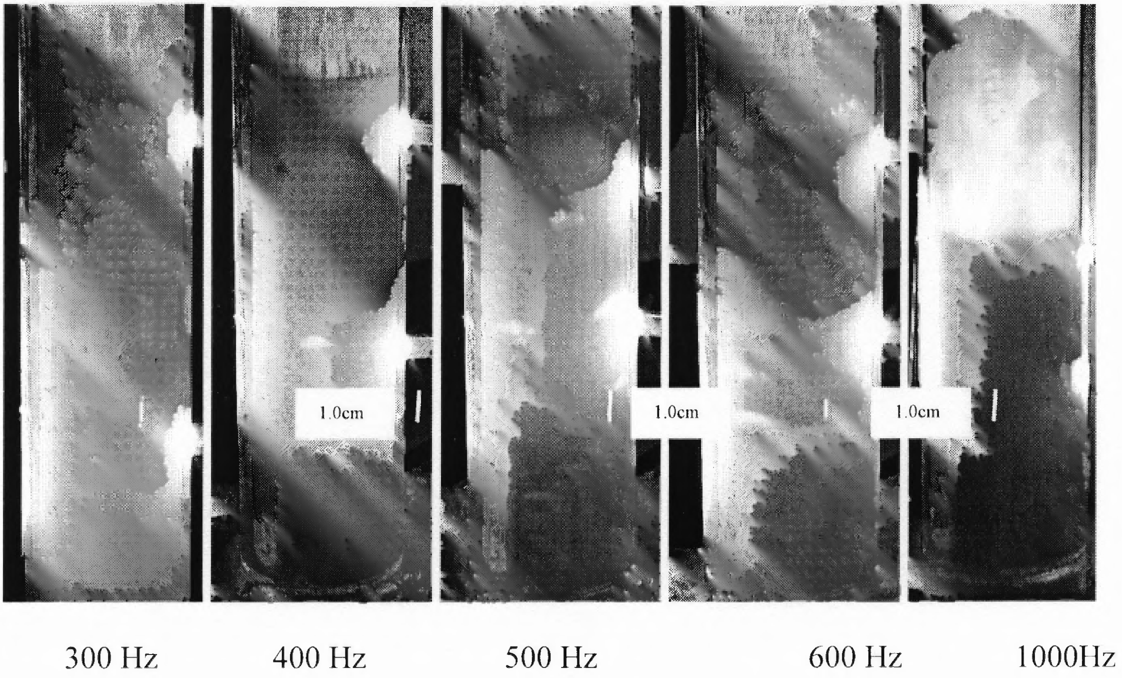

Figure 7.10 Fluidization at different frequencies. (Degussa Aerosil® R974, fine agglomerates sieved by 500 μm sieve, SPL=125 dB, Uair=0.1cm/s)

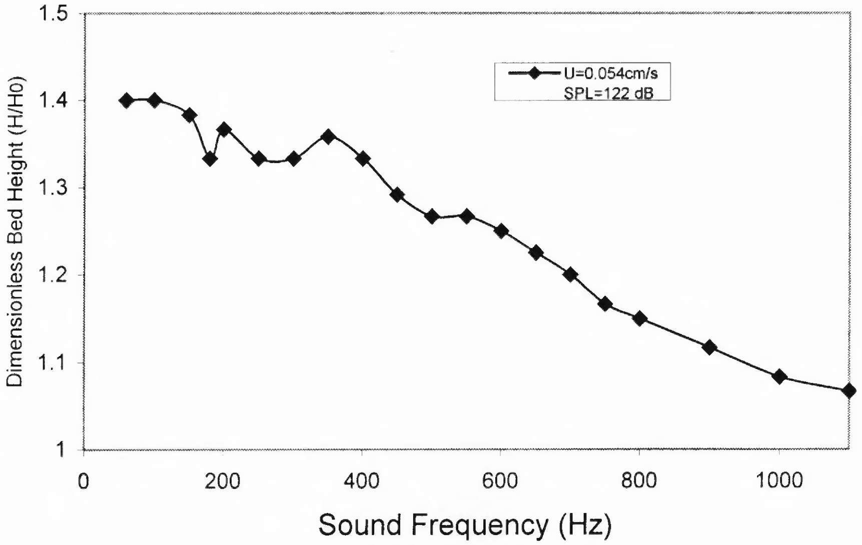

Figure 7.11 Effect of sound frequency on bed expansion. (Degussa Aerosil® R974, fine agglomerates sieved by 500 μm sieve, H_0 is the initial bed height, which is 12.0 cm in this study)

7.2.4 Effects of Sound Pressure Level (SPL)

The effect of sound pressure level on the bed expansion is shown in Figure 7.12. It is noted that below a critical value of sound pressure level (e.g. 112 dB at 100Hz and 105dB at 400Hz in Figure 7.12), there is no fluidization. The critical sound pressure level appears to be a function of sound frequency. The bed expansion increases monotonically as the sound pressure level increases in the range of our study. The bed expansion may be related to the balance between agglomerate breakup and re-agglomeration of the nanoparticles.

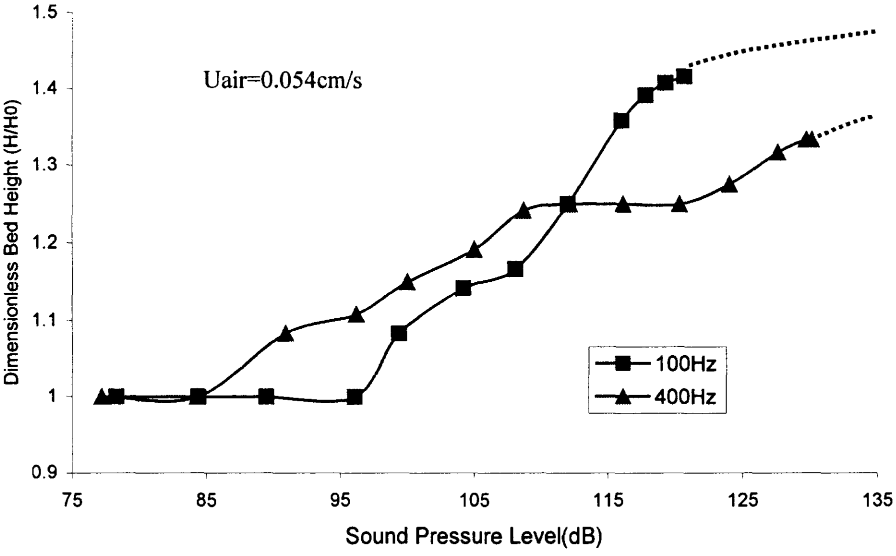

Figure 7.12 Effect of sound pressure level on bed expansion. (Degussa Aerosil® R974, fine agglomerates sieved by 500 μm sieve, H_0 is the initial bed height, which is 12.0 cm in this study)

7.2.5 Agglomerate Size Measurement

If we let the laser beam illuminate the powder bed near the inside surface of the acrylic wall, which ensures enough light for taking pictures, we can measure the agglomerate size inside the fluidized bed. One of the captured images is shown in Figure 7.13a. It is noted that the typical agglomerate size roughly ranges from 200 to 300 μm.

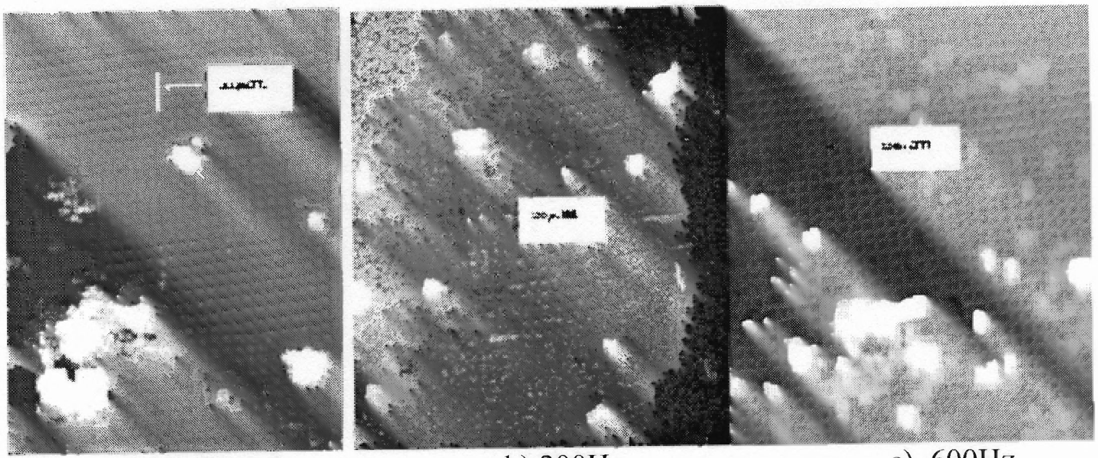

a) No Sound. b) 200Hz. c) 600Hz.

Figure 7.13 Effect of sound on agglomerate size (Degussa Aerosil® R974).

The effect of sound on the agglomerate size is shown in Figure 7.13. With sound, the average agglomerate size is smaller that that observed in the absence of sound. This can partially explain why the minimum fluidization velocity is reduced when sound is added.

7.2.6 Concluding Remarks

Experiments have been carried out to determine the effects of sound frequency and intensity on the bed behavior, such as the minimum fluidization velocity, pressure drop across the bed, and bed expansion. It is found that the external forces induced by the acoustic field can overcome the cohesive van der Waals forces so that large nano-agglomerates break into smaller agglomerates, which can be fluidized smoothly and homogeneously with negligible elutriation.

Experimental results show that for the APF nanoparticles, with the assistance of a sound field, the minimum fluidization velocity can be reduced from around 1.0 cm/s to 0.3~0.6 cm/s, and bed expansion increased; for the ABF nanoparticles, with the assistance of a sound field, the minimum fluidization velocity can be reduced from over 5.0 cm/s to about 2.3 cm/s, the fluidization quality can be improved, and the bed expansion also increased.

Varying both the sound intensity and sound frequency result in dramatic changes in the quality of the fluidization. Within a certain range of the sound frequency, typically from 200 to 600 Hz, bubbling fluidization occurs. Both the bed expansion and the bubble characteristics are strongly dependent on the sound frequency and sound pressure level. However sound has almost no impact on fluidization, when the sound frequency is extremely high, above 2000 Hz. A relatively high sound pressure level (such as 115 dB) is needed to initiate the fluidization. Experiments also show that different types of nanoparticles display very different fluidization characteristics. The agglomerate size has also been measured, and we found that with sound assistance the average diameter of the agglomerates are significantly reduced.

7.2.7 Limitation of this Study and Future Research Directions

More comprehensive experimental studies on the effect of external sound excitation on fluidization of nanoparticle agglomerates are needed, and more types of nanoparticles should be tested. It is also necessary to better understand the mechanism of external sound excitations on the fluidization of nanoparticles; for example, why are large bubbles observed at certain frequencies whereas no bubbles are seen at both lower and higher frequencies. Mathematical modeling and numerical simulations needs to be done to explain this and other puzzling experimental observations.

CHAPTER 8

MAGNETIC ASSISTED FLUIDIZATION OF NANOPARTICLES

8.1 Experimental System

A schematic diagram of the experimental fluidization system for magnetic assisted fluidization is shown in Figure 8.1. The magnetic particles are barium ferrite (BaO-$6Fe_2O_3$) coated with polyurethane (supplied by Aveka, USA) and have a size about 1.0-3.0 mm. Before each experiment, the magnetic particles are recharged by contacting a permanent magnet to ensure the same magnetic properties. They are then added to the bed of nanoparticles at a given mass of magnets. The shafts of two 1/20 HP electric motors (Dayton 5M064B) are removed and the electromagnetic coils are placed opposite one another around the lower part of the vertical transparent column by mounting them on the acrylic plate which holds the distributor, as shown in Figure 8.1. An oscillating magnetic field can be generated by an adjustable AC power (Triathion Precision AC Source), with intensity up to 140 Gauss at the center of the field. A strong cooling fan (Comair Rotron TNE2A) is used to prevent the coils from overheating. A gauss meter (Walker Scientific Inc. MG-3A) with the magnetic field intensity measurement range from 1 to 10^4 G is used to measure the intensity of the oscillating magnetic field. The intensity is measured at the center point between the coils in the empty column (before charging the nanoparticles into the bed). Figure 8.2 is the picture of the actual experimental system, and Figure 8.3 is the photograph of the Gauss meter.

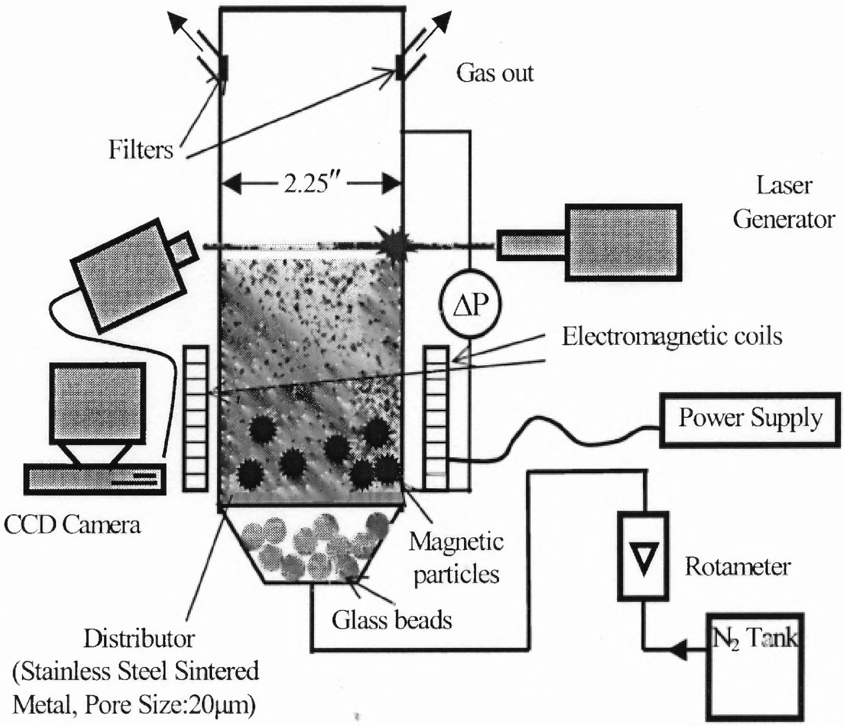

Figure 8.1 Systematic diagram of experimental system for magnetic assisted fluidization of nanoparticles.

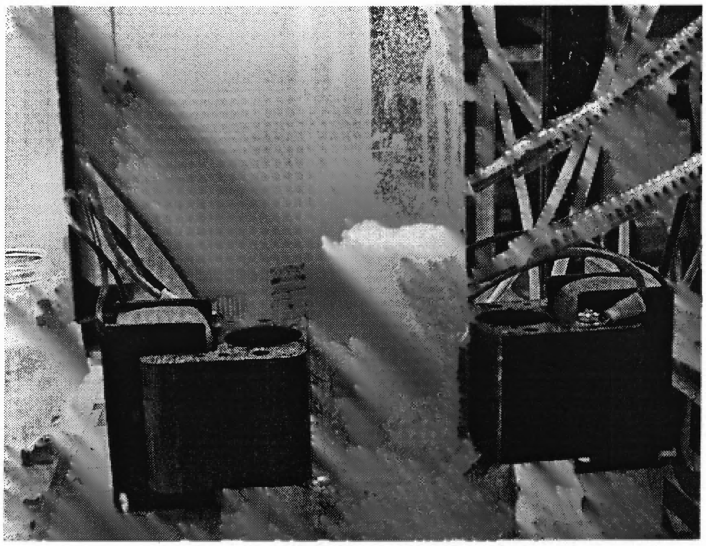

Figure 8.2 Experimental system of magnetic assisted fluidization.

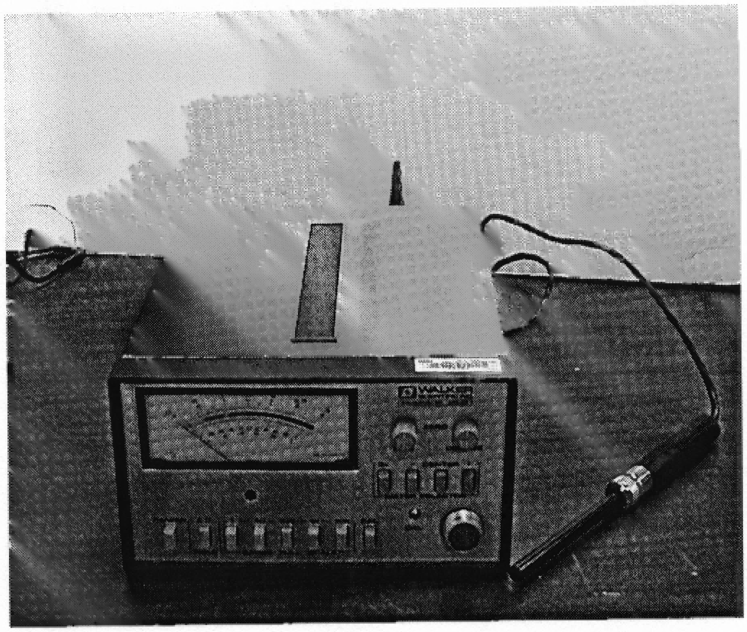

Figure 8.3 Gauss Meter.

Table 8.1 shows the intensity of the oscillating magnetic field of an empty bed measured by the Gauss Meter, and Figure 8.4 is the locations of the measuring points (top view of the empty chamber). In this study, then intensity of the magnetic field at the center of the bed (Point 0) is selected as the reference.

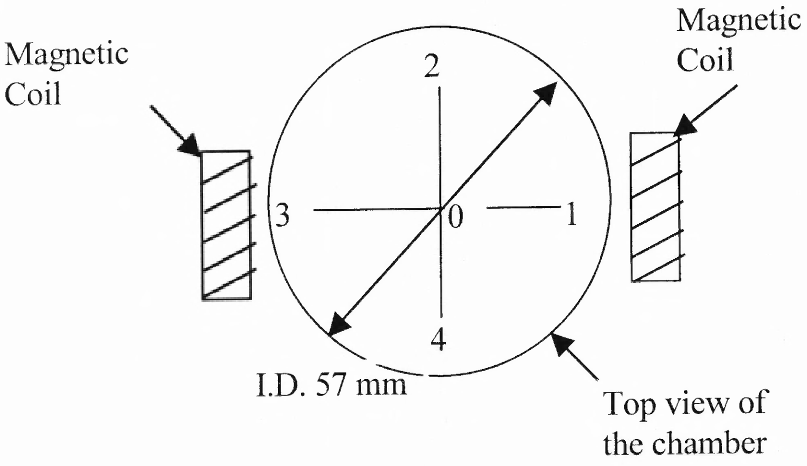

Figure 8.4 Locations of the magnetic field intensity measuring points.

Table 8.1 Intensity of the magnetic field at different locations.

Point	0	1	2	3	4
Magnetic Field Intensity (Gauss)	80	100	50	120	50

The fluidized bed of nanoparticle agglomerates, the flow and pressure measurement devices, the flow visualization system, the optical sensor system for in-situ size measurement of agglomerates, and the preparation of nanoparticles are the same as those of the conventional fluidization system described in Chapter 3. Using the above magnetic generating system with the fluidization system, a set of experiments by use of APF and ABF nanoparticle agglomerates mixed with the millimeter size permanent magnetic particles in oscillating magnetic field are conducted, and the corresponding results will be discussed in next section.

8.2 Results and Discussion

8.2.1 Visualization of Magnetic Assisted Fluidization

Before the experiments, the Degussa Aerosil® R974 particles were sieved using a shaker (Octagon 2000) and a 35-mesh sieve opening (about 500 μm). In this study, the smaller nanoagglomerates, which pass through the openings of the 500 μm sieve are designated as "soft" and the larger agglomerates, from about 500 μm to more than 10 mm, as "hard". These two different sized agglomerates and a "mixture" consisting of 80% soft agglomerates and 20% hard agglomerates by weight (80/20) were selected to conduct the fluidization experiments.

It has been found that, even when using the same nanoparticles, if we select agglomerates of different sizes, the bed will show very different fluidization behavior.

For example, the soft R974 agglomerates fluidize smoothly with large bed expansion (APF) at a low minimum fluidization velocity of 0.23 cm/s. The mixture consisting of 80% soft agglomerates and 20% hard agglomerates (80/20) also behaves as APF, but the minimum fluidization velocity is much higher (5.67 cm/s) than that of the soft agglomerates. However, the hard R974 agglomerates do not fluidize at all, even at a gas velocity as high as 13.2 cm/s. At this high gas velocity, significant particle elutriation was observed, and the fluidization experiment had to be interrupted to avoid sever losses of nanoparticles.

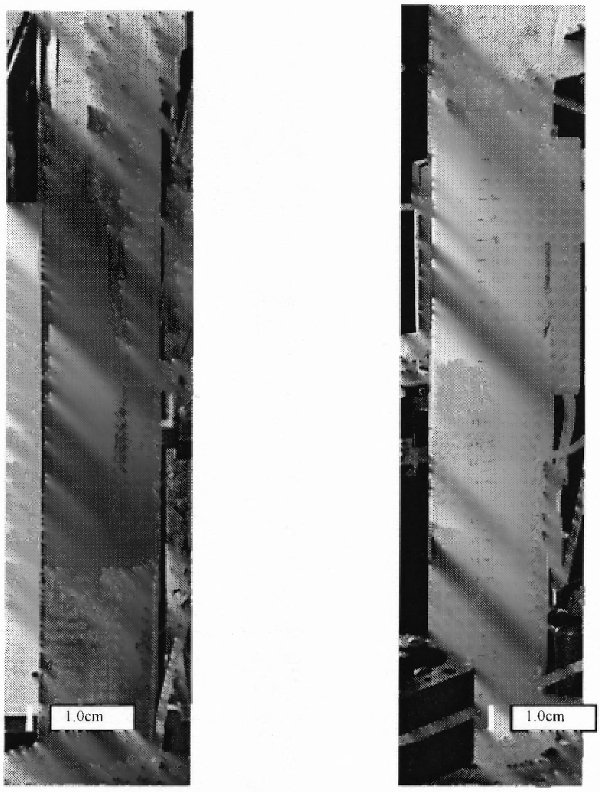

(a) Without magnetic field

(b) With magnetic field, 140G, 60Hz, mass of magnets 20.0 g.

Figure 8.5 Fluidization of SiO_2 nanoparticles at Ugas=0.65cm/s. (Degussa Aerosil® R974, 80/20 mixture)

Typical fluidization behavior of the 80/20 mixture of SiO_2 nanoparticle agglomerates with and without the external oscillating magnetic excitation is shown in Figure 8.5. Without the external oscillating magnetic excitation, at a superficial gas velocity of 0.65 cm/s (Figure 8.5a), the nanoparticle agglomerates are first lifted as a plug and then the plug disintegrates to form stable channels through which the gas passes; the bed expands slightly with an uneven surface and the pressure drop is much less than the bed weight, indicating that the nanoagglomerate bed is not fluidized.

However, if a sufficiently strong oscillating magnetic field is applied, the magnetic particles are set into motion (translation and rotation) and the nanoparticle agglomerates are fragmentized into smaller agglomerates because of collisions with the magnets, the vessel wall, and the distributor. After a few minutes, the channels disappear, and the bed begins to expand slowly and uniformly until it reaches its full expansion, of up to 5 times the initial bed height, and at the same time, the pressure drop reading is very close to the weight of the bed, indicating a full bed fluidization. A homogenous fluidization state is established, as shown in Figure 8.5b, and the surface is very smooth and even. A further visual examination of the powder after the magnetic fluidization shows a much smaller averaged agglomerate size, with only a few large hard agglomerates left.

Cabot Carbon Black ® PEARLS 2000 is a pelletized powder, and the average size of the carbon black pellets or granules is around 800 μm. As mentioned in Chapter 5, the Cabot Carbon Black ® PEARLS 2000 after sieving through a 500 μm sieve show typical APF fluidization. But the fresh Cabot Carbon Black ® PEARLS 2000 without sieving process show a typical ABF fluidization. In this study, the fresh Cabot Carbon

Black ® PEARLS 2000 without sieving process is selected as a representative ABF nanoparticle to be tested for comparison with and without magnetic excitation.

For some ABF nanoparticles (Degussa Aerosil® TiO_2 P25, and Degussa Aerosil® SiO_2 A90), there is no significant improvement observed by introducing magnetic excitation. But for some other types of ABF nanoparticles (fresh Cabot Carbon Black ® PEARLS 2000 without sieving), the improvement in the fluidization quality is significant. Without the assistance of magnetic excitation, we observed a typical ABF fluidization behavior, i.e., very high gas velocity (Umf=27.6 cm/s) required, strong bubbling, bed expansion only around 60%, and the fluidization has to be stopped due to the huge loss of particles (10% loss within minutes). With the assistance of magnetic excitation, within 15 minutes, we observed typical APF fluidization behavior; the bed begins to expand up to 5 or more times at low gas velocity (Umf= 1.93), an extremely smooth uniform fluidization is achieved, and bubbling disappeared, and no elutriation is observed. Due to the magnetic assistance the original large agglomerates are fragmentized into much smaller agglomerates and the fluidization qualify is significantly improved. Figure 8.6 shows pictures of the powder bed at agas velocity of 2.78 cm/s, with and without magnetic excitation.

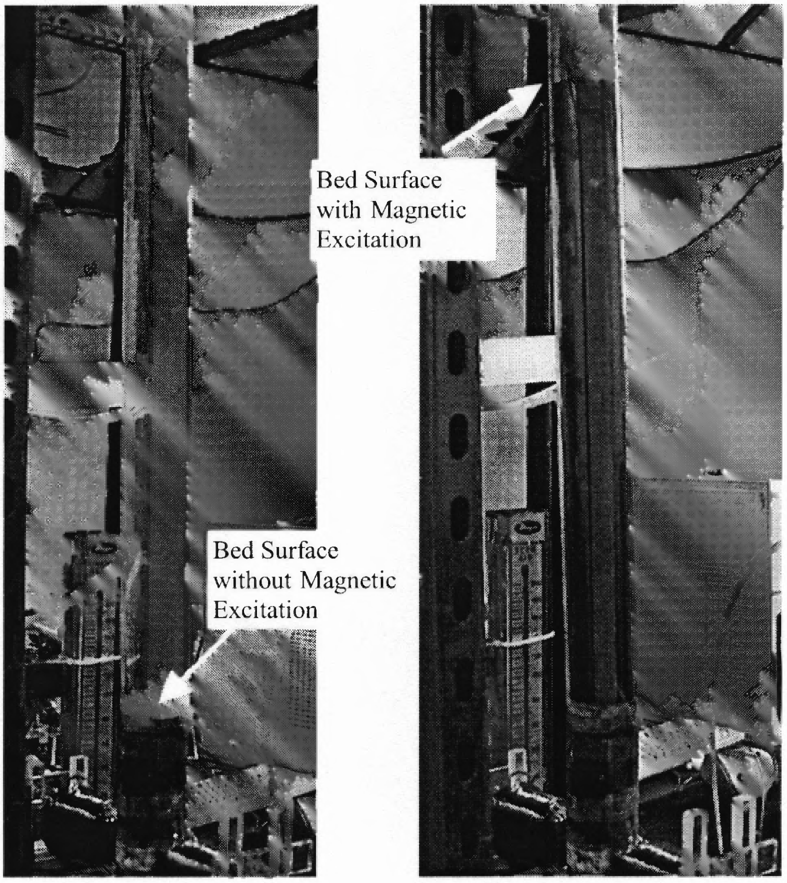

Bed Surface with Magnetic Excitation

Bed Surface without Magnetic Excitation

Figure 8.6 Images of bed expansion of Carbon Black (Cabot ® PEARLS 2000) with and without magnetic excitation. Initial bed height = 12.0 cm, mass of carbon black particle = 60.0 grams.

(a) Without magnetic excitation, Ugas=2.78 cm/s;
(b) With magnetic excitation, Ugas=2.78 cm/s. Intensity of magnetic field ~ 200 Gauss, mass of magnetic particles 30.0 grams, 60 Hz AC.

8.2.2 Minimum Fluidization Velocity and Bed Expansion

8.2.2.1 APF Nanoparticles

The pressure drop normalized with the bed weight per unit area and the bed expansion ratio as a function of superficial gas velocity through the bed is shown in Figure 8.7 with and without magnetic excitation for the 80/20 mixture of Degussa R974 nanoparticles. It is seen that magnetic excitation causes the bed to expand almost immediately as the velocity is increased and the bed fluidizes at a velocity more than one order of magnitude lower than that without magnetic assistance. In this section and next section, Degussa Aerosil® R974 is chosen as a typical APF nanoparticle.

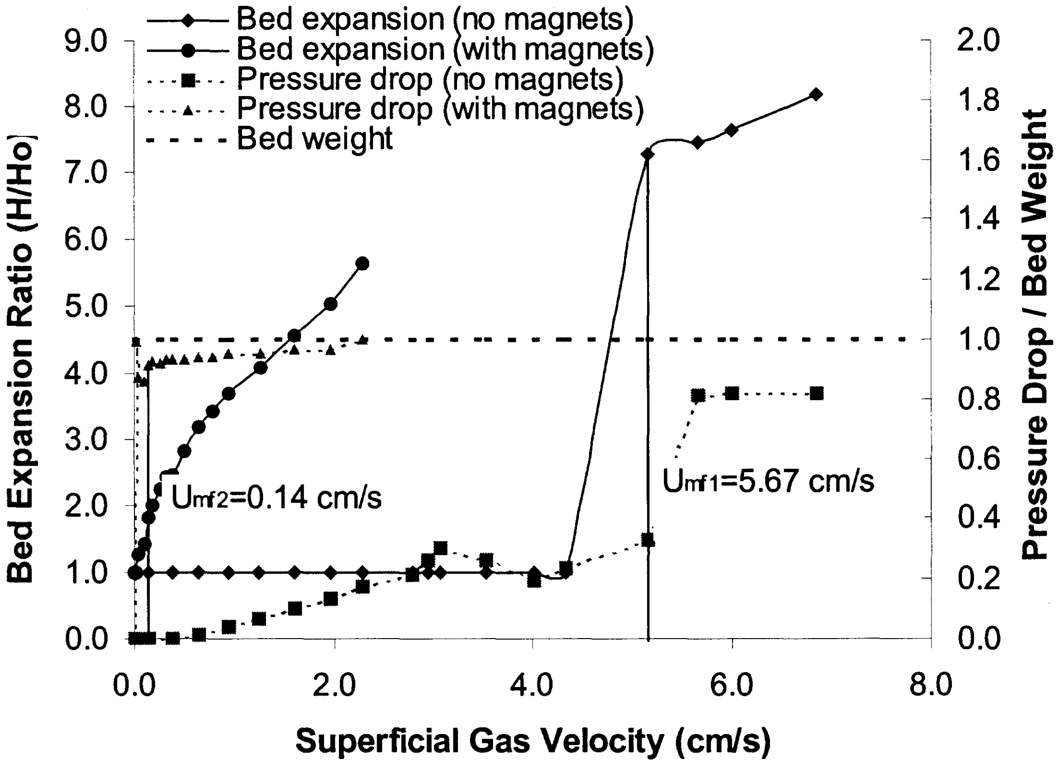

Figure 8.7 Bed expansion ratio and pressure drop for 80/20 mixture with and without magnetic excitation. (Solid lines are the bed expansion ratios, and dashed lines are the pressure drops)
(Magnetic field intensity 140G at the center of the field, mass of magnets 20.0 g, AC frequency 60 Hz.)

Umf1: minimum fluidization velocity without magnetic excitation;
Umf2: minimum fluidization velocity with magnetic excitation.

After separation from the magnetic particles (using a magnetic separator), the nanoparticle agglomerates are put back into the column, and a second fluidization experiment without magnetic assistance is conducted using these agglomerates. Figure 8.8 is a comparison of the fluidization characteristics of the 80/20 mixture before and after magnetic processing. A significant reduction in the minimum fluidization velocity from 5.67 cm/s to 1.25 cm/s is observed, indicating that previous fluidization with magnetic assistance causes the agglomerates to be fragmented into smaller ones and the average agglomerates size is reduced. However, the minimum fluidization velocity of these smaller agglomerates is still about an order of magnitude larger than the minimum fluidization velocity observed when the magnetic assistance is turned on.

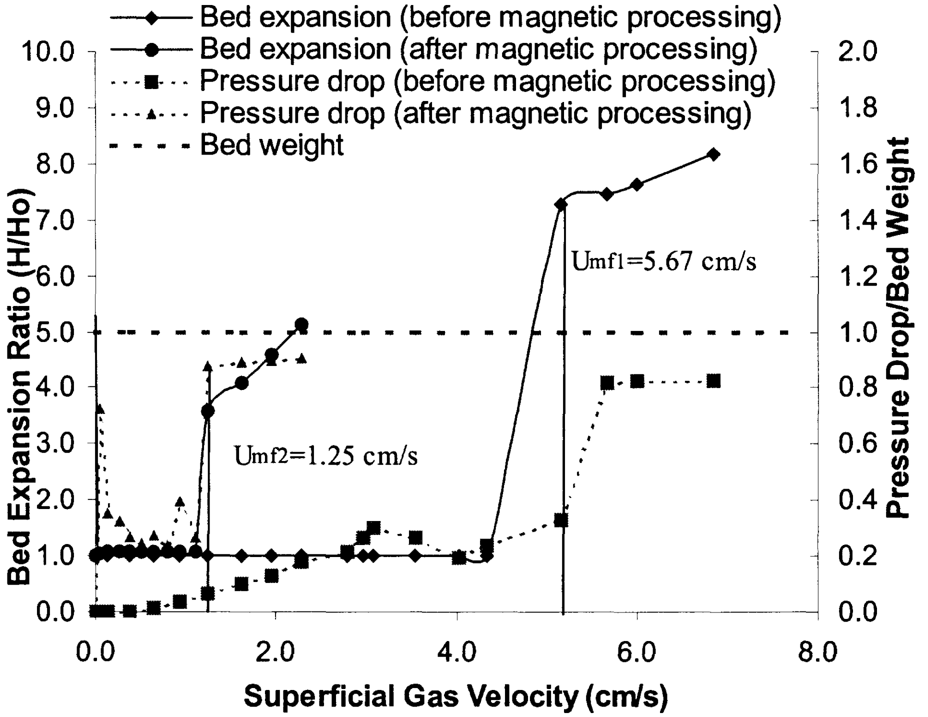

Figure 8.8 Bed expansion ratio and pressure drop for conventional fluidization of 80/20 mixture before and after magnetic processing. (Solid lines are the bed expansion ratios, and dashed lines are the pressure drops)
(Magnetic field intensity 140G at the center of the field, mass of magnets 20.0 g, AC frequency 60 Hz.)
Umf1: minimum fluidization velocity before magnetic "fragmentation" processing;
Umf2: minimum fluidization velocity after magnetic "fragmentation" processing.

The fluidization behavior of the soft agglomerates is shown in Figure 8.9. These much smaller agglomerates fluidize well with and without magnetic excitation. In both cases, the minimum fluidization velocities appear to be quite close to each other, and at higher gas velocities (above minimum fluidization velocity) the bed expansion with magnetic assistance is higher than that without magnetic assistance. It should also be noted that the ratio of the measured pressure drop to the weight of the bed per unit area is below unity for magnetic assisted fluidization. This indicates that some of the nanoagglomerates may not participate in the fluidization and may stick to the magnets or the distributor.

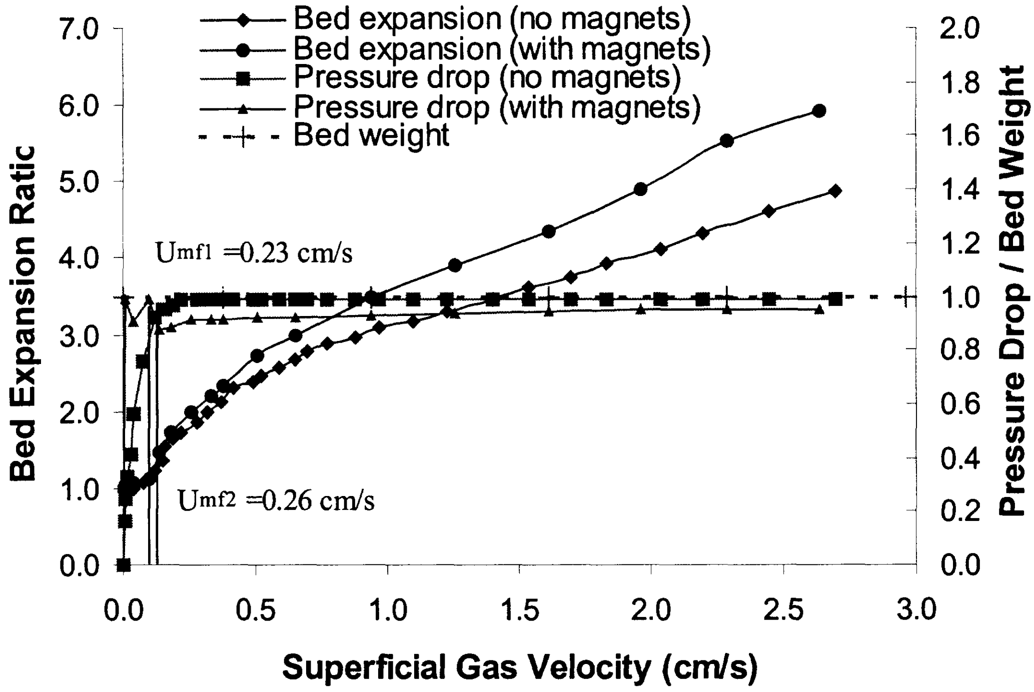

Figure 8.9 Bed expansion ratio and pressure drop for soft agglomerates with and without magnetic excitation. (Solid lines are the bed expansion ratios, and dashed lines are the pressure drops)
(Magnetic field intensity 140G at the center of the field, mass of magnets20.0 g, AC frequency 60 Hz.)
Umf1: minimum fluidization velocity without magnetic excitation;
Umf2: minimum fluidization velocity with magnetic excitation.

Figure 8.10 shows the typical fluidization behavior (pressure drop and bed expansion) of hard SiO_2 nanoparticle agglomerates (R974) with and without magnetic excitation. The size of the hard agglomerates is in a wide range from 0.5mm to about

10mm. Without the magnetic excitation, even at a superficial gas velocity as high as 13.2 cm/s, the hard agglomerates are hardly fluidized. Visual observation reveals that the smaller hard agglomerates are in motion at the top of the bed, but the larger agglomerates remain motionless near the bottom of the bed, causing the gas to flow in large channels between them. The bed shows almost no expansion (see Figure 8.11a) and the pressure drop is much less than the bed weight, indicating that the bed is not fluidized.

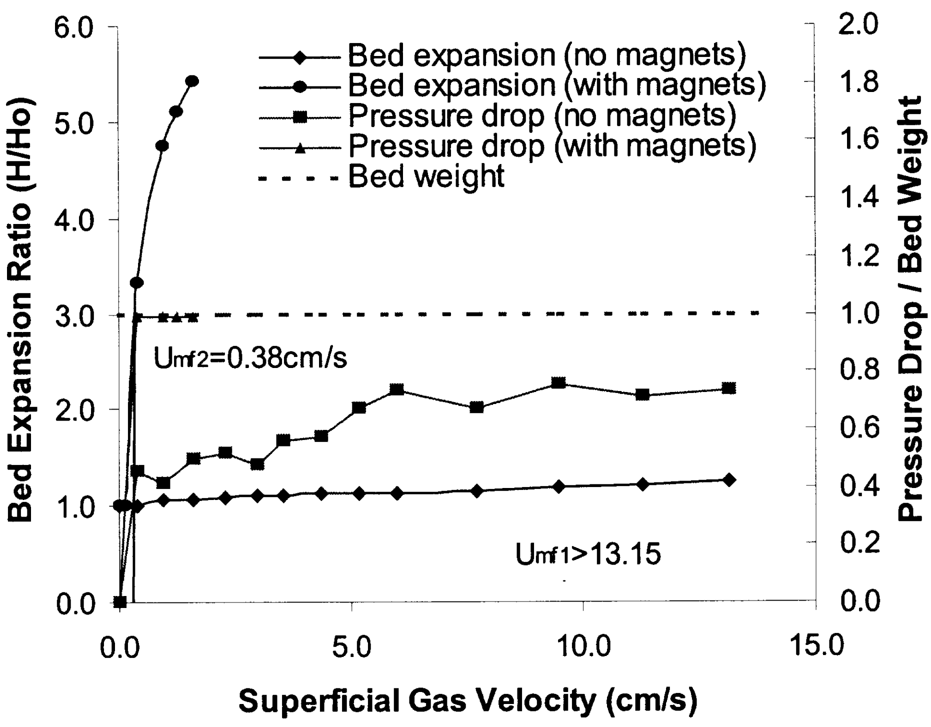

Figure 8.10 Bed expansion ratio and pressure drop for hard agglomerates with and without magnetic excitation. (Solid lines are the bed expansion ratios, and dashed lines are the pressure drops) (Magnetic field intensity 140G at the center of the field, mass of magnets 20.0 g, AC frequency 60 Hz)

Umf1: minimum fluidization velocity without magnetic excitation;

Umf2: minimum fluidization velocity with magnetic excitation.

Once the external magnetic field is applied, however, the large agglomerates are gradually broken down into smaller agglomerates that participate in the circulation of the bed. After a few minutes, even at the moderately low gas velocity of 0.94 cm/s, all of the large agglomerates disappear, and the bed expands slowly and uniformly until it reaches the full expansion, (Figure 8.11b), while the pressure drop reading is very close to the weight of the bed, indicating that the entire bed is fluidized.

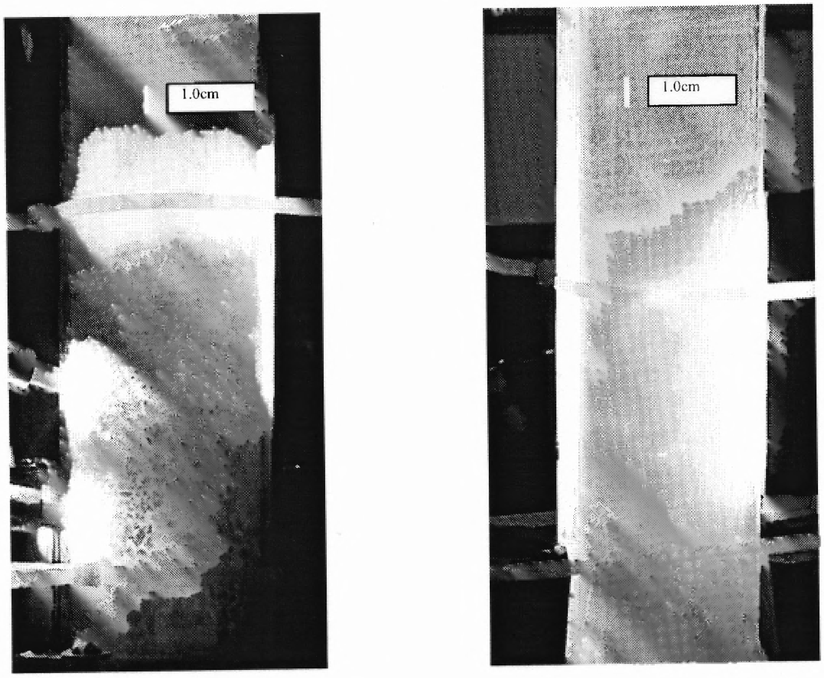

(a) Without magnetic field
Ugas=13.15 cm/s

(b) With magnetic field
Ugas=0.94 cm/s

Figure 8.11 Fluidization of hard agglomerates. (140G, 60Hz, mass of magnets 20.0 g)

The fragmentation caused by the magnetic processing is so obvious that the reduction in size of the hard agglomerates could be seen by inspection after the magnetic field and air flow were shut down. Upon removing the magnetic particles, the nanoparticle agglomerates are recharged back into the chamber and a conventional fluidization experiment (no magnetic assistance) is performed. Figure 8.12 is a comparison of the fluidization characteristics between the powder before and after the magnetic assisted fluidization (fragmentation) process. A very large reduction in the minimum fluidization velocity (U_{mf}) from larger than 13.2 cm/s to 2.29 cm/s indicates that the average agglomerates size has been significantly reduced.

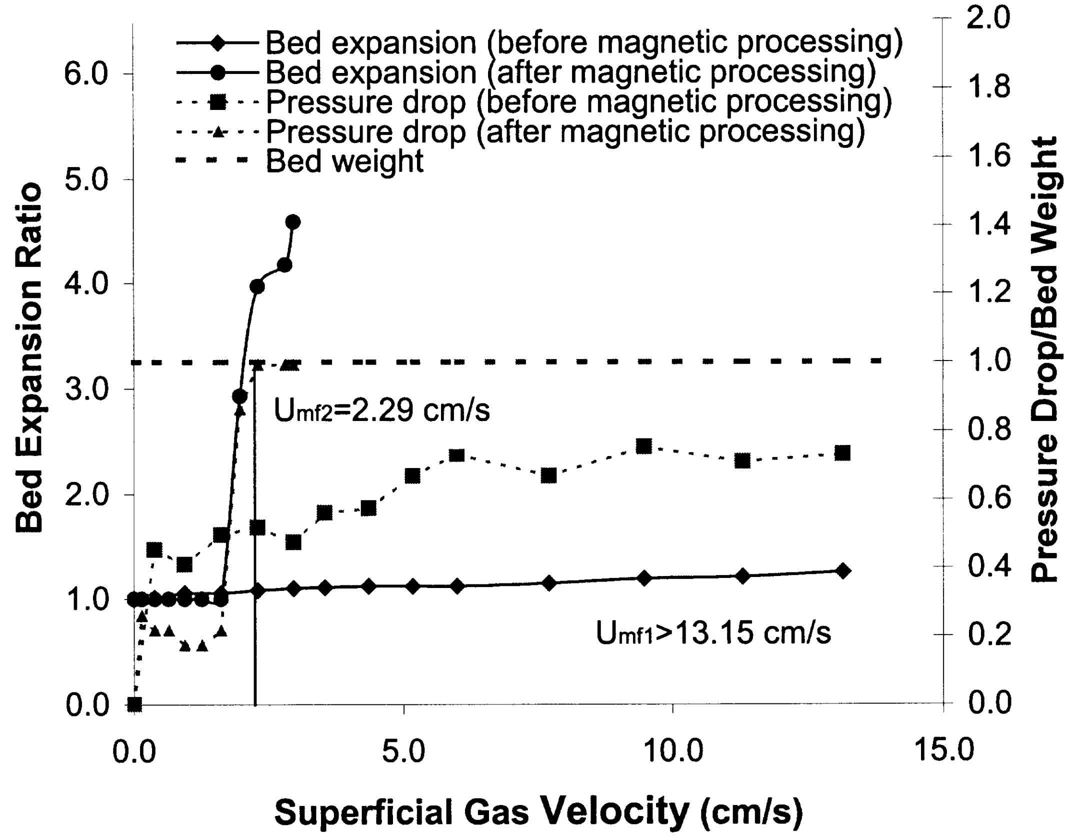

Figure 8.12 Bed expansion ratio and pressure drop for conventional fluidization of hard agglomerates before and after magnetic processing. (Solid lines are the bed expansion ratios, and dashed lines are the pressure drops)
(Magnetic field intensity 140G at the center of the field, mass of magnets 20.0 g, AC frequency 60 Hz)
Umf1: minimum fluidization velocity before magnetic "fragmentation" processing;
Umf2: minimum fluidization velocity after magnetic "fragmentation" processing.

The U_{mf} for the hard agglomerates after magnetic processing is 2.29 cm/s, which is larger than the U_{mf} of 1.25 cm/s for the 80/20 mixture, and also much larger than the

U_{mf} of 0.23 cm/s for the soft agglomerates. This indicates that the average size of the hard agglomerates and of the mixture after the fragmentation process is still larger than that of the soft agglomerates. Hence, in order to better investigate the effect of magnetic excitation (such as mass of magnets used, AC frequencies, and different magnetic field intensity), and to minimize the influence of non-uniformity of the initial agglomerate size distribution, only soft agglomerates were used in the comparative experiments of magnetic fluidization.

At low gas velocities, conventional fluidization (no magnetic assistance) of soft agglomerates or of the 80/20 agglomerate mixture, produces only slugging and channeling, whereas at sufficiently high gas velocities, the bed can be fluidized smoothly. If we continue to increase the gas velocity above a certain level, bubbles can be observed in the fluidized bed. Fluidization of nanoparticle agglomerates occurs due to the disruption of interparticle forces by the large hydrodynamic forces generated at high gas velocities. However, for conventional fluidization of hard agglomerates, even at a very high gas velocity, the bed could not be fully fluidized.

The mechanism of fluidization with the assistance of an oscillating magnetic field is much more complicated. The excited magnets will enhance nanoparticle fluidization at least in two ways: fragmentation of large agglomerates into smaller ones, and transferring kinetic energy generated by the oscillating magnetic excitation to the nanoparticle agglomerates due to collisions to disrupt the large interparticle forces between them. A more comprehensive explanation of this combined effect requires further experimental and modeling efforts.

Table 8.2 Minimum fluidization velocities for soft agglomerates, hard agglomerates and 80/20 mixture. (Degussa Aerosil® R974)

Experimental Conditions	Soft agglomerates Umf (cm/s)	Hard agglomerates Umf (cm/s)	80/20 Mixture Umf (cm/s)
Before processing, conventional fluidization	0.23	>13.2	5.67
During magnetic processing, magnetic assisted fluidization	0.26	0.38	0.14
After magnetic processing, conventional fluidization	0.23	2.29	1.25

Table 8.2 presents a summary of the minimum fluidization velocities for the soft, hard, and the 80/20 agglomerate mixture. For the soft agglomerates magnetic excitation has little effect, but it produces a definite improvement in fluidization behavior for the 80/20 mixture. For the hard agglomerates, magnetic excitation changes the fluidization characteristics significantly, from no fluidization to smooth, bubbleless, agglomerate particulate fluidization (APF) with very large bed expansion up to 5 times of the initial bed height. The minimum fluidization velocity is also significantly reduced from higher than 13.2 cm/s to 0.38 cm/s. Without magnetic excitation, at a gas velocity of 13.2 cm/s or higher, extremely strong elutriation is observed, whereas with magnetic excitation, at the low gas velocity of 0.38cm/s, elutriation was hardly noticed.

8.2.2.2 ABF Nanoparticles

For some types of ABF nanoparticles (Cabot Carbon Black ® PEARLS 2000), the reduction in the minimum fluidization velocity is also impressive. From Figure 8.13, it can be seen that the minimum fluidization velocity U_{mf2} significantly decreased with the magnetic excitation, and the bed expansion increased very much. Without magnetic excitation, the minimum fluidization velocity U_{mf1} is 27.6 cm/s, and this high gas velocity leads to large elutriation and large gas bypassing. When magnetic excitation is applied, the minimum fluidization velocity U_{mf2} drops to 1.93 cm/s, and this low gas velocity prevents elutriation and significantly reduces gas bypass. And at the same time, the bed expansion increased from around 60% to even 5 or 6 times of the original bed height. The application of magnetic excitation, which leads to low gas velocity, reduced gas bypass and large bed expansion is very beneficial for improved heat and mass transfer, chemical reaction and combustion.

It should be pointed out that to initiate the circulation of powder in the bed with the assistance of magnetic excitation, a gas velocity which is higher than Umf2 is required, for example, for example, a U_{gas}=5.0 cm/s is required to initiate the circulation of the whole bed, and then the magnetic excitation can begin to fragmentize the large agglomerates into smaller ones.

Another interesting observation is that after magnetic processing, besides the significant reduction of agglomerate size, the bulk density of powder is also significantly reduced. For example, the initial bed height was 12.0 cm, and the initial bulk density was 215 kg/m^3 before magnetic assisted fluidization; but after the magnetic fluidization experiments, and after shutting off the gas, the bed height is 32.0 cm, almost 3 times larger than the initial bed height, and the bulk density of the powder reduced to 73.1 kg/m^3.

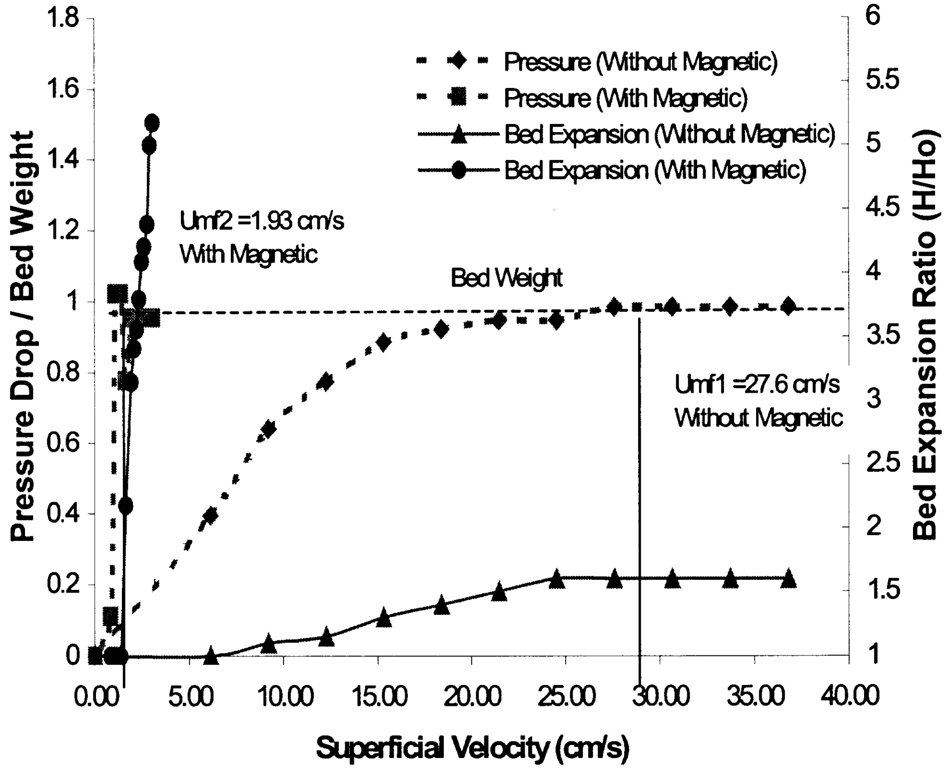

Figure 8.13 Fluidization curve for Carbon Black (Cabot ® PEARLS 2000) with and without magnetic excitation. Bulk density = 215 kg/m^3, Primary nanoparticle size 12 nm. Initial bed height = 12.0 cm, mass of particle = 60.0 grams, bed weight = 0.90 inches water column. Without magnetic excitation, U_{mf1}=27.6 cm/s; with magnetic excitation, U_{mf2}=1.93 cm/s. Intensity of magnetic field ~ 200 Gauss, mass of magnetic particles 30.0 grams, 60 Hz AC.

Figure 8.14 is a comparison of conventional fluidization of carbon black powder before and after magnetic process. Compared with U_{mf1} (27.6 cm/s) before magnetic processing, U_{mf2} (3.86 cm/s) after the magnetic processing is significantly decreased, and the bed expansion increased very much.

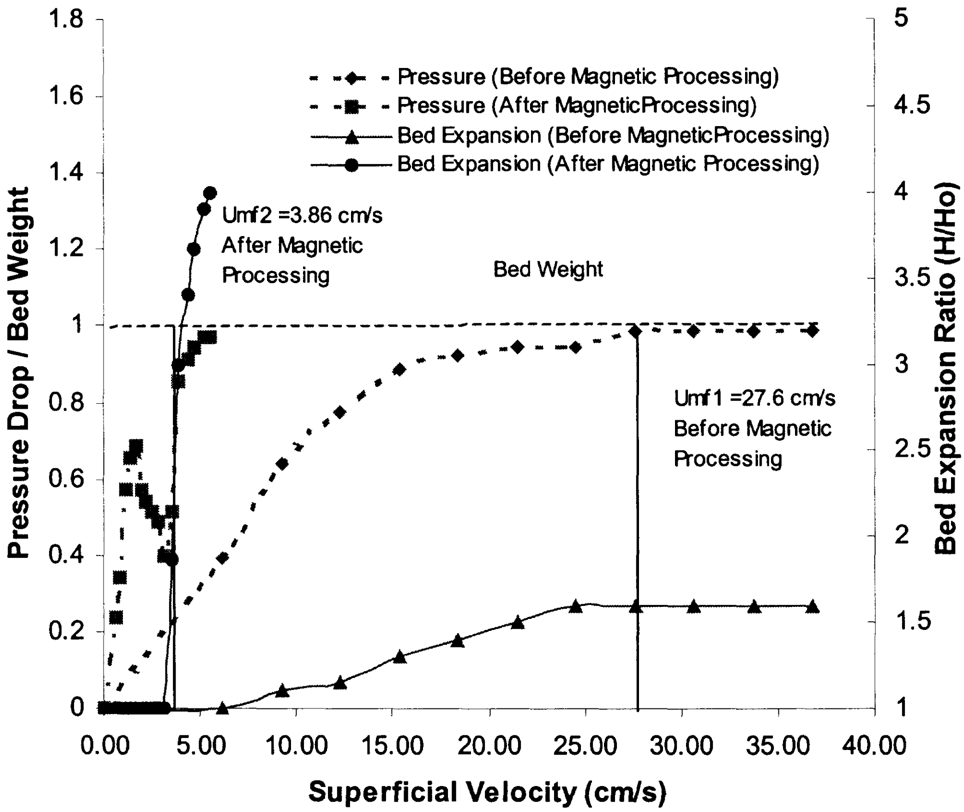

Figure 8.14 Fluidization curve for Carbon Black (Cabot ® PEARLS 2000) before and after magnetic processing. Fresh powder bulk density = 215 kg/m^3, Primary nanoparticle size 12 nm. After magnetic processing, bulk density = 73.0 kg/m^3
Before magnetic processing, U_{mf1}=27.6 cm/s; after magnetic processing, U_{mf2}=3.86 cm/s.

Table 8.3 presents a summary of the minimum fluidization velocities and bed expansions for the carbon black (Cabot ® PEARLS 2000) nanoparticle agglomerates. The substantial reduction in the minimum fluidization velocity as well as the realization of smooth and bubbleless fluidization with little elutriation is clearly beneficial to many industrial applications where a good mixing and high rates of heat and mass transfer with little gas bypassing are required.

Table 8.3 Minimum fluidization velocity and bed expansion of Carbon Black (Cabot ® PEARLS 2000) nanoparticle agglomerates before, during and after magnetic assisted fluidization.

Experimental Conditions	Umf (cm/s)	Bed Expansion Ratio at Umf (H/Ho)	Bed Expansion Ratio at 1.5Umf (H/Ho)
Before processing, conventional fluidization, fresh powder	27.6	1.60	1.60
During magnetic processing, magnetic assisted fluidization	1.93	3.15	5.17
After magnetic processing (magnets removed from the processed nano-powder), conventional fluidization	3.86	2.77	4.0

8.2.3 Agglomerates Size Measurement

8.2.3.1 In-situ Agglomerates Size Measurement of APF Nanoparticles

Figure 8.15 shows typical images of the agglomerates on the fluidized bed surface and Figure 8.16 shows the agglomerate size distributions, with and without magnetic assistance. Some statistical results are given in Table 8.4, which illustrates that the mean size of R974 agglomerates is decreased from 315μm to 196μm by the magnetic processing. Following the methodology developed by our group in the previous chapter 4, the mean agglomerate size can also be calculated based on experimental measurements of bed expansion and superficial gas velocity for both cases, with and without magnetic excitation. These calculated results, also listed in Table 8.4, show that the mean size of silica R974 nanoparticle agglomerates is changed from 211μm to 95μm after the magnetic processing. Both methods indicate that the mean agglomerate size decreases by roughly 100 μm during the magnetic processing.

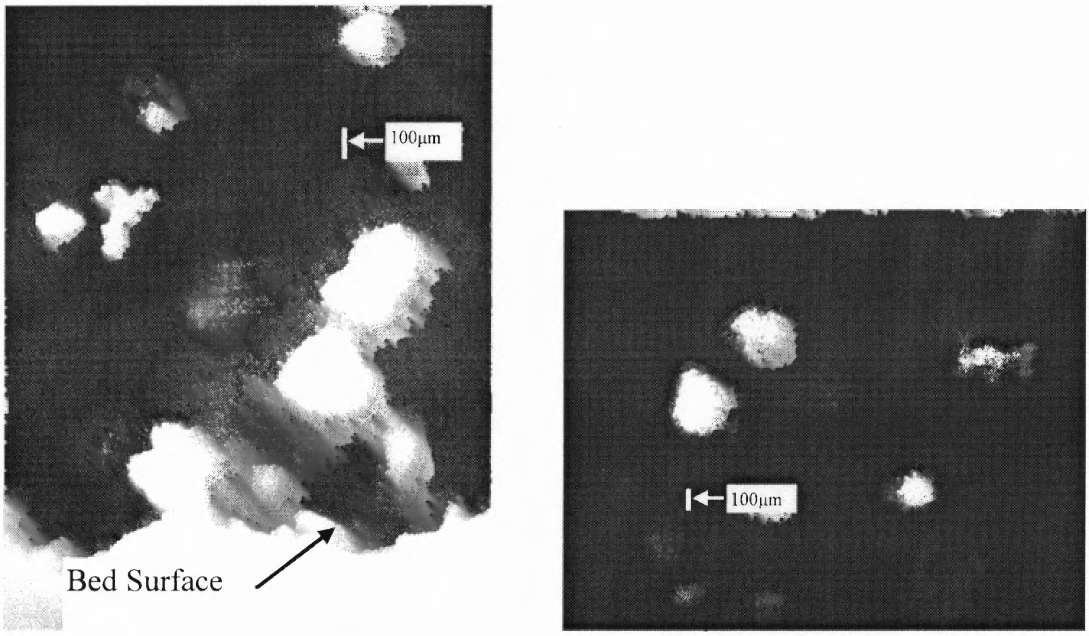

(a) Without magnetic field (b) With magnetic field, 140G, 60Hz, mass of magnets 20.0 g

Figure 8.15 Photographic images of agglomerates near the fluidized bed surface at Ugas=0.5 cm/s. (Degussa Aerosil® R974, Soft agglomerates)

(a) Without magnetic field.

(b) With magnetic field, 140G, 60Hz, mass of magnets 20.0 g.

Table 8.4 Comparison of agglomerate sizes from optical experimental measurements and calculation results using the prediction methodology developed in Chapter 4.

Magnetic excitation	Measured agglomerate mean size (μm)	Number of samples	Standard deviation (μm)	Calculated results
No	315	193	123	211
Yes	196	172	64.9	95

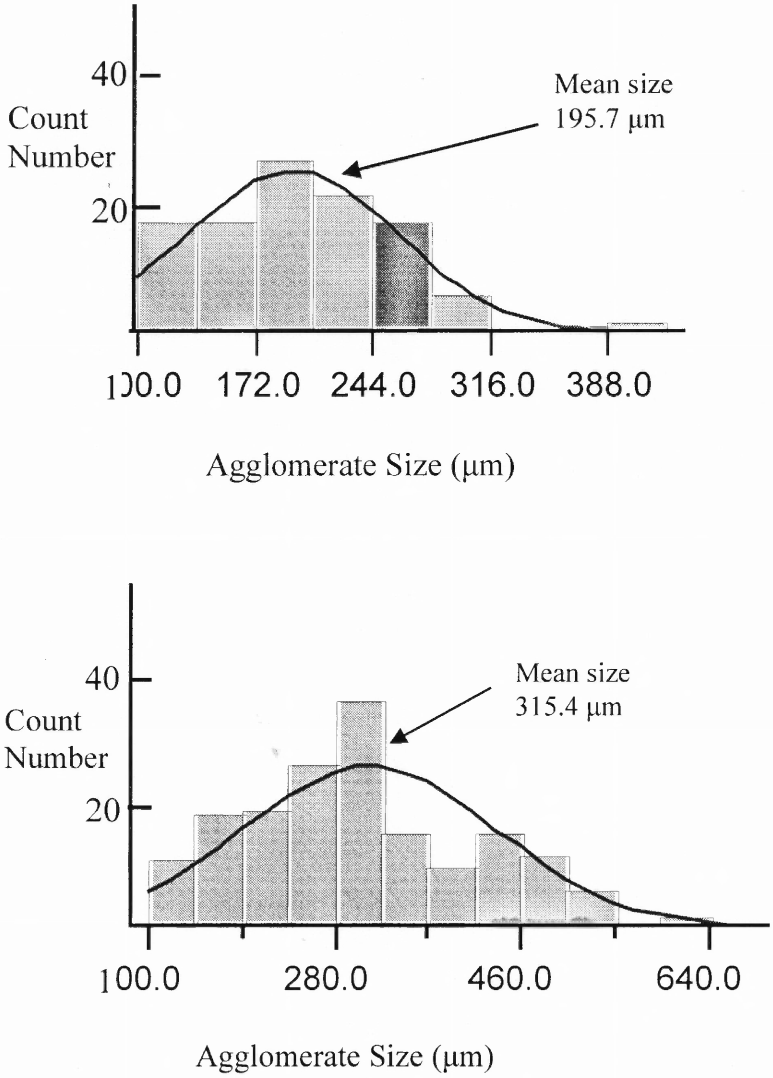

Figure 8.16 Typical agglomerate size distribution.
(In-situ optical measurements on the fluidized bed surface, Degussa Aerosil® R974, soft agglomerates)

8.2.3.2 Agglomerates Size Measurement of ABF Nanoparticles

The carbon black powder can absorb the laser light, hence the above in-situ agglomerate size measurement approach could not be used to measure the size of fluidizing carbon black powder. In this study, size measurement is conducted by the following method: carbon black powder is sieved using 10 sieves with different mesh numbers, the mass within each range is recorded, and the results are processed statistically and listed in Table 8.5

Table 8.5 Size distribution by mass for Carbon Black (Cabot ® PEARLS 2000) nanoparticle agglomerates before, 1 hour after and 7 days after magnetic assisted fluidization.

Size of Agglomerate (μm)	Mass of particles (gram) Before Magnetic Fluidization	Mass Percentage (%) Before Magnetic Fluidization	Mass of particles (gram) 1 hours After Magnetic Process	Mass Percentage (%) 1 hour After Magnetic Process	Mass of particles (gram) 7 days After Magnetic Process	Mass Percentage (%) 7 days After Magnetic Process
<150	1.55	5.17	19.83	40.7	2.47	15.17
150-250	1.5	5	28.72	59.0	13.40	82.31
250-425	2.16	7.2	0.12	0.25	0.41	2.52
425-500	1.3	4.33	0	0	0	0
500-710	4.86	16.2	0	0	0	0
710-850	4.15	13.8	0	0	0	0
850-1000	4.42	14.7	0	0	0	0
1000-1400	9.37	31.2	0	0	0	0
1400-1700	0.38	1.27	0	0	0	0
> 1700	0.03	0.1	0	0	0	0
Estimated Mean Size (μm)	**798.3 μm**		**159.6 μm**		**188.3 μm**	

From Table 8.5, it is clear that magnetic processing significantly reduced the agglomerate size from around 800 μm to less than 200 μm, and this is the key reason why magnetic excitation can significantly reduce the minimum fluidization velocity.

Comparing with the results 1 hour after the magnetic processing (in the fluidized bed), and after storing the powder for 7 days, minor re-agglomeration may have occurred, but there is no appreciable difference between the average agglomerate sizes (around 160 μm vs. around 190 μm).

Table 8.6 shows the calculated results using the prediction methodology in Part I; the model prediction agrees fairly well with the measured results.

Table 8.6 Comparison of agglomerate sizes from experimental measurements and calculation results using the prediction methodology developed in Chapter 4.

Condition	Measured agglomerate mean size (μm)	Calculated results (μm)
Before Magnetic Fluidization	798.3	---
During Magnetic Fluidization	159.6	124.2
After Magnetic Processing	188.3	158.5

8.2.4 Bed Expansion and Bed Collapse as a Function of Time

From experimental observation, once the magnetic excitation is turned on, the fluidization behavior of the nanoparticle bed does not change immediately, and it will take a couple of minutes for the bed expansion to begin and full expansion takes another few minutes.

The bed expansion as a function of time for R974 silica at different gas velocities is shown in Figure 8.17a; the higher the velocity the quicker the bed expansion. Similarly, when the magnetic excitation is turned off, it also takes a very short period of time, typically a few seconds, for the bed to begin to collapse, and the collapse will last a few minutes before reverting back to a fixed bed with an uneven surface. The bed collapse as a function of time is shown in Figure 8.17b; the higher the gas velocity, the longer it will take for the bed to collapse.

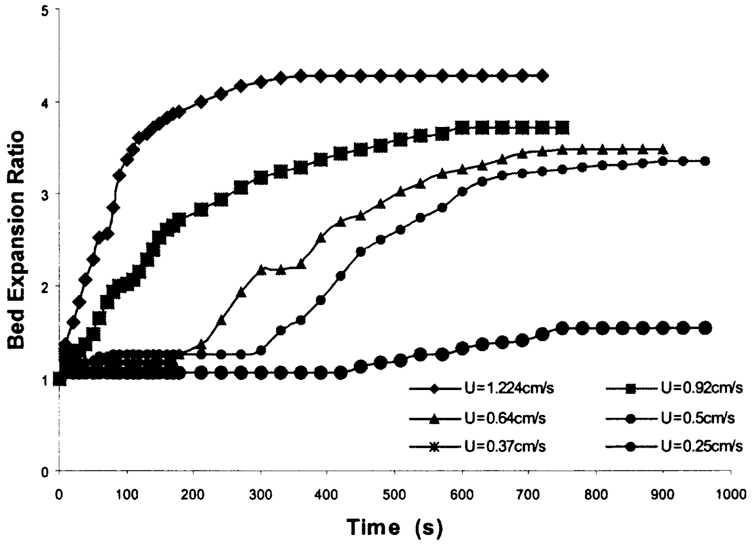

(a) Bed expansion.

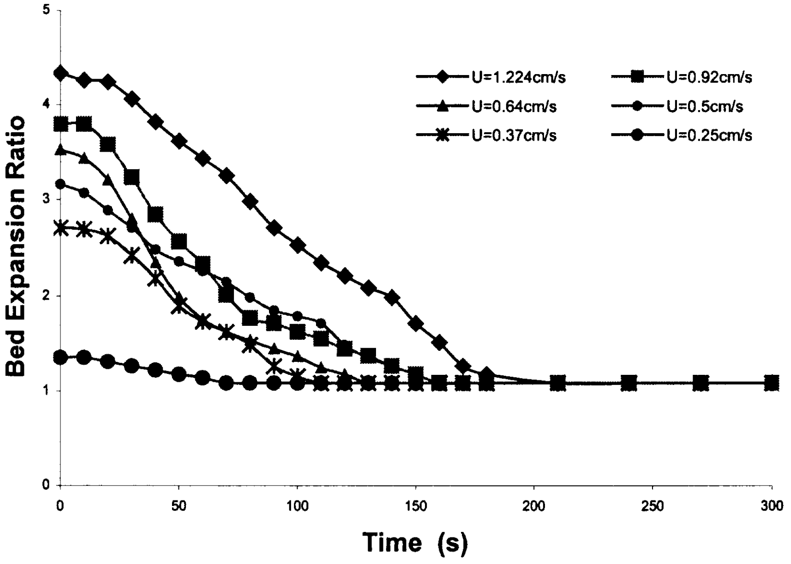

(b) Bed collapse.

Figure 8.17 Bed expansion and bed collapse as a function of time for soft agglomerates with magnetic excitation.

(Magnetic field intensity 140G at the center of the field, mass of magnets20.0 g, AC frequency 60 Hz.)

8.2.5 Effects of the Mass of Magnets Used

Fluidization experiments with magnetic assistance were conducted using the soft agglomerates at four different masses of magnets, varying from 2.5 grams to 20.0 grams. Table 8.7 presents the values of U_{mf} and the bed expansion ratios at two different gas superficial velocities that were observed for these four cases. The table shows that the minimum fluidization velocity and bed expansion depends on the magnet mass, with U_{mf} decreasing from 1.61 cm/s to 0.26 cm/s as the mass increases from 2.5 grams to 20.0 grams. This indicates that adding more magnetic particles to the bed will result in more kinetic energy transported from the magnets to the nanoagglomerates, causing more fragmentation and better fluidization. The table also shows that there is little benefit in increasing the mass of magnets above 10.0 grams. It should also be noted that the minimum fluidization velocities for a low mass of magnets are actually higher than what we obtained for the nanoagglomerates without any magnetic assistance. This is probably due to the additional drag of the gas on the magnetic particles or due to the increased non-uniformity of the bed particles with the addition of magnetic particles.

Table 8.7 Minimum fluidization velocities and bed expansion ratios for soft agglomerates with different mass amount of magnets. (Magnetic field intensity 140G at the center of the field, AC frequency 60 Hz.)

Mass of magnets (grams)	Umf (cm/s)	Bed expansion ratios at Ugas = 1.26 cm/s	Bed expansion ratios at Ugas = 1.96 cm/s
2.5	1.61	1.35	3.82
5.0	0.51	3.57	4.43
10.0	0.26	3.35	4.09
20.0	0.26	3.91	4.91

8.2.6 Effects of Intensity of the Oscillating Magnetic Field

Table 8.8 presents the values of U_{mf} and bed expansion ratio at a fixed superficial gas velocity and a fixed amount of magnets for three different magnetic field intensities. As mentioned earlier, the center point of the column around which the 2 coils are located is used as the reference point for the magnetic field intensity. It was observed that, with a magnetic field intensity of less than 80G, the bed could not be fluidized. Hence, in order to conduct the magnetic fluidization experiments, three different intensities are selected as 100, 120, and 140G. Table 8.5 shows that the minimum fluidization velocity is a strong function of the magnetic field intensity and U_{mf} decreases rapidly as the magnetic field intensity increases, indicating improved fluidization. Although the beds expand more in a stronger magnetic field, as expected, the expansion ratios are quite close to one another, indicating a weak dependence upon the magnetic field intensity.

Table 8.8 Minimum fluidization velocities and bed expansion ratios for soft agglomerates with different intensities of magnetic field. (Mass of magnets 20.0 g, AC frequency 60 Hz.)

Intensity of Magnetic field (Gauss)	Umf (cm/s)	Bed expansion ratios at Ugas = 2.29 cm/s
100	2.29	5.13
120	0.51	5.30
140	0.26	5.52

8.2.7 Effects of Frequency of the Oscillating Magnetic Field

Table 8.9 presents the values of U_{mf} and bed expansion ratio at a fixed superficial gas velocity for three different frequencies of AC power, keeping the mass of magnets at 20.0 g and the magnetic field intensity at 120G. The table shows that the frequency of the magnetic field can significantly affect the minimum fluidization velocity. At the lower frequencies, 45 Hz and 60 Hz, the beds show a similar fluidization behavior, and can be fluidized easily at a U_{mf} of 0.65 cm/s and 0.51 cm/s, respectively. But at higher frequency, 80 Hz, the bed is difficult to fluidize, U_{mf} is as high as 2.64 cm/s, and the bed expansion is much smaller than that at the lower frequencies. At a frequency higher than 90 Hz, the bed could not be fluidized at all.

Table 8.9 Minimum fluidization velocities and bed expansion ratios for soft agglomerates with magnetic assistance at different frequencies. (Mass of magnets 20.0 g, magnetic field intensity 120 G at the center of the field.)

Frequency of Magnetic field (Hz)	Umf (cm/s)	Bed expansion ratios at Ugas = 2.29 cm/s
45	0.65	5.26
60	0.51	5.30
80	2.64	2.17 (Ugas=2.64 cm/s)

8.2.8 Concluding Remarks

8.2.8.1 APF Nanoparticles

For silica nanopowder (Degussa Aerosil® R974), we observed that the "soft" fraction (after sieving) could be fluidized at low velocity in contrast to the "hard" fraction, which could not be fluidized at all. However with magnetic assistance, fluidization of the "hard" fraction is achieved due to the fragmentation of the large agglomerates at the bottom of the fixed bed.

Fluidization of the hard agglomerates occurs due to gas channeling and interaction with smaller free agglomerates formed near the bed bottom caused by the impacts of the magnetic particles. When the free aggregates reach the channel entrance they move upward together with the gas flow, reach the channel exit, rise above it, and spread over the top of the bed top in the radial direction. This leads to the formation of a new (upper) fluidized bed of smaller agglomerates on the top of the existing fixed bed. The transport of the free aggregates to the channel entrance at the bottom of the fixed bed results in the settling of the fixed bed because the free aggregates that moved to the top of the bed are replaced by an equal amount of the larger agglomerates. This process continues until the fixed bed gradually disappears and the entire bed is fluidized.

This study has shown that silica nanoparticle agglomerates can be easily and smoothly fluidized with the assistance of magnetic particles in an oscillating magnetic field. Due to a significant reduction in the minimum fluidization velocity with magnetic assistance, both elutriation of nanoparticle agglomerates and gas bypass in the form of bubbles is greatly reduced. With magnetic excitation, hard (larger than 500 μm) agglomerates change their fluidization pattern from no fluidization to agglomerate particulate fluidization (APF) with large bed expansion. The minimum fluidization velocity of an 80% soft (smaller than 500 μm) and 20% hard agglomerate (80/20) mixture can also be significantly reduced, resulting in easier and more uniform fluidization.

From in-situ agglomerate size measurements on the surface of the fluidized bed and calculations using a predictive model based on experimental data, it is found that magnetic excitation will result in fragmentation of the agglomerates, so that the mean agglomerate size is significantly reduced. The ability to fluidize these fumed silica nanoparticle agglomerates depends on the mass of magnets, the intensity of the magnetic field, and the frequency of the magnetic field.

8.2.8.2 ABF Nanoparticles

For ABF nanoparticles (carbon black: Cabot ® PEARLS 2000), there is also significant improvement in fluidization quality by introducing magnetic excitation. Without the assistance of magnetic excitation, bubbling, gas bypassing and substantial elutriation of particles exists, bed expansion is only around 60%, the fluidization has to be stopped due to the huge loss of particles (10% loss within minutes), and the particle shows a typical ABF fluidization with a very large minimum fluidization velocity of 27.6 cm/s and strong gas bypassing.

The magnetic excitation can significantly improve the quality of fluidization, with the assistance of magnetic excitation, within several minutes, the bed begin to expand up to 5 or more times at low gas velocity, an extremely smooth uniform fluidization can be achieved, and bubbling disappeared, no elutriation can be observed, the nanoparticle shows a typical APF fluidization with a much reduced minimum fluidization velocity of only 1.93 cm/s.

The average agglomerate size of original carbon black powder is around 800 μm, while the original large agglomerates were fragmentized into much smaller agglomerates with the assistance of magnetic excitation, and the average agglomerate size significantly reduced to around 160 μm. After magnetic assisted fluidization, the powder were stored in a sealed container for 7 days, then a conventional fluidization with this powder was conducted, a uniform APF fluidization can be achieved with ignorable elutriation and large bed expansion with minimum fluidization velocity as 3.86cm/s. Model agrees well with experimental measurements.

8.2.9 Limitation of this Study and Future Research Directions

This study conducted experimental studies on external oscillating magnetic excitation with in-bed magnets on the fluidization of a limited choice of nanoparticle agglomerates. Experimental studies on many more different types of nanoparticles, as well as theoretical mechanistic studies are recommended. Numerical simulations would also be useful in better understanding the effect of external magnetic excitation with in-bed magnets on the fluidization of nanoparticle agglomerates.

PART III: FILTRATION OF SUBMICRON PARTICLES USING NANOPARTICLE AGGLOMERATES

This part will focus on the experimental study on nanoparticle agglomerates as a filter media for filtration of submicron particles in gas stream. Chapter 9 summarizes the existing literature, Chapter 10 describes the experimental system, and the results and discussion are given in Chapter 11.

CHAPTER 9

LITERATURE REVIEW

9.1 Fibrous and Granular Bed Filtration

The theory of filtration by fibrous HEPA (High Efficiency Particulate Air) filters and granular bed filters has been well developed by considering the hydrodynamic flow patterns around a cylinder (or sphere) lying transverse to the flow (Flagen and Seinfeld, 1988;Tien, 1989). As the gas streamlines bend around the collector, very small particles with low inertia follow the streamlines, but larger, heavier particles follow a more direct path and will collide with the collector. The higher the gas velocity and more massive the particle, the greater the likelihood of it striking the cylinder (inertial impaction mechanism). However, a particle of radius r_p, need only approach the collector to that distance to touch (direct interception mechanism) and when there are two particles of the same mass traveling on the same streamline, the one with the larger radius is more likely to impinge on the collector. All particles also undergo Brownian motion (diffusion mechanism) to cause them to deviate significantly from the gas streamlines. The magnitude of the deviation increases as the particle size and velocity decrease. These three classical mechanisms, inertial impaction, direct interception and diffusion are the major factors in particle capture (El-Halwagi, 1990; Coury *et al.*, 1987). A fourth mechanism, gravity settling is not considered important in HEPA filters used to remove submicron particles. Of course, electric charges if present on either the particles or fibers, or both, will also affect the collection efficiency or penetration (Tardos *et al.*, 1979).

Since diffusion capture increases as the particle size decreases and inertial impaction comes into play only as the particle size increases, it follows that there should be a particle size which penetrates most easily through fibrous (and granular) filters. Submicron size solid and liquid particles (0.1 to 1 μm) which are the most difficult to filter, are commonly known as the most penetrating particle size (MPPS). . As the velocity through the filter is increased and diffusion becomes less important, penetration rises to a maximum and then decreases as inertial effects appear. The penetration due to direct interception does not depend on velocity. Figure 9.1 is a schematic diagram showing how penetration varies with velocity and other important filter parameters. If the penetration is plotted against particle size then the position of the penetration maximum clearly depends on velocity, shifting to larger particle size as the velocity decreases.

It is assumed that particles are captured by London van der Waals forces or some other forces on touching a fiber, which is reasonable at the low velocities associated with HEPA filters where diffusion is the main mechanism of capture. However, at higher velocities particles do not always adhere and larger particles may possess sufficient kinetic energy to bounce off the fibers (D'Ottavio and Goren, 1983). Also, when the filter becomes heavily loaded, aggregates of collected particles are often dislodged as aerodynamic forces overcome adhesive forces and the filtration efficiency will drop rapidly.

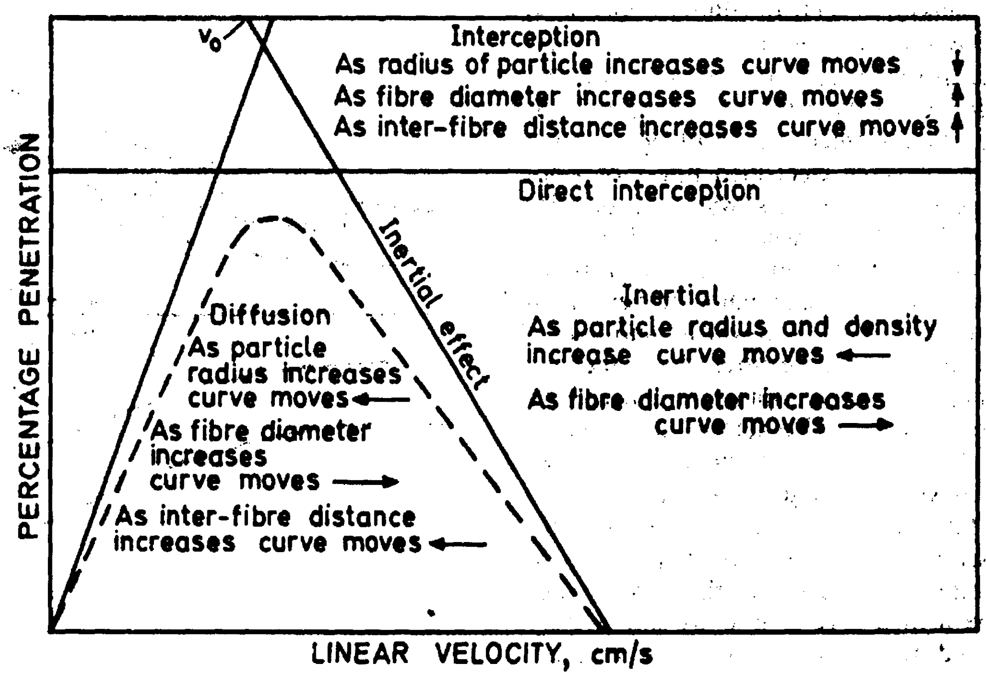

Figure 9.1 Penetration as a function of velocity showing MPPS.

The efficiency of particle removal across fibrous filters in the absence of electrical effects is generally assumed to be a combination of the three removal mechanisms operating concurrently, i.e., diffusion, interception and impaction. It is generally assumed that the collection efficiencies due to individual mechanisms are additive, so that the total collection efficiency of a single fiber (called the single particle efficiency), $\eta=\Sigma\eta_i$. The filter media penetration is then given by (Thomas et al, 1999)

$$P = (1-E) = \exp[-4\eta\alpha L/\pi(1-\alpha)d] \tag{9.1}$$

where α is the filter packing density (1-ε), L is the filter thickness, and d is the fiber diameter.

Currently, HEPA filters are used extensively in the microelectronics (clean rooms) and pharmaceutical industries, and are also used in hospitals, and in food and cosmetic production facilities, and even in the home in air purifiers and vacuum cleaners, for the purpose of filtration of MPPS particulates. In all of these applications the objective is either to prevent contamination of a particularly sensitive product with particulate pollutants or to protect human beings from dangerous particulates such as microorganisms (bacteria, viruses and mold), pollen, asbestos, etc. HEPA fiber-based filters are made up of an entanglement of thin, usually less than one micron in diameter, fibers in which particles are collected by several classical mechanisms such as diffusion, interception and inertial impaction.

The two major important characteristics of these filters, the pressure drop and the collection efficiency, E (or the penetration, P=1-E), depend on the filter structure (packing density, fiber diameter), operating conditions (filter velocity, temperature) and the properties of the aerosols to be filtered (density, mean particle size, particle size distribution, solid or liquid). In addition they depend strongly on the filter loading. SEM studies (Penicot et al, 1999) of the loading of HEPA fiber filters with solid particles show that the filtration initially takes place in the depth of the filter with the formation of chainlike agglomerates called dendrites not unlike the chains of nanoparticles shown in Figure 9.2, but 3 orders of magnitude larger in size. During this process the pressure drop rises linearly with the amount of mass collected at constant face velocity. However, as the dendrites begin to fill the spaces between the fibers of the filter, a filter cake of increasing thickness begins to form at the upstream surface of the filter and the slope of the pressure drop with increasing loading rises sharply, indicating that the filter is being clogged. This occurs at a loading (mass of particulates collected) of the order of 1 g/m^2 of filter area (Penicot et al, 1999).

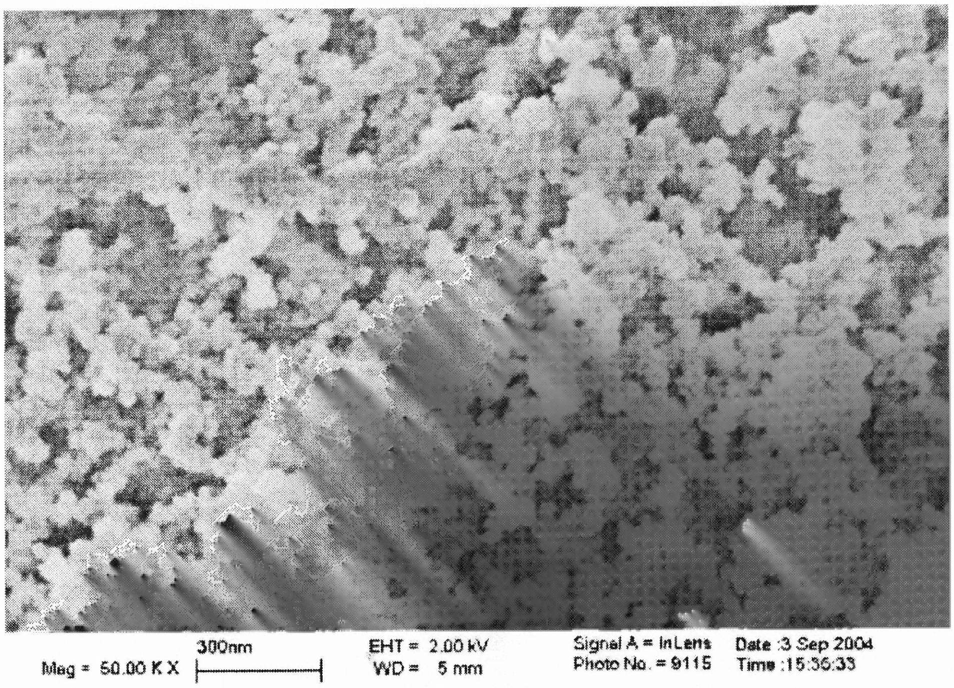

Figure 9.2 SEM image showing individual silica nanosize particles sintered together in a chain-like structure. Scale bar = 300nm. (Degussa Aerosil® A300).

For liquid particles (mists), in the early stage of filtration, the particles are deposited as droplets around the fibers and the pressure drop rises slowly with mass collected per unit of filter area. However, at a certain point during the filtration, a sharp exponential rise in pressure drop is observed. This is attributed to the presence of a liquid film covering the filter surface. It is assumed that the droplets deposited on the filters progressively grow and join together to form bridges at the intersection of several fibers. At the point of clogging, all the interstices of the first layer of fibers are filled in, forming a film covering the filter surface (Penicot et al, 1999).

When clean, HEPA fiber-based filters provide excellent filtration efficiency and low pressure drop for both solid and liquid MPPS and filtration occurs throughout the depth (deep bed filtration) of the filter. However, as soon as the upstream surface becomes heavily clogged with particulates, filtration only occurs at the fiber surface (cake filtration) leading to a sharp rise in pressure drop and the filter needs to be replaced.

9.2 Unique Properties of Nanoparticle Agglomerates as Ideal Filter Media for MPPS

During the above research on the fluidization of nanoparticles, it is observed that nanoparticles could be fluidized in the form of large (~100-400 μm) stable agglomerates that are extremely porous (ε~0.99). These nanoagglomerates are hierarchical fractal structures consisting of sub-agglomerates or aggregates at a number of different length scales, down to individual nanosize particles as shown in the SEM image in Figure 9.2, and the schematic drawing in Figure 4.2.

In-situ photographs taken at the surface of a fluidized bed of Degussa Aerosil® A300 silica nanoagglomerates (primary particle size ~ 7 nm), for example, and shown in Figure 9.3, gave a mean agglomerate size of about 200 μm based on image analysis of over 200 images. The mathematical model based on the Richardson-Zaki equation for particulate fluidization to predict the mean agglomerate size, which is included in Chapter 4, also gave results in good agreement with the in-situ experimental measurements.

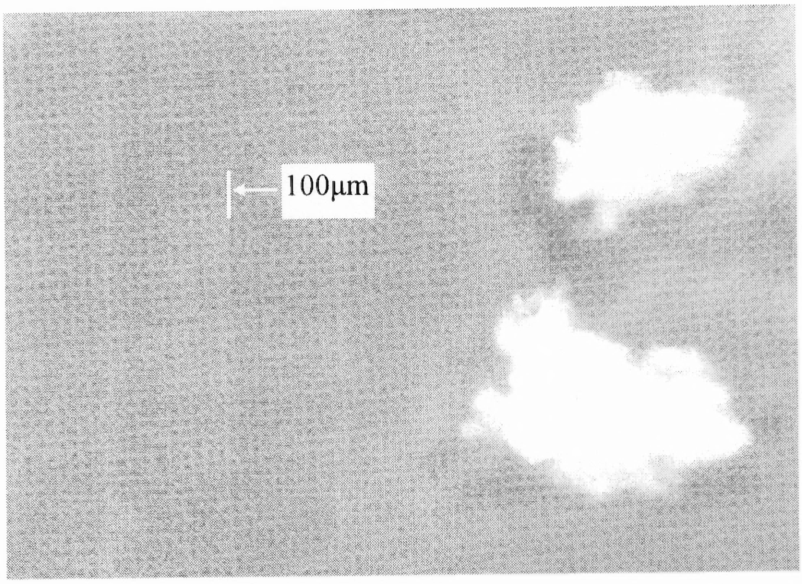

Figure 9.3 Laser and CCD camera results capturing agglomerates in a conventional fluidized bed. Scale bar = 100μm. (Degussa Aerosil® A300).

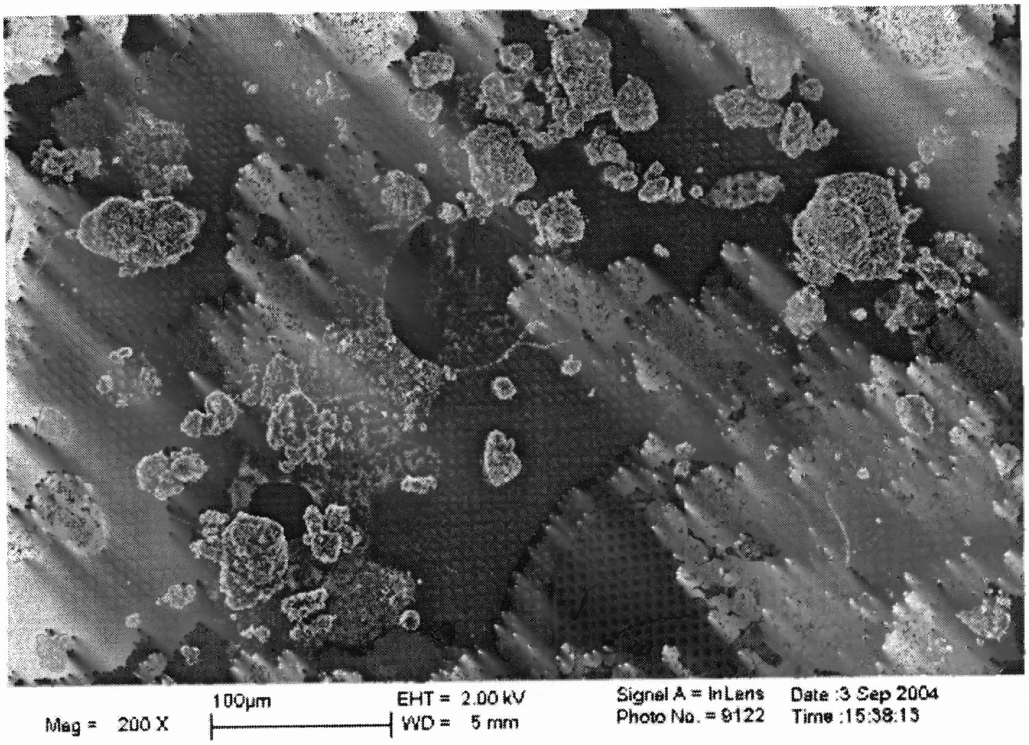

Figure 9.4 SEM images of samples, (Degussa Aerosil® A300). Scale bar = 100μm.

Yet, when the agglomerates were removed from the fluidized bed and studied under a SEM as seen in Figure 9.4, they appear to be of mean size of about 30 μm, an order of magnitude smaller than that observed from the in-situ photographs. It is suspected that the large nanoagglomerates are extremely fragile, and removing them from the fluidized bed and preparing them for SEM analysis fragmented them into what we call sub-agglomerates (SA). A high magnification of single sub-agglomerate, clearly showing its porous structure, is shown in Figure 9.5.

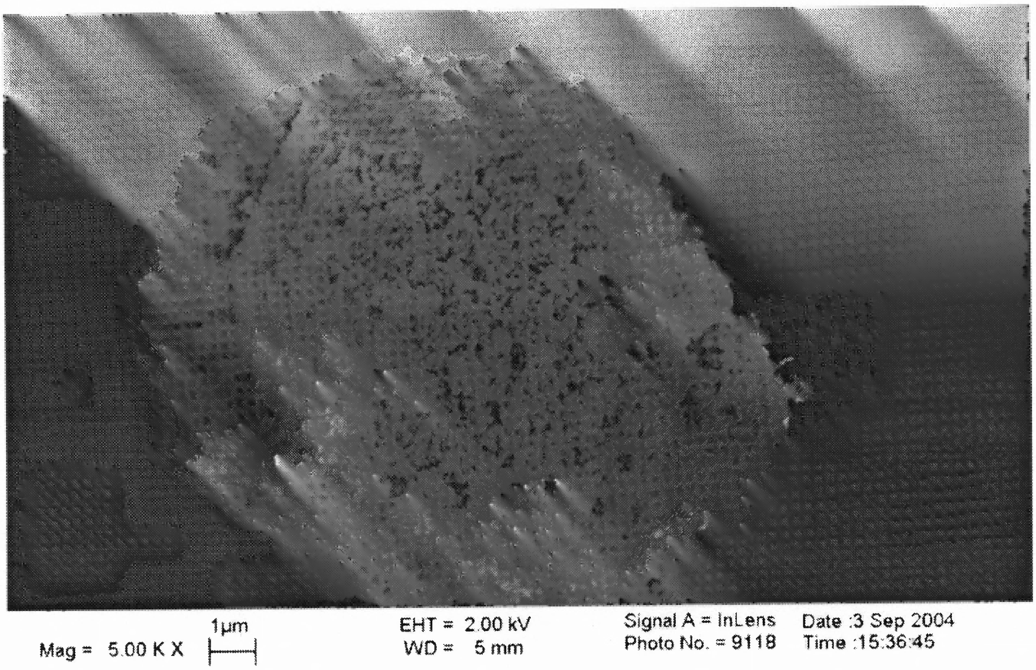

Figure 9.5 High magnification of a single sub-agglomerate (SA) showing the highly porous structure. (Degussa Aerosil® A300). Scale bar = 1μm.

Based on the experimental particle characterizations (Figures 9.2-9.5), and what we perceive to be the structure of the nanoagglomerates (Figure 4.2), they should behave as an ideal filter media to remove particles (solid and liquid) from industrial gas streams, especially the MPPS particles.

The nanoagglomerates are relatively large in size, which would result in a low gas pressure drop; they are extremely porous with an overall internal porosity greater than 0.99 which suggests that some of the "dusty" gas would flow through them; and if used for filtering liquid particles (mists) that wet their surface, they would act as a sponge and suck in the liquid drops by capillary action.

Best of all, because of the relatively large distance between adjacent nanoagglomerates (high external porosity), they should act as a deep bed filter (unlike fiber-based HEPA filters) without surface cake formation, which invariably causes HEPA filters to clog rather quickly. Based on these favorable properties and structure, it is anticipate that the nanoagglomerates will perform as well (high collection efficiency) as fiber-based HEPA filters, but with a much higher dust loading capacity. In this study, a set of experiments using fractal Degussa Aerosil® A300 nanoaprticle agglomerates are performed to test the filtration of submiron solid particles and liquid droplets generated by a bunch of burning incenses.

This study is an exploratory experimental study on filtration of sub-micron particles using nanoparticle agglomerates as the filter media; all of the tests in this study are qualitative rather than quantitative. The major objective is to do a proof of concept and provide a research direction for future quantitative and much more comprehensive studies.

CHAPTER 10

EXPERIMENTAL SETUP

A number of simple experiments were performed to test the idea of using nanoagglomerates as a filter media for HEPA filters. Hydrophilic silica nanoagglomerates (Degussa Aerosil® A300) with a primary particle size of 7 nm, a bulk density 39 kg/m^3 and a BET surface area of 300 m^2/gram are used in the experiments. The nanoparticles were first sieved by a 500μm sieve and then, either charged directly or fluidized (U_{air} =2.0 cm/s) in a 2-inch tube for 30 minutes, before being charged into the filter assembly shown in Figure 10.1 and Figure 10.2. Two filters of different thickness were constructed. The first filter consisted of two layers of fine steel screens (40-50μm opening), which were glued onto two rubber washers having an inner diameter of 1 inch. Nanoagglomerates were poured into the space between the washers (on the screens) forming a packed bed. PVC flanges were placed on each of the rubber washers, and the assembly was tightened by nuts and bolts. The thickness of the filter is ~5mm and the amount of nanoparticles charged is ~0.074 g. The second filter was made using five layers of washers instead of two, which increased the thickness to ~16mm and the amount of nanoparticles to ~0.15 g; all of the other experimental conditions were kept the same.

As shown in Figure 10.1, nanoparticle agglomerates are charged in between two fine screens to make a filter assembly. If the nanoparticles in the filter assembly are slightly compressed, then the bed voidage ε_g will decrease slightly and the size of the pores among the agglomerates will also decrease. This will result in an increase in flow resistance of the pores among the agglomerates. Hence more gas will be forced to penetrate through the permeable agglomerates, and the ratio of the flow penetrating through the permeable agglomerates to the flow passing around the agglomerates will increase. As shown in Equs. (4.1), (4.2) and (4.4), when the bed voidage ε_g decreases, the bed voidage dependent dimensionless parameter η will increase. thus the drag force on a permeable sphere in a swarm of permeable spheres in creeping flow F_{Dp} will correspondingly decrease, and the overall drag force on the particles will also decrease. Hence, although the compression process decreases the bed voidage ε_g, the increase in pressure drop over a swarm of permeable aggloemrates will be smaller than the increase of the pressure drop over a swarm of solid spheres with the same sphere size and flow rate. This is beneficial to the filter design. Based on this analysis, nanoparticle agglomerates in the filter assembly have been slightly compressed before the filtration experiments.

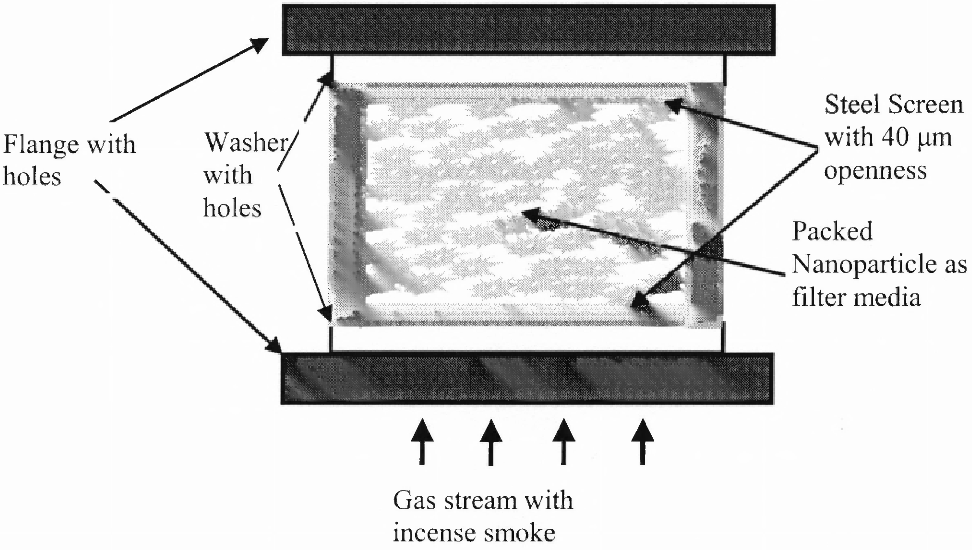

Figure 10.1 Schematic diagram of filter assembly.

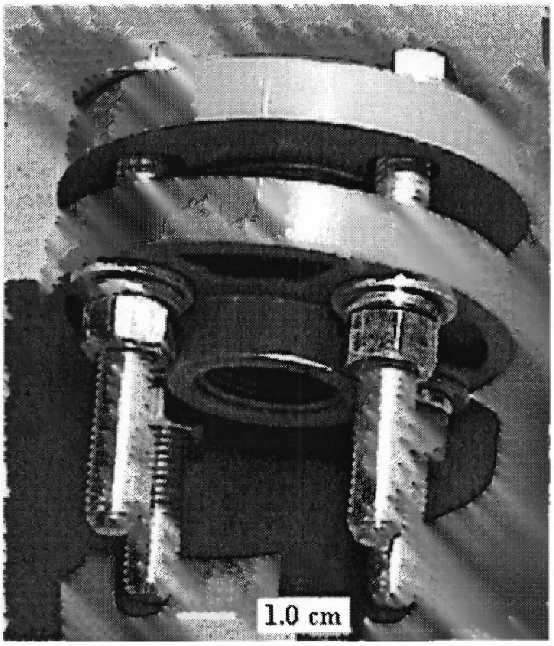

Figure 10.2 Filter assembly.

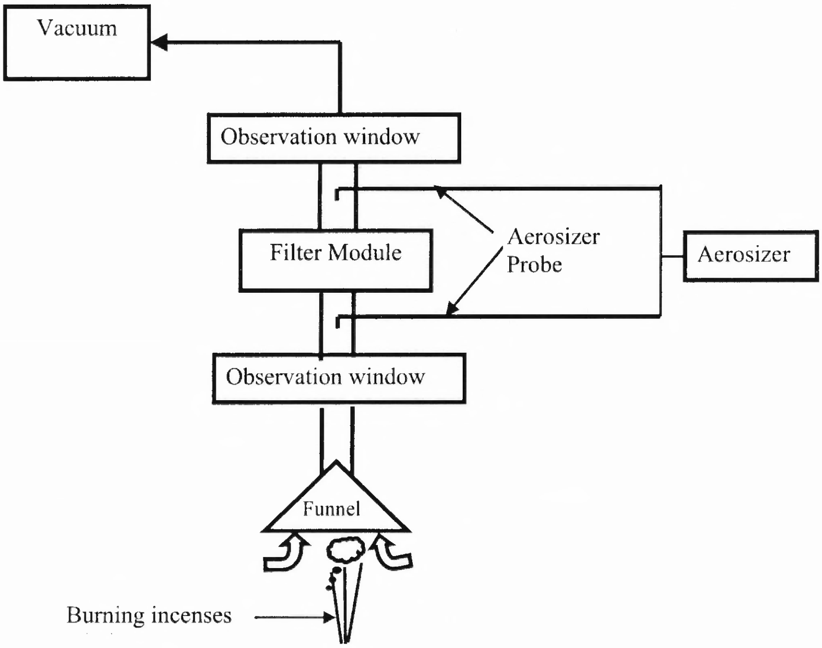

Figure 10.3 Schematic diagram of experimental set-up.

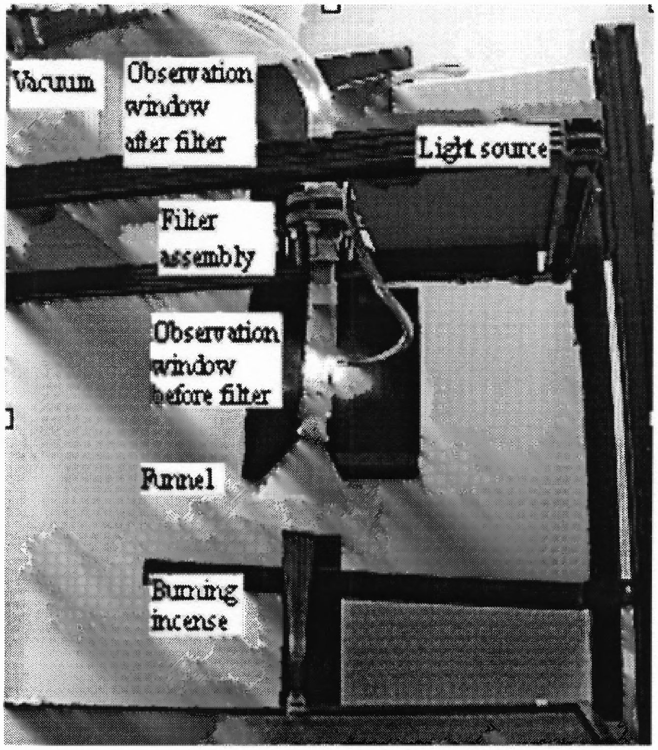

Figure 10.4 Experimental set-up.

The filter was attached to a vacuum pump and a funnel as shown in Figure 10.3 and Figure 10.4. Fourteen sticks of incenses were burned to produce a mixture of smoke and oily liquid droplets at a relatively high concentration, and one stick of incense was burned to produce a mixture at a relatively low concentration. The white smoke generated by the incense is sucked into the transparent vinyl tubing through the funnel by the vacuum and the concentration of smoke before and after the filter is monitored visually by eye and by taking photographs at different times after starting the experiment. Experiments using both filters filled with silica nanoparticles (Degussa Aerosil® A300) or carbon black nanoparticles (Cabot ® fine PEARLS 2000, REGAL 400R, MONARCH 120) were run for 30 minutes and 2 hours. Here, fine PEARLS 2000 is the carbon black nanoparticles after magnetic processing for 60 minutes as described in Chapter 8.

The smoke generated by burning incenses is a combination of submicron solid particles and liquid droplets. As shown in Figure 10.5, an aerosizer system (Amherst Instruments) is used to analyze the filtration efficiency by measuring the number concentration of the smoke for certain size ranges before and after the filters. The results of these experiments will be discussed in next chapter.

The incense sticks that were used in the experiments are typical of the incense commonly burned in Asian temples and were purchased from an Asian store. When burned they will generate a white smoke, which is a mixture of micron and sub-micron sized solid particles and liquid droplets; the size distribution of the smoke as measured by the aerosizer is shown in Figure 10.6.

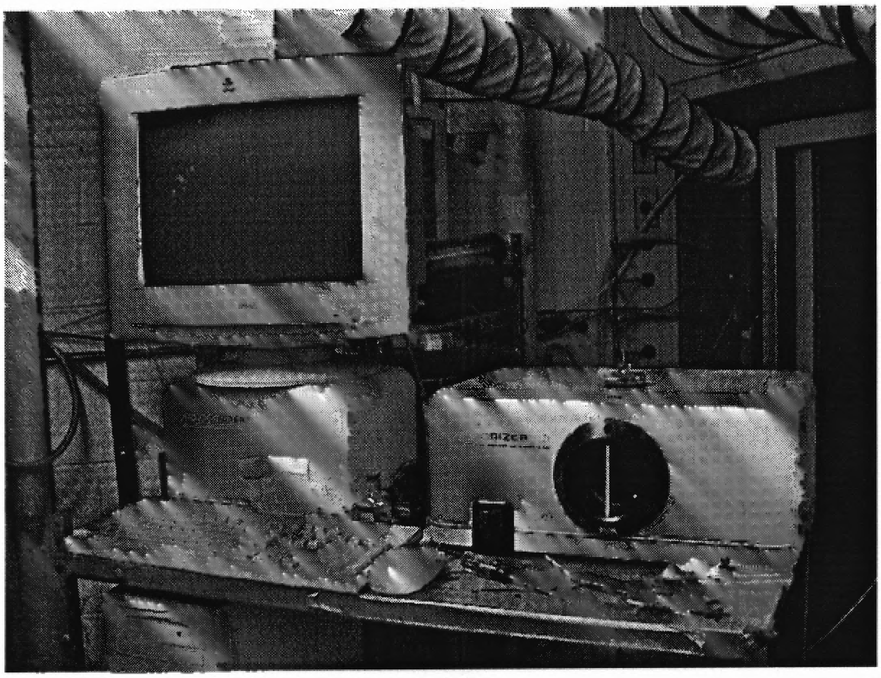

Figure10.5 Aerosizer system.

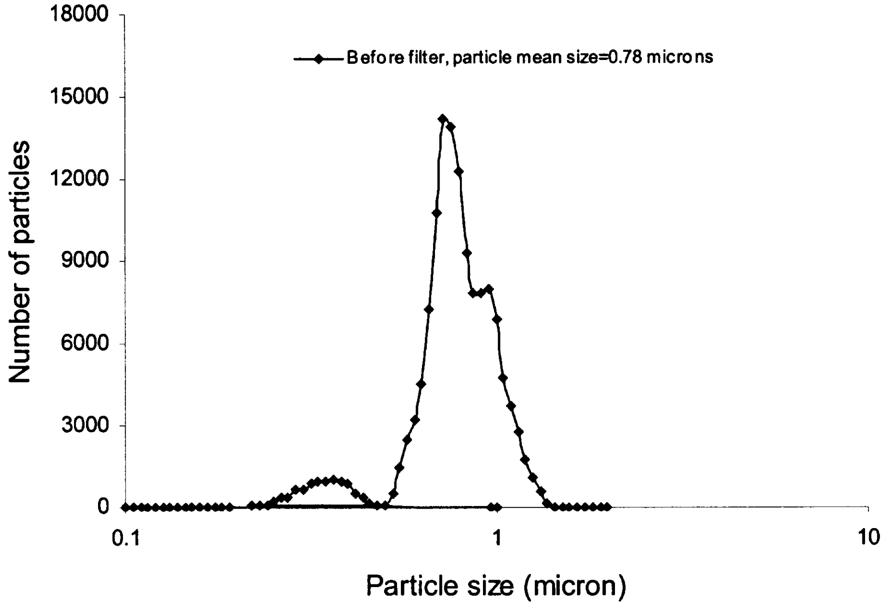

Figure 10.6 Particle size distribution of incense; U_{air}= 4.20 cm/s; sampling time 60 seconds. Mean particle size 0.78 μm.

CHAPTER 11

RESULTS AND DISCUSSION

11.1 Experimental Observation

During the filtration experiments, it was observed that the color of the transparent tubing changes very slowly, going from clear to yellow to brown because of the accumulation of oil and/or water droplets. Also, the lower window (inlet) showed much denser smoke than the upper window, but some smoke could still be observed from the upper window, indicating some penetration. After running both filters for either 30 min or 2 hours, and disassembling them it was found that the 5 mm filter had already become saturated, (Figure 11.1c), but the 16 mm filter was not yet saturated (Figure 11.1d) and appeared similar to the 5 mm filter run for 30 minutes (Figure 11.b). The nanoparticles in the 5 mm filter became completely dark black, and some black liquid-like components were also observed, implying complete saturation.

We also observed that the filter media is consolidated and compressed (Figure 11.1d) which could be due to the vacuum sucking the nanoagglomerates towards the upper screen, the collected liquid droplets affecting the voidage of the nanoagglomerates, or to elutriation of some of the smaller nanoagglomerates. We therefore did a control experiment and ran the vacuum through a clean bed of silica nanoagglomerates in the 16 mm thick filter without burning incense, and measured the weight of the filter media before and after. The weight loss was only 0.3% indicating that elutriation was negligible.

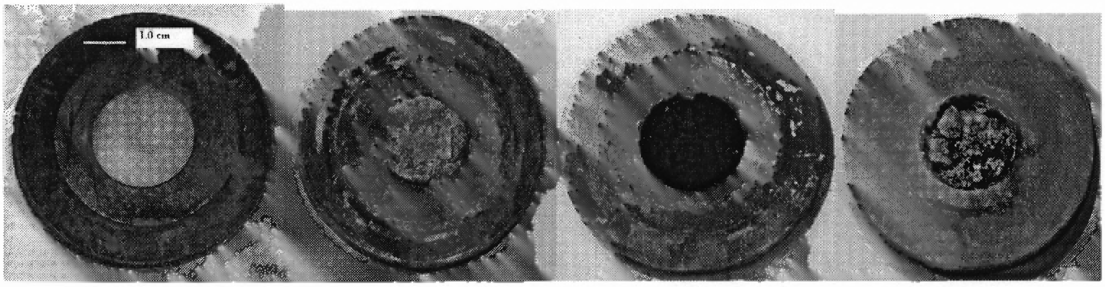

a. clean filter; b. 5mm filter, 30 min; c. 5mm filter, 2 hrs; d. 16mm filter, 2 hrs

Figure 11.1 Filter media after being exposed to burning incense. (Degussa Aerosil® A300)

Table 11.1 shows the mass of the filter media before and after filtration for 2 hours. By using the nanoparticle filter (Silica A300), we obtained a mass increase as high as 491.0 % (16 mm filter, U_{air}= 4.20 cm/s) and 756.4 % (5 mm filter, U_{air}= 14.50 cm/s). Thus the 5mm filter (which appeared saturated) absorbed smoke particles (solid and liquid) as much as 8 times its own weight!

Table 11.1 Mass of nanoparticles (Degussa Aerosil® A300) before and after filtration of burning incense for 2 hours.

	Mass after 2 hours' filtration without burning incensed M_0 (g)	Mass after 2 hours' filtration M_1 (g)	$\Delta M = M_1 - M_0$ (g)	$\frac{\Delta M}{M_0}$
5mm filter	0.0741	0.6346	0.5605	756.4 %
16mm filter	0.1501	0.8871	0.7370	491.0 %

Figure 11.2 is a picture of the filter media after being exposed to the burning of incense for 30 minutes. At location A the filter media is facing the outlet of the filter, and the nanoparticle agglomerates are still white, indicating that the burning incense has not yet penetrated to this depth; at location B the filter media is facing the inlet of the filter,

and the nanoparticle agglomerates have been contaminated by the burning incense. This figure clearly indicates that the nano filter acts as a deep bed filter, instead of a surface filter as observed in a HEPA fiber-based filter. Furthermore, as will be discussed below, we used a HEPA filter for comparison and found that it turned almost completely black from the burning incense within several minutes, while our nanoagglomerate filter media lasted for over 2 hours.

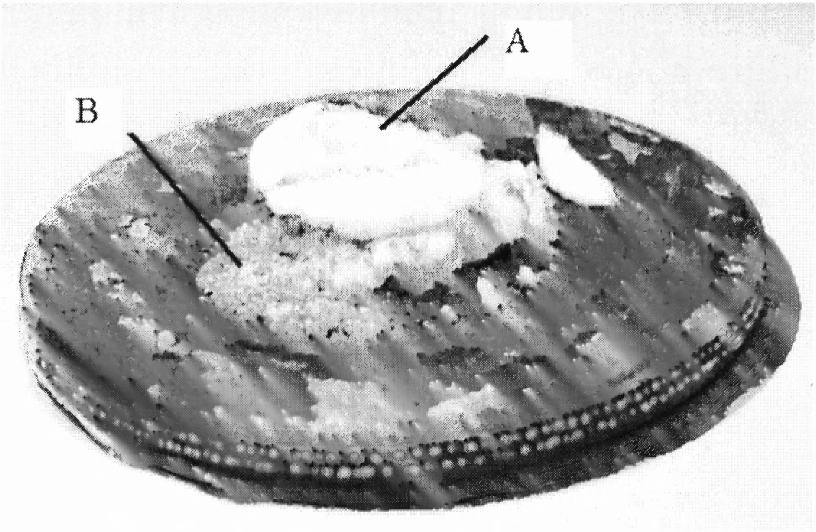

Figure 11.2 Filter media after being exposed to burning 14 sticks of incenses for 30 minutes. 16 mm filter, Degussa Aerosil® A300. Location A is the filter media facing the outlet of the filter; location B is the filter media facing the inlet of the filter.

11.2 Penetration of Nanoparticle Filter

The particle size distribution of smoke generated by burning 14 sticks of incense as measured with an Aerosizer (Amherst Instruments) before and after the 5mm and the 16mm filters are shown in Figures 11.3; the particle size distribution before and after a HEPA filter are also shown as a comparison. The HEPA filter is cut from a commercial HEPA filter module (McMaster 9179K11, thickness of 0.7mm, cut-off size of 0.3μm), and is installed in the filter module. As seen in Figure11.3, at a superficial air velocity of 4.20 cm/s, the inlet incense smoke had a mean size of 0.78μm, and during a sampling time of 60 seconds, the number of particles counted by the aerosizer (particle number) was 134600.

After the HEPA filter, the number of particles only decreased to 52,800 and the mean size decreased slightly to 0.51μm. However, for the 5mm thick nano filter, the number of particles decreased to 13612 and the mean size decreased to 0.41μm, and for the 16mm thick nano filter, the number of particles decreased to 832, and the mean size decreased to 0.35μm. It can also be seen in Figure 11.3 that the effluent particle size distribution shifts to the left (smaller size) for both the HEPA filter and the 5mm nano filter; there is practically no penetration for the 16mm nano filter. This unusual observation is probably due to the relatively high inlet concentration of smoke particles (solid and liquid) produced by the burning incense, which causes them to form agglomerates before entering the filter. These agglomerates will be broken up as they move through the filter, and therefore any particles that are not captured in the filter media will tend to be smaller in size.

Table 11.2 is the comparison results of particle penetration by particle number and by particle weight for the HEPA and the nano filters. At an air velocity of 4.20cm/s, the nano filters have higher filtration efficiencies than the HEPA filter. For example, the penetration by total number of particles for the HEPA filter is 0.392, whereas the 5mm and nano filter show much lower penetrations of 0.101and 0.003, respectively. The comparative results for the penetration by particle weight are also listed in the table.

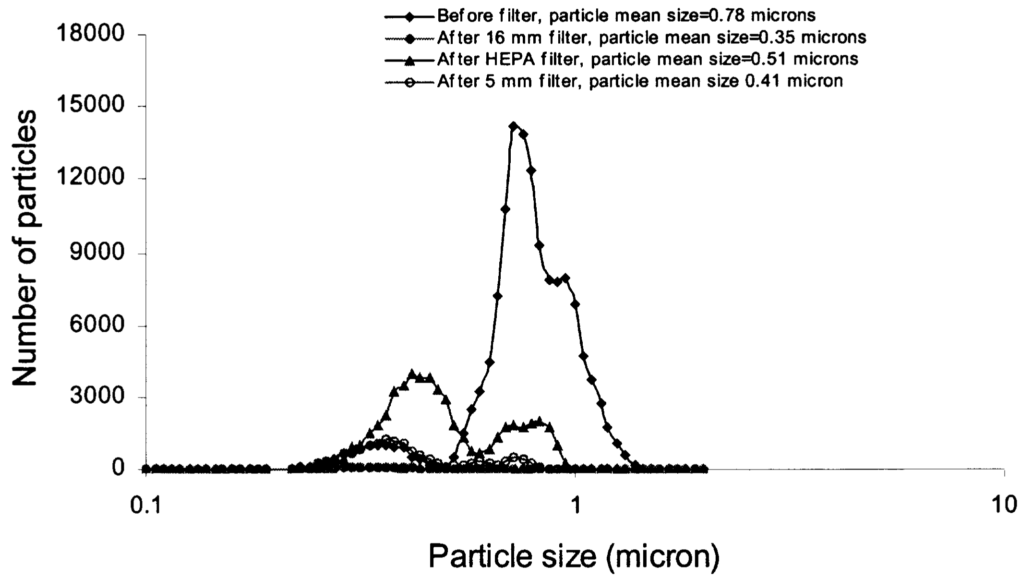

Figure 11.3 Particle size distribution of smoke generated by burning 14 sticks of incense before and after the 5 mm filter and 16 mm filter (Degussa A300, agglomerate size<500 μm), and after the HEPA filter; U_{air}= 4.20 cm/s; sampling time 60 seconds.

Table 11.2 Comparison of the particle penetration of the 5mm and 16mm nano filters with a HEPA filter.

U_{gas} (cm/s)	Sampling position	Mean particle size (μm)	Number of particles counted in 60 s	Penetration (by total number) of particles	Mass of particles less than 1μm ($\times 10^{-12}$g)	Penetration (by mass) of particles less than 1μm
4.20	Before filter	0.78	134600	------	29630.0	------
	After HEPA filter	0.51	52800	0.392	5255.9	0.177
	After 5mm nanofilter	0.41	13612	0.101	743.4	0.025
	After 16mm nanofilter	0.35	832	0.006	19.0	0.0006

To investigate the penetration of aerosols at a relatively low concentration, another set of experiments are performed. Figure 11.4 shows the particle size distribution of smoke generated by burning only one stick of incense as measured with an Aerosizer (Amherst Instruments) before and after the 5mm filter filled with silica nanoparticles (Degussa Aerosil® A300) and carbon black nanoparticles (Cabot ® fine PEARLS 2000, REGAL 400R, MONARCH 120). As seen in Figure 11.4, at a relatively low concentration of aerosols, the penetration decreases with the filter media used in the following order: HEPA, REGAL 400R, MONARCH 120, A300, and fine PEARLS 2000, This indicates that all the nanoparticle filters tested have a higher filtration efficiency that the HEPA filter, and the carbon black nanoparticle PEARLS 2000 after magnetic fragmentation processing shows the highest filtration efficiency.

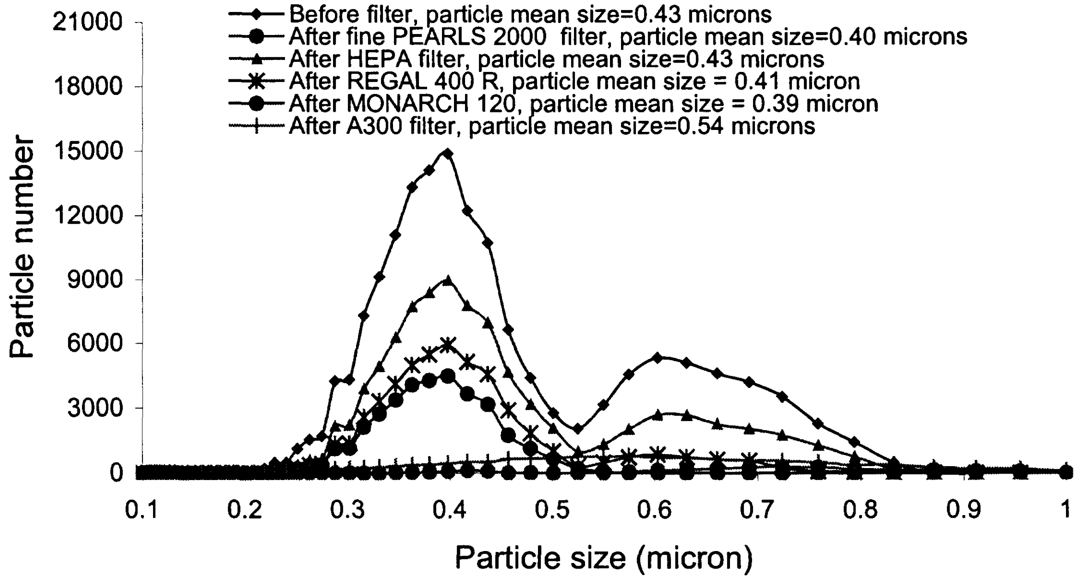

Figure 11.4 Particle size distribution of smoke generated by burning one stick of incense before and after the 5 mm filter (Degussa A300, Cabot ® fine PEARLS 2000, REGAL 400R, MONARCH 120, agglomerate size<500 μm), and after the HEPA filter; U_{air}= 4.20 cm/s; sampling time 300 seconds.

11.3 Pressure Drop Across the Degussa A300 Nanoparticle Filter

Figure 11.5 is a plot of the pressure drop of the clean filters (before exposure to the incense smoke) versus air velocity. The nano filters show a higher pressure drop than the HEPA, e.g., at a superficial air velocity of 4.20 cm/s, the pressure drop of the 5mm nano filter is 92mm H_2O compared to 66mm for the HEPA filter, but the increase in pressure drop is within an acceptable range.

Moreover, the pressure drop across the 5mm filter remains relatively constant with time before saturation and then rises sharply when the filter becomes saturated (Figure 11.6) indicating that the nanoagglomerates act as a deep bed filter. During the filtration experiment, the liquid droplets and solid particulates in the gas stream will first be trapped on the surface of the nanoparticle agglomerates, and also be sucked into the porous agglomerates. Before saturation, the pores among the agglomerates will remain open, and the pressure drop across the filter will remain almost constant. But after the interior of the nanoparticle agglomerates are saturated, the pores among the agglomerates will begin to be quickly filled with liquid droplets and solid particulates, the bed voidage around agglomerates ε_g will significantly decrease within a short period of time. Once the pores are fully filled with liquid droplets and solid particulates, the pressure drop across the filter will suddenly jump up. Hence, the pressure drop across the filter will behave as shown in Figure 11.6.

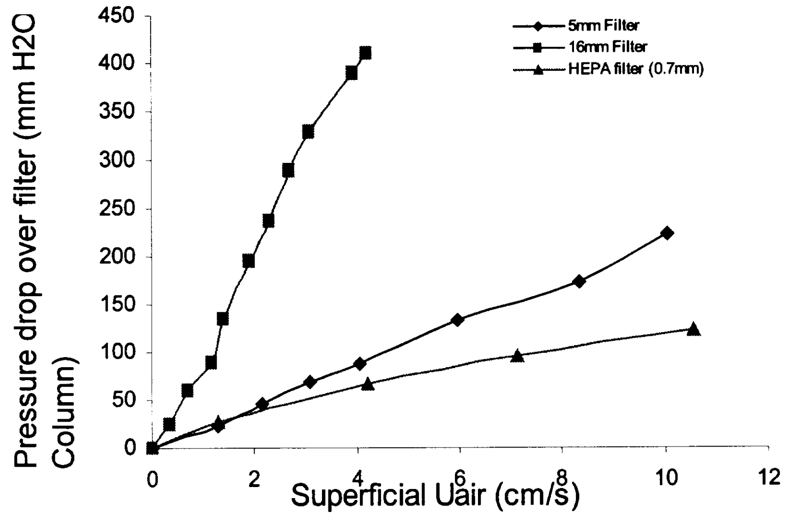

Figure 11.5 Pressure drop across the 5mm, 16mm and HEPA filters.

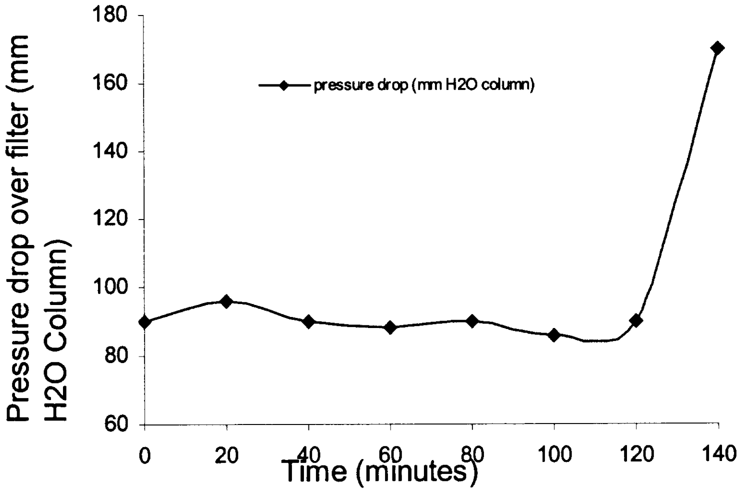

Figure 11.6 Pressure drop across the 5 mm filter as a function of time. Uair=4.20 cm/s. Filter media: Degussa A300; 14 sticks if incense.

11.4 SEM Images

Figure 11.7 shows highly magnified SEM images (100 nanometer scale) of the fresh A300 nanoagglomerates showing the extremely porous structure and the ~1μm primary agglomerates.

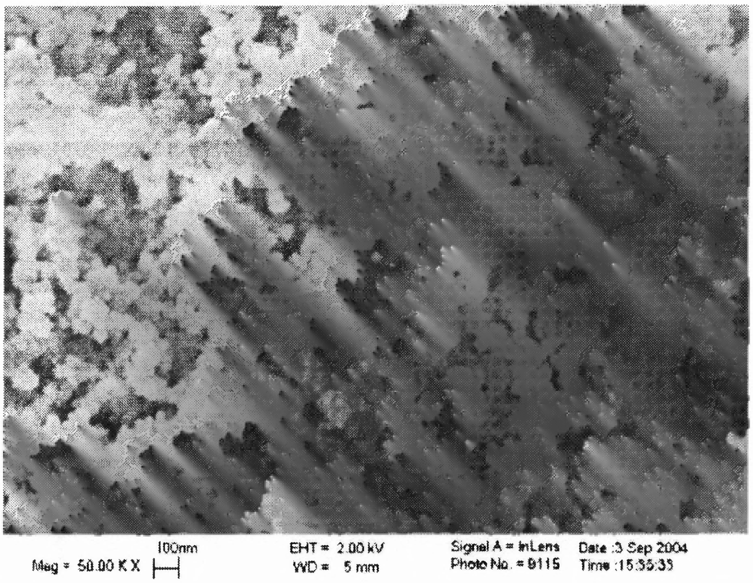

Figure 11.7 Image of fresh nanoagglomerates in the 5 mm filter. (Degussa Aerosil®A300)

The images in Figure 11.8a and b, also at the 100nm scale, show the nanoagglomerates facing the inlet and the outlet side, respectively, of the 5 mm thick filter after being exposed to incense smoke for 30 minutes. Figure 11.7a shows that the nanoparticles are covered with a tar-like material and that the primary agglomerates appear glued together. The image of Figure 11.8b however, is very similar to that of the fresh powder shown in Figure 11.7 indicating that the burning incense smoke has not yet contaminated this end of the filter.

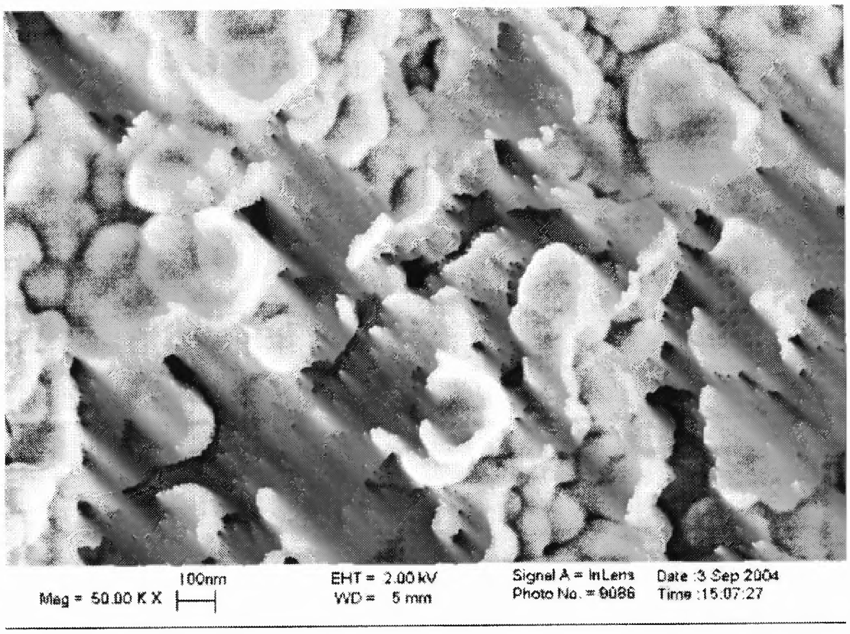

Figure 11.8a. Image of nanoagglomerates after 30 min. of filtration, unsaturated, facing the inlet of the filter. (Degussa Aerosil® A300)

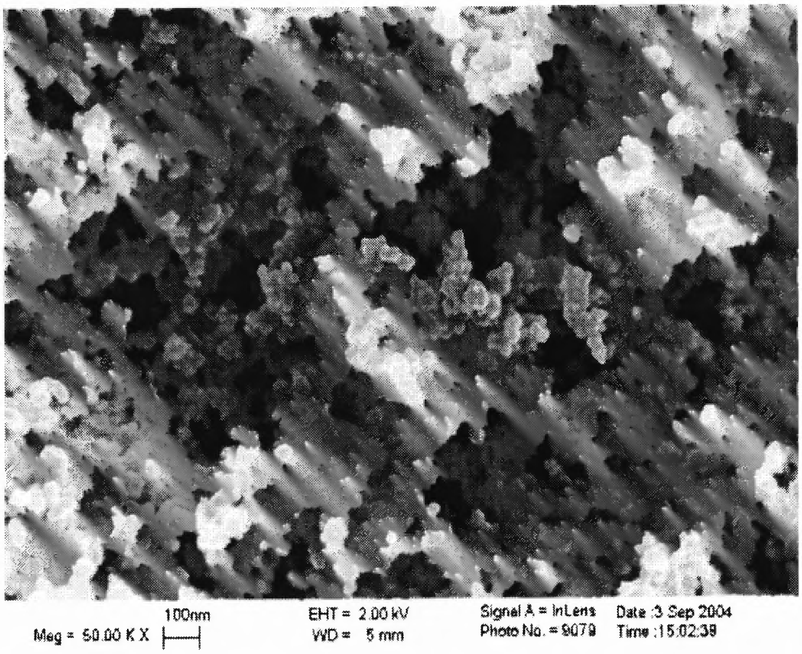

Figure 11.8b. Image of nanoagglomerates after 30 minutes of filtration, unsaturated, facing the outlet of the filter. (Degussa Aerosil® A300)

Figure 11.9 shows the nanoagglomerates after being exposed for 2 hours. The entire filter media appeared saturated with the tar-like material and no visual difference in the saturated nanoagglomerates could be observed at the two ends of the filter. These figures provide further confirmation that the nanoagglomerates act as a deep bed filter rather than a cake-forming surface filter, characteristic of fiber-based HEPA filters.

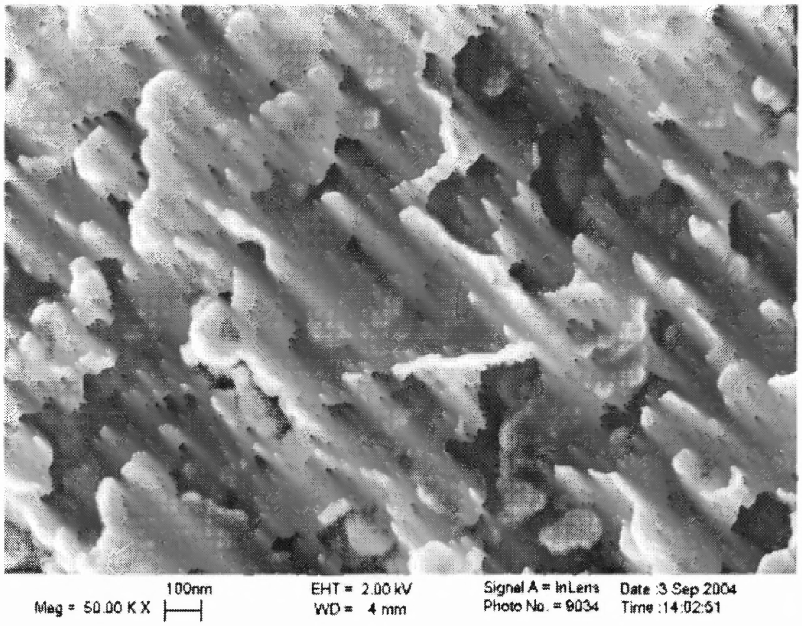

Figure 11.9 Image of nanoagglomerates after a 2 hours of filtration, saturated. (Degussa Aerosil® A300).

Figure 11.10 and 11.11 show a comparison of SEM images of carbon black nanoparticles (Cabot ® fine PEARLS 2000, after magnetic processing) before and after the filtration experiments. As seen in Figure 11.10, the fresh carbon black nanoparticles have a clean surface. After a 1-hour of filtration, the nanoparticle agglomerates appear to have trapped some water or oil droplets. These figures provide further evidence that sub-micron particulates can be filtered by the nanoagglomerates.

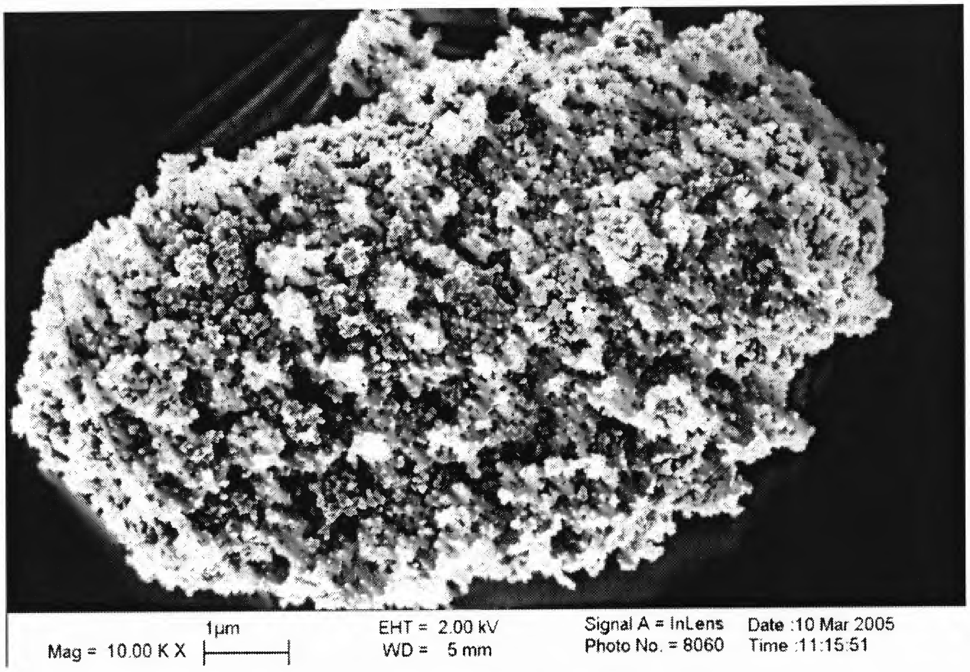

Figure 11.10 Image of fresh nanoagglomerates in the 5 mm filter. (Cabot ® fine PEARLS 2000, carbon black)

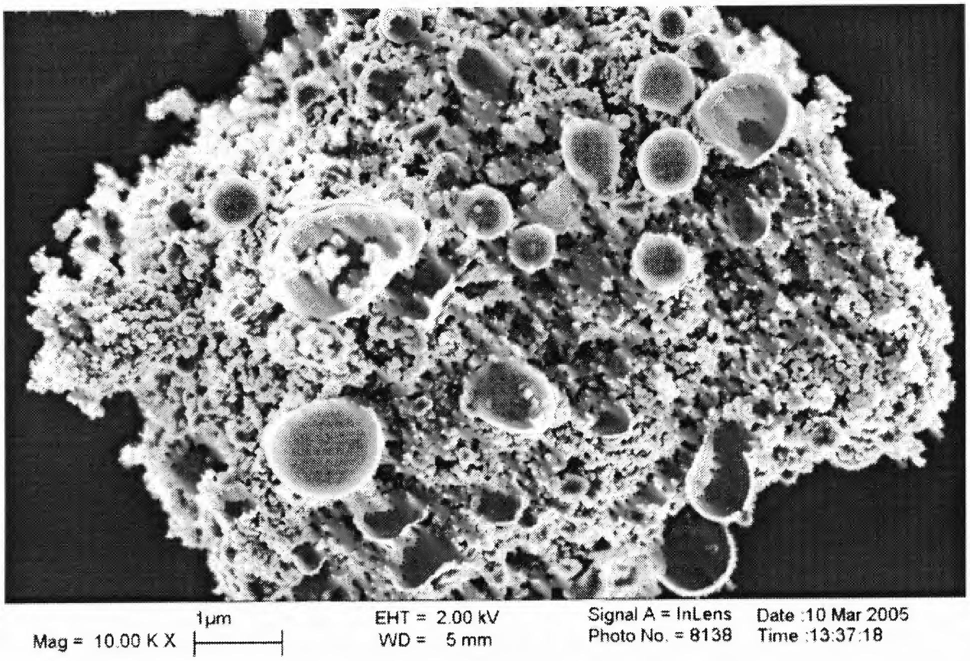

Figure 11.11 Image of nanoagglomerates after a 1 hour filtration. (Cabot ® fine PEARLS 2000, carbon black)

11.5 Concluding Remarks

From the preliminary experiments performed in this study, it appears that fractal hierarchical structured nanoagglomerates, such as fumed silica Degussa Aerosil® A300 and carbon black nanoparticles (Cabot ® fine PEARLS 2000, REGAL 400R, MONARCH 120) can be used as a substitute filter media in a HEPA filter, to remove the submicron sized solid particles and liquid droplets. The nanoagglomerate-based HEPA filters can absorb a large amount of submicron particles, even as much as 8 times of its own weight before saturated, showing high filtration capacity.

The nanoagglomerate-based HEPA filters result in low penetration for MPPS as 0.0006 or 0.025 for the two filters tested, at an acceptable pressure drop level, showing high efficiency (lower penetration) to remove submicron size particulates. Both sizing measurement and SEM images support this observation.

The nanoagglomerate-based HEPA filters work as a deep bed filter, rather than a cake-forming surface filter as the traditional fiber-based HEPA filters.

11.6 Limitation of this Study and Future Research Directions

Filtration of submicron particles using nanoparticle agglomerates is a completely new area, and this study only performed some very preliminary qualitative experimental tests. Hence there are many new research directions, which must be explored to determine whether, or not, a nanoagglomerate filter will be able to compete with a fiber-based HEPA filter.

Variables such as the size and specific surface area of the primary particles, surface treatment, hydrophobicity and hydrophilicity, porosity, mean size of the large agglomerates, subagglomerates (SA) and primary agglomerates (PA) will significantly influence the absorption efficiency and capacity for submicron particles. Quantitative experimental studies using aerosols of specified properties (rather than incense smoke) and much more accurate particle counters must be performed so as to optimize the performance of the nanoagglomerate filter media.

In addition, in order to be able to predict the single particle collection efficiency and penetration of MPPS particles and to be able to choose the properties of fractal nanoagglomerates which will provide the best results, with respect to penetration, pressure drop and capacity, theoretical modeling needs to be developed.

PART IV: CORE-ANNULUS-WALL STRUCTURE IN A CIRCULATING FLUIDIZED BED RISER

This part will focus on modeling the core-annulus-wall structure in a circulating fluidized bed riser. Chapter 12 will summarize the existing literature and describe the existing experimental results, Chapter 13 will introduce the mechanisms, while modeling work on the acceleration region will be included in Chapter 14. The modeling results and discussion related to the core-annulus-wall structure in a circulating fluidized bed riser appears in Chapter 15. A numerical solution algorithm is given in Appendix A, and a sample input file in Appendix B.

CHAPTER 12

LITERATURE REVIEW

Recent experimental studies using Electrical Capacitance Tomography (ECT) show that there exists a double ring structure in solids concentration in a circulating fluidized bed riser (Du *et al.*, 2004). It was found that the solid concentrations at the dense core region can be as high as five times of those at the dilute annulus region, which indicates that the radial flow structure for a dense circulating fluidized bed should be treated as a core-annulus-wall three-region structure, instead of the well-known core-wall two-region structure. A typical example of such a measurement is shown in Figure 12.1. The color change indicates the variation of solids holdup. It is further found that near the riser bottom, the solids concentration in the core is much denser than the solids in the annulus whereas the solids concentration in the core is less than that in the annulus near the riser top. Across any cross-section, the solids near the wall have the highest concentration.

This core-annulus-wall structure appears to be stable along the riser, and holds for a wide range of CFB operation conditions.

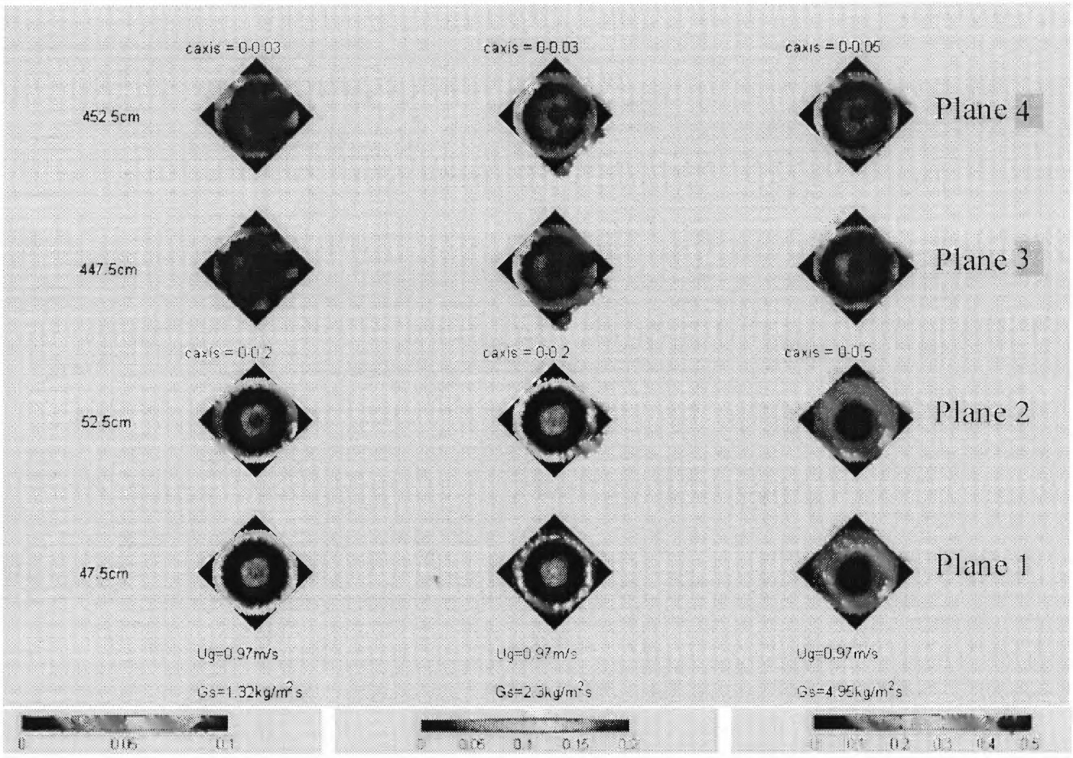

Figure 12.1 Wall-Annulus-Core Structure in CFB (Du *et al.*, 2004).

Figure 12.2 shows the experimental setup that is used to obtain the results shown in Figure 12.1. The ECT measurement yields the time averaged cross-sectional distribution of solids holdup at four different locations, with Planes 1 and 2 near the bottom and Planes 3 and 4 near the top of the riser. Detailed descriptions of the experimental methods and operation conditions can be found in Du *et al.* (2004).

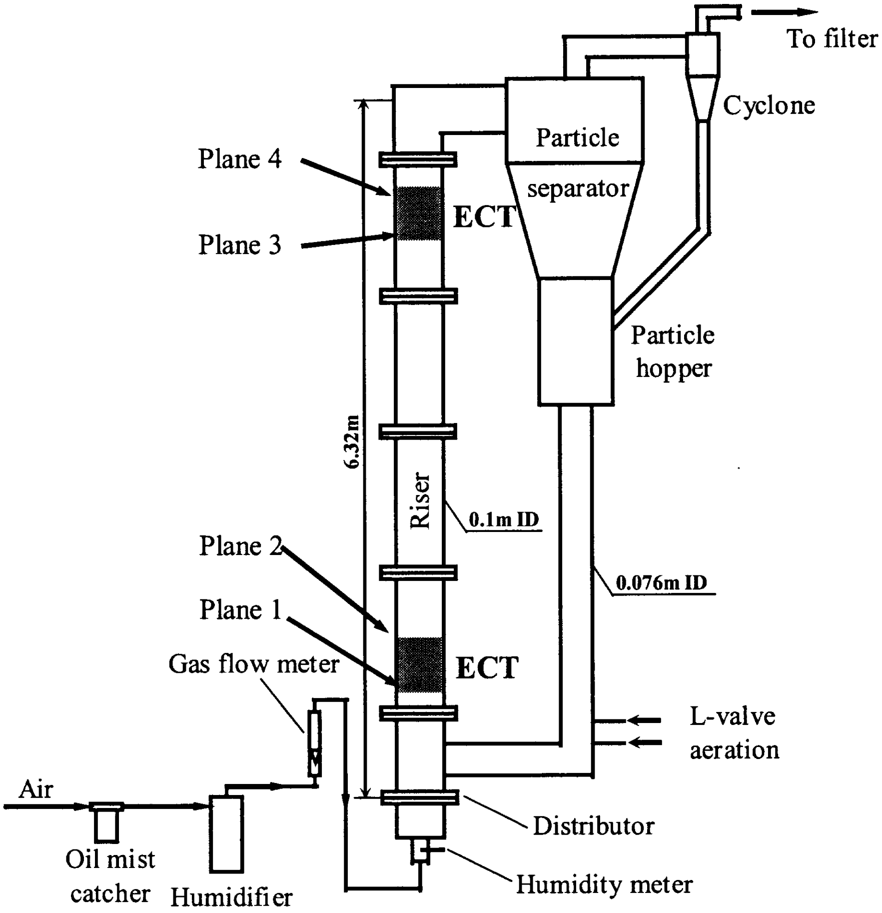

Figure 12.2 Experimental system and locations of ECT measurements in Du *et al.* (2004).

This study will first discuss the formation mechanisms of the core-annulus-wall structure in a CFB riser. Secondly, an analytic model is developed for quantifying the flow structure in the developing regime, especially the solids concentration in the core. In addition, we provide a rough evaluation of the effect of solids acceleration on the solid holdup measurement that is determined from pressure gradient measurements in a CFB riser. The detailed mechanistic explanation, modeling and results will be included in the following chapters.

CHAPTER 13

MECHANISTIC EXPLANATION

Consider a CFB riser with a uniform gas-solids flow at the riser inlet, as shown in Figure 13.1. As the solids move upward against gravity, a wall (boundary layer) region is developed where the gas velocity is low and the solids concentration is high. At some bed height, the solids in the wall region have exhausted all their initial upward momentum and begin to move downward. At this location the solids velocity in the wall region is null. Hence, in a bed section near this height, all solids from the upper wall region or from the lower wall region are forced to migrate inward towards the riser column center (Rhodes *et al.*, 1998).

As a result, and due to axial symmetry of the CFB column, a dense core region must be formed, as shown in Figure 13.1. While all solids are accelerated in this developing region, the radial distribution of axial gas velocity is by no means uniform. Since a nearly equal pressure gradient must exist in all regions at the same bed height, the gas velocity in the core tends to be lower than that in the annulus where the solids concentration is less. This lowered gas velocity in the core leads to a slower solids acceleration in the core, and hence preserves the core-annulus-wall structure with a higher solids concentration at the core. However, based on a mass balance of solids, the downward moving solids in the wall region in the upper part of a riser must come from those solids in the annulus and core. Hence, in the upper part of the riser, the solids migration into the wall results in a depletion in solids concentration, which is more severe in the core than in the annulus. Therefore, near the top of a riser, a core-annulus-wall structure still exists but with less solids in the core than in the annulus. In summary, the core-annulus-wall flow structure can be fully explained, in good agreement with the ECT findings in Figure 12.1.

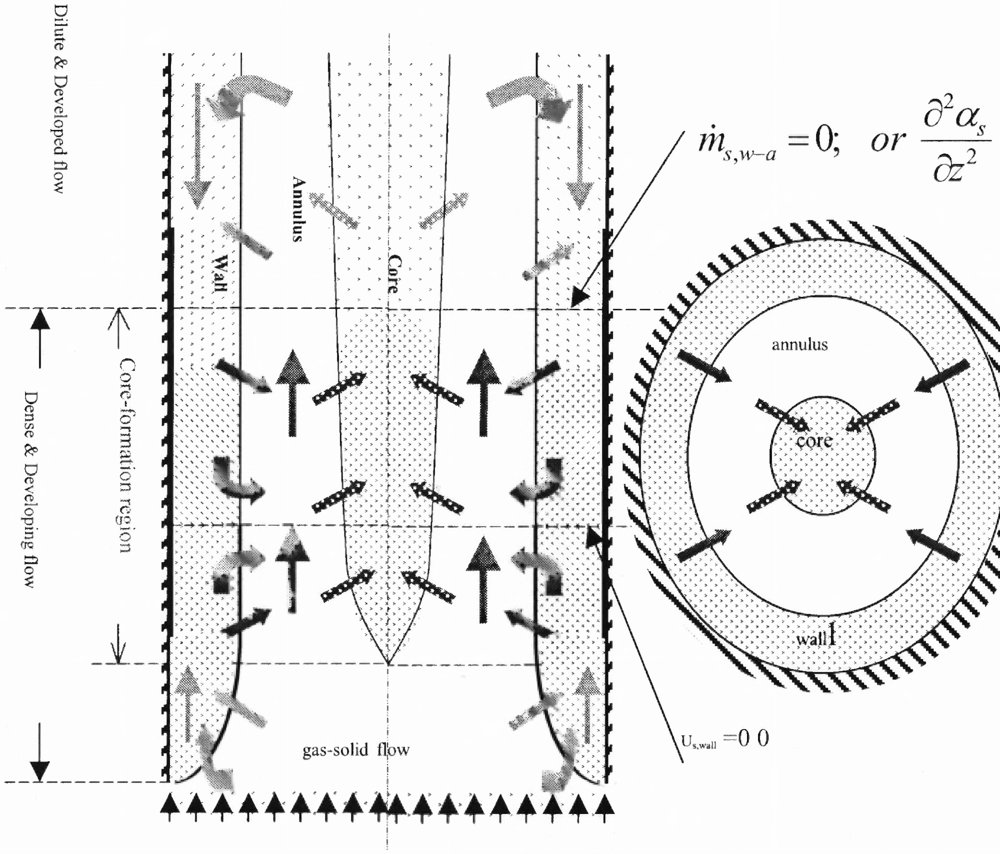

Figure 13.1 Core-annulus-wall structure in CFB.

CHAPTER 14

MODELING OF DEVELOPING FLOW IN CORE-ANNULUS-WALL REGIONS

To simplify our analysis, it is assumed that at any bed height and within each region, the solids are uniformly distributed. Figure 14.1 shows that the actual radial distribution of the solids concentration near the bottom of a CFB riser can be reasonably approximated by a three-zone structure.

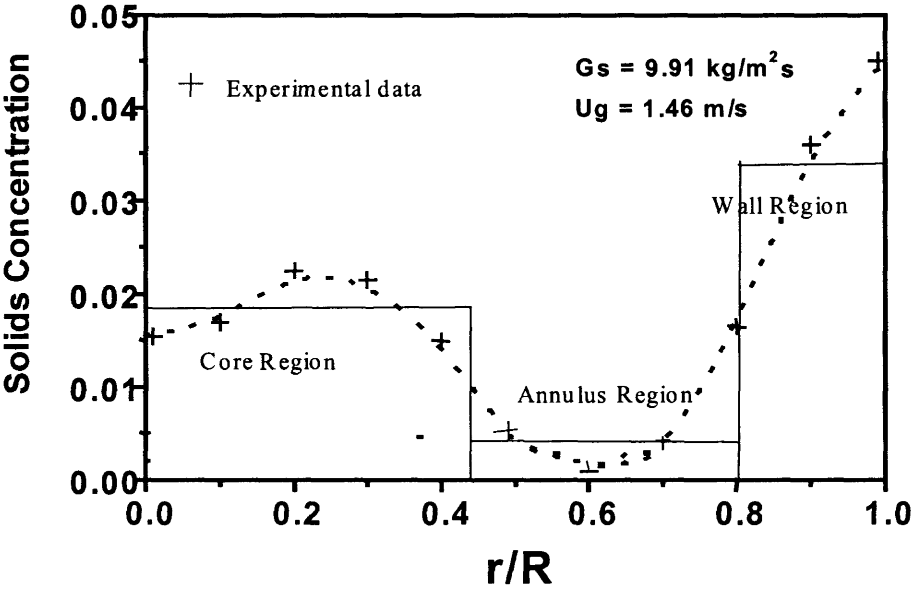

Figure 14.1 Three-zone representation of solids concentration distribution.

14.1 Governing Equations

To describe the flow in a CFB riser with the core-annulus-wall flow structure, fourteen independent equations or correlations must be developed for fourteen independent variables. These variables include gas velocities, solid velocities and solid volume fractions in each region, region cross-sectional areas, solids flows across regional interface and the pressure drop. The following is a summary of the equations.

Solid Mass Balance

Overall balance: $$\dot{M}_s A = \rho_s \alpha_{sc} U_{sc} A_c + \rho_s \alpha_{sa} U_{sa} A_a - \rho_s \alpha_{sw} U_{sw} A_w \tag{14.1}$$

Core-region: $$\frac{d}{dz}(\alpha_{sc} \rho_s U_{sc} A_c) = \dot{m}_{sac} 2\pi R_c \tag{14.2}$$

Wall-region: $$\frac{d}{dz}(\rho_s \alpha_{sw} U_{sw} A_w) = +\dot{m}_{swa} 2\pi R_a \tag{14.3}$$

Gas Mass Balance

$$\dot{M}_g A = \rho_g (1-\alpha_{sc}) U_{gc} A_c + \rho_g (1-\alpha_{sa}) U_{ga} A_a + \rho_g (1-\alpha_{sw}) U_{gw} A_w \tag{14.4}$$

Gas Momentum Balance

Core-region: $$\frac{dp}{dz} = -\alpha_{sc} C_{Dc} \left(\frac{3}{4}\frac{\rho_g}{d_s}\right)(U_{gc} - U_{sc})^2 \tag{14.5}$$

Annulus-region: $$\frac{dp}{dz} = -\alpha_{sa} C_{Da} \left(\frac{3}{4}\frac{\rho_g}{d_s}\right)(U_{ga} - U_{sa})^2 \tag{14.6}$$

Wall-region: $$\frac{dp}{dz} = -\alpha_{sw} C_{Dw} \left(\frac{3}{4}\frac{\rho_g}{d_s}\right)(U_{gw} + U_{sw})^2 \tag{14.7}$$

Solids Momentum Balance

Core-region: $$\frac{d}{dz}(\alpha_{sc} \rho_s U_{sc}^2 A_c) = F_{Dsc} - \alpha_{sc} A_c \rho_s g + \dot{m}_{sac} (2\pi R_c) U_{sa} \tag{14.8}$$

Annulus-region:

$$\frac{d}{dz}(\alpha_{sa} \rho_s U_{sa}^2 A_a) = F_{Dsa} - \alpha_{sa} A_a \rho_s g - \dot{m}_{sac} (2\pi R_c) U_{sa} - \dot{m}_{swa} (2\pi R_a) U_{sw} \tag{14.9}$$

Wall-region: $$\frac{d}{dz}(\alpha_{sw} \rho_s U_{sw}^2 A_w) = F_{Dsw} - \alpha_{sw} A_w \rho_s g + \dot{m}_{swa} (2\pi R_a) U_{sw} \tag{14.10}$$

Solids Flow Across Regional Interface

The solids transfer across the regional interface is given by Equ. (14.1), diffusive transfer due to the solids concentration difference between the two regions and Equ. (14.2), turbulence convection.

Core-Annulus interface:
$$\dot{m}_{sac} = \rho_s D_s(\alpha_{sa} - \alpha_{sc}) + \frac{1}{6}\rho_s(k'_a \alpha_{sa} U_{sa} - \alpha_{sc} U_{sc} k'_c) \qquad (14.11)$$

Annulus-Wall interface:
$$\dot{m}_{swa} = \rho_s D_s(\alpha_{sw} - \alpha_{sa}) + \frac{1}{6}\rho_s(k'_w \alpha_{sw} U_{sw} - \alpha_{sa} U_{sa} k'_a) \qquad (14.12)$$

Definition of Regional Boundaries

Two equations should be defined for the demarcation of regional boundaries. Based on ECT measurements, in this study, we propose two simple equations:

$$\frac{dA_w}{dZ} \approx 0 \qquad (14.13)$$

$$\frac{A_c}{A_a} = C \qquad (14.14)$$

14.2 Solids Holdup in Developing Flow in a CFB Riser

The power dissipation due to the solids-wall friction and inter-solids collisions is not included in the above model. For solids accelerating in a dense suspension, this effect could be important. Hence, a further examination of the power partitions from the axial pressure gradient for solid suspension, solid collision, and solid acceleration is conducted for the 1-D flow case.

Due to solids acceleration and the energy dissipation from solid collisions in the developing regime (typically near the bottom of CFB riser), the measured axial pressure gradient tends to overestimate the solid holdup, as given by Equ. (14.15):

$$-\frac{dP}{dZ}=\alpha_s\rho_s g+\alpha_s\rho_s U_s\frac{dU_s}{dZ}+F_f \tag{14.15}$$

Rearranging the above equation yields

$$1=\frac{\alpha_s\rho_s g}{\left(-\frac{dP}{dZ}\right)}+\frac{\alpha_s\rho_s U_s\frac{dU_s}{dZ}}{\left(-\frac{dP}{dZ}\right)}+\frac{F_f}{\left(-\frac{dP}{dZ}\right)}=\delta+\chi+\beta' \tag{14.16}$$

where β' stands for the power fraction from the axial pressure gradient due to the inter-particle collision and solid-wall friction; χ is the power fraction from the axial pressure gradient to promote solids acceleration; and δ is the power fraction from the axial pressure gradient to keep the solids suspended. Typical distributions of β' and χ vs. apparent solid holdup, i.e., axial pressure gradient, are schematically plotted in Figure 14.2. Hence, the solids holdup can be expressed as:

$$\alpha_s=\frac{1}{\rho_s g}\left(-\frac{dP}{dz}\right)(1-\beta'-\chi) \tag{14.17}$$

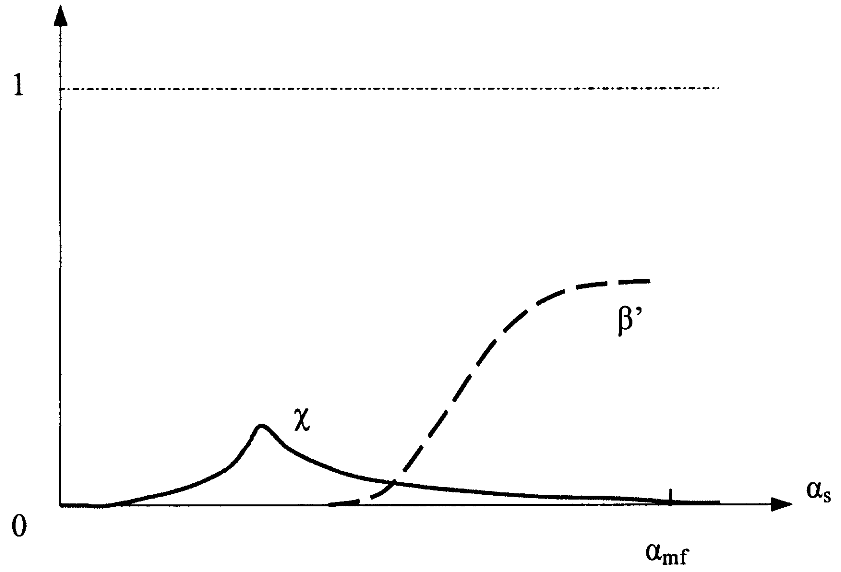

Figure 14.2 Schematic plot of β' and χ vs. apparent solid holdup.

Figure 14.3 shows a typical plot of χ as a function of apparent solids holdup, which is derived based on the experimental data in Sun *et al.* (1999).

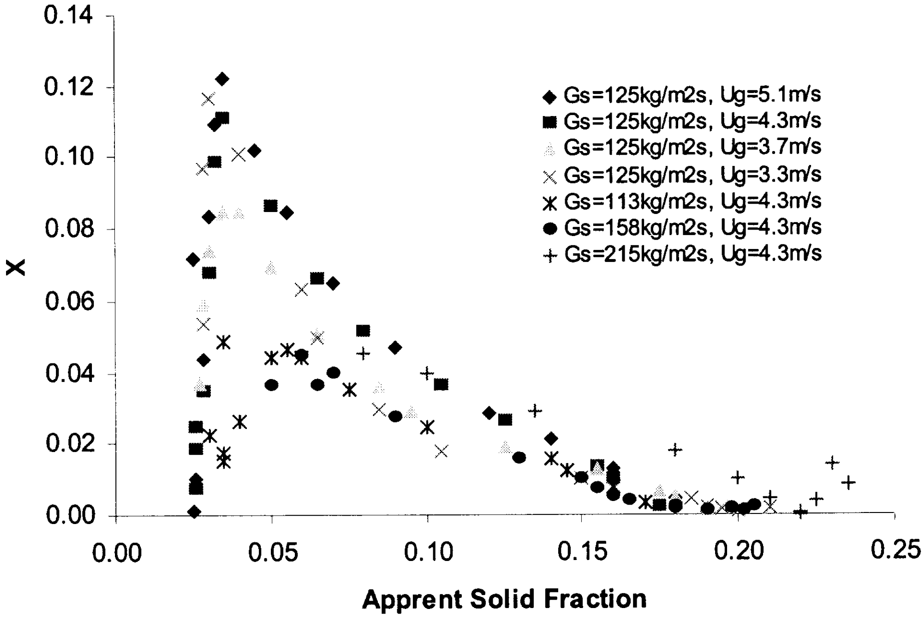

Figure 14.3 Example of χ vs. apparent solid holdup (based on data in Sun *et al.*, 1999).

14.3 Determination of β'

In a circulating fluidized bed riser, the power fraction from the axial pressure gradient β' is due to inter-particle interactions that include the neighboring particle effect (Zhu *et al.*, 1994; Liang *et al.* 1996) and the kinetic energy dissipation by solids collision (Fan & Zhu, 1998).

Defining F'_{Ds} as the drag force on a solid particle in a swarm of particles experiencing strong inter-particle collisions, and F_{Ds} as the drag force on a solid particle in an infinite large space, the power fraction from the axial pressure gradient due to inter-particle interactions β' can be expressed by:

$$\beta = \frac{F_{Ds}^{'}}{F_{Ds}} \tag{14.18}$$

According to kinetic theory, the drag force due to the kinetic energy dissipation can be expressed as

$$F_{Ds}^{'} = \gamma \cdot A_s \cdot U_s \tag{14.19}$$

where γ is the kinetic energy dissipation rate, and A_s is the cross section of the solid particle.

According to kinetic theory (Fan & Zhu, 1998), the kinetic energy dissipation rate γ can be expressed as

$$\gamma = \frac{6(1-e^2)}{d^2} \cdot 2\rho_s \alpha_s^2 g_0 \cdot d_s \cdot T_c^{3/2} \cdot \frac{1}{\sqrt{\pi}} \tag{14.20}$$

where g_0 is the radial distribution function, and its value is 1.0; T_c is the granular temperature, which can be expressed as a function of solid velocity fluctuation:

$$T_c = \frac{1}{3} U_s^{'2} \tag{14.21}$$

Substituting Equs. (14.19), (14.20) and (14.21) into Equ. (14.18), β can be expressed as

$$\beta' = \frac{4(1-e^2)}{\sqrt{3\pi}} \rho_s \alpha_s^2 \left(\frac{A_s}{d_s} \right) \left(\frac{\sqrt{U_s^{'2}}}{\overline{U_s}} \right)^3 \cdot U_s^{\,2} \frac{1}{F_{Ds}} \tag{14.22}$$

Since

$$\dot{M}_s = \alpha_s \rho_s U_s \tag{14.23}$$

Equ. (14.22) can be further expressed as:

$$\beta' = \frac{4(1-e^2)}{\sqrt{3\pi}} \dot{M}_s \alpha_s \left(\frac{A_s}{d_s}\right)\left(\frac{\sqrt{\overline{U_s'^2}}}{\overline{U_s}}\right)^3 \cdot U_s \frac{1}{F_{Ds}} \tag{14.24}$$

For a solid particle in a swarm of particles, the drag force on the particle can be expressed by

$$F_{Ds} = \frac{18\mu}{d_s^2} C_D (U_g - U_s) \tag{14.25}$$

For a solid particle in an infinite large space, the drag force on the particle can be expressed by

$$F_{Ds0} = C_{D0} \frac{\pi}{8} \frac{\mu^2}{\rho_g} \mathrm{Re}^2 \tag{14.26}$$

Hence, substituting Equs. (14.25) and (14.26) into Equ. (14.24), one can get:

$$\beta' = \frac{2(1-e^2)}{9\sqrt{3\pi}} \frac{\left(\frac{\sqrt{\overline{U_s'^2}}}{\overline{U_s}}\right)^3}{\left(\frac{C_D}{C_{D0}}\right)\mu} \dot{M}_s d_s \frac{U_s}{U_g - U_s} \tag{14.27}$$

where $\frac{C_D}{C_{D0}}$ is the correction factor due to the existence of neighboring particles, and is a function of particle distance (center to center) l', and particle diameter d_s (Zhu *et al.*, 1994; Liang *et al.* 1996):

$$\frac{C_D}{C_{D0}} = 1 - 0.4 \exp\left(-0.7 \frac{l'}{d_s}\right) \tag{14.28}$$

where

$$\frac{l'}{d_s} = \sqrt[3]{\frac{\left(\frac{\pi}{6}\right)}{\alpha_s}} - 1 \tag{14.29}$$

Hence, substituting Equ. (14.28) into Equ. (14.27), the power fraction from the axial pressure gradient due to inter-particle interactions β' can be expressed by:

$$\beta' = \left[1 - 0.4 \exp\left(-0.7 \cdot \sqrt[3]{\frac{\pi/6}{\alpha_s}} \right) \right] \cdot \frac{4(1-e^2)}{9\sqrt{3\pi}} \dot{M}_s \frac{d_s}{\mu} \left(\frac{\sqrt{U_s'^2}}{\overline{U_s}} \right)^3 \cdot \frac{U_s}{U_g - U_s} \qquad (14.30)$$

CHAPTER 15

RESULTS AND DISCUSSION

15.1 Numerical Solver Algorithm

The numerical solver algorithm is shown in Figure 15.1, a FORTRAN 90 code is developed to numerically solve the sample problem as shown in Appendix A, and the sample input file is shown in Appendix B.

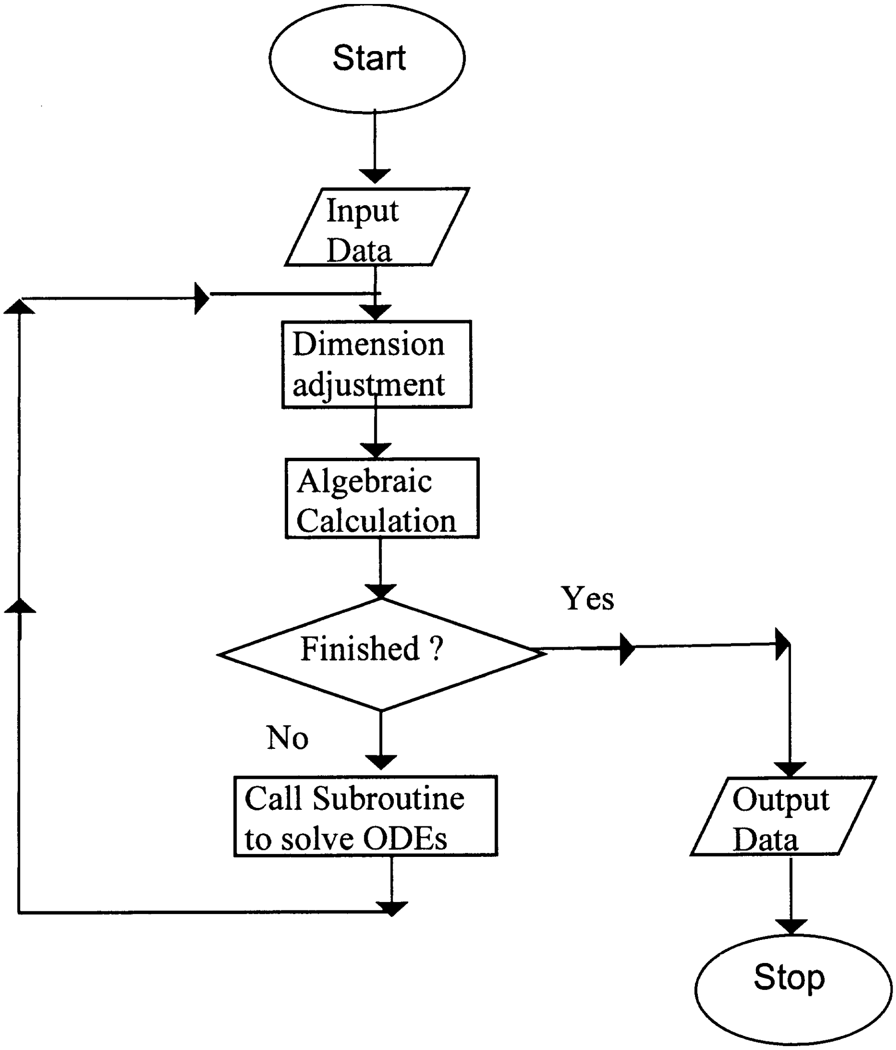

Figure 15.1 Numerical solver algorithm.

15.2 Distribution of Solid Concentration

A typical modeling result of axial distributions of solids concentration in the core and annulus regions is given in Figure 15.2, and the parameters of a sample calculation are shown in Table 15.1.

Table 15.1 Parameters for a sample calculation.

Constant C in Equ. 14.14	0.5
Restitution coefficient	0.9
Calculated bed height from the distributor	0.0 m – 1.0 m
Gas velocity	1.0 m/s
Solid feeding rates	1.0 kg/m^{2}s 2.0 kg/m^{2}s 3.0 kg/m^{2}s
Bed diameter	10.2 cm
Density of solid particles	1.4*10^3 kg/m^3
Viscosity of gas	1.5*10^{-5} Pa/s
Density of gas	1.2 kg/m^3
Initial solid concentration In wall region	0.3
Solid particle diameter	60.0 μm

As shown in Figure 15.2, at a constant gas velocity Ug = 1.0 m/s, at different solid feeding rates of 1.0 kg/m^{2}s, 2.0 kg/m^{2}s, and 4.0 kg/m^{2}s, the axial solid concentrations for three cases for both the core and annulus regions show different patterns.

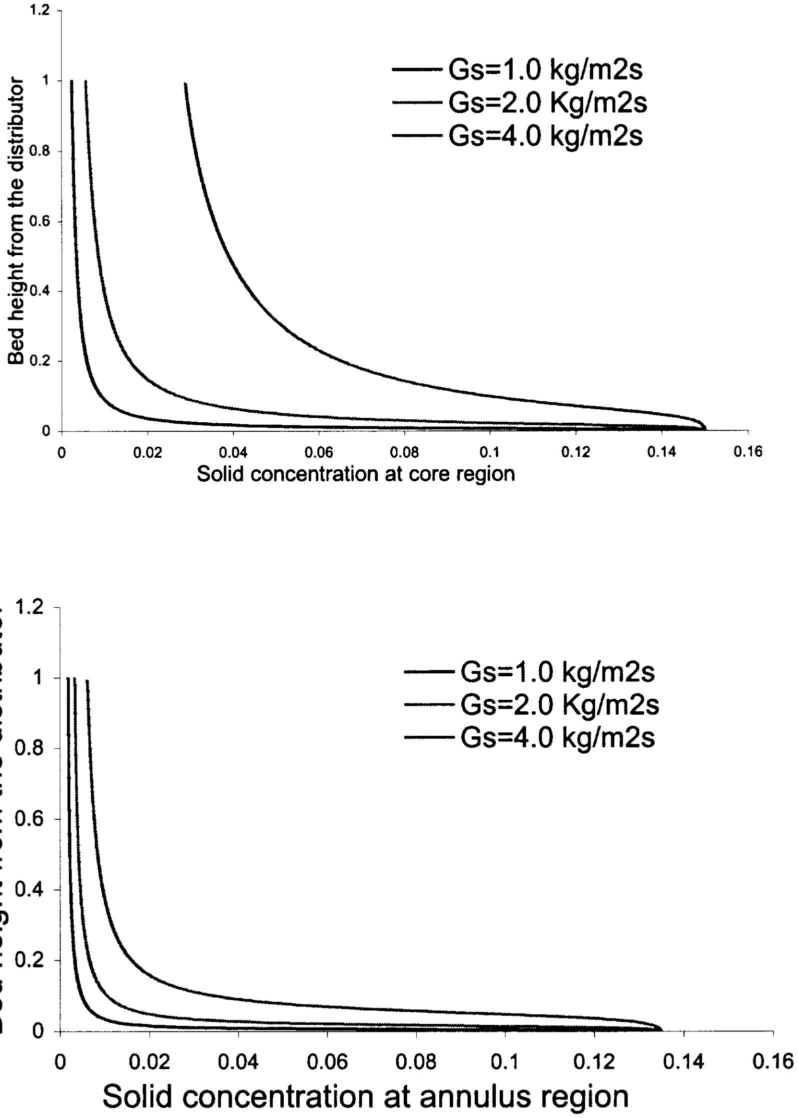

Figure 15.2 Axial distributions of solid concentration in core (upper figure) and annulus (lower figure) regions in a developing regime of CFB (FCC particles, U_{gas}=1.0 m/s).

It is found that, at low solids circulating rate, the solids concentrations in both the core and annulus regions monotonically decrease along the riser. However, at a high solids circulating rate and at a moderate gas flow rate, the solids concentration in the core region near the bottom of a CFB riser can be very dense, and the gas velocity in the core region would be very low compared to that in the annulus, which leads to a very slow solids acceleration in the core. Therefore it is possible that the strong radial solids flow from the wall could overbalance the solids dilution by acceleration, resulting in a net increase of solids in the local core region. This net increase in local solids holdup near the bottom of riser at a high solids circulation rate and low gas flow rate may trigger the instability of the solid suspension, which leads to bed collapse. This bed collapse phenomenon has been observed via ECT measurements by Du et al. (2004) and can be modeled using our proposed model.

15.3 Concluding Remarks

A mechanistic model has been proposed to interpret the core-annulus-wall flow structure in CFB risers. This structure originates from the wall region mixing of a down flow of solids from top section of a riser and an upward flow of solids near the bottom of the riser. As a result, the solids transport distributions are highly non-uniform both in the axial and radial directions. An analytical model is developed to calculate the solids holdup in this developing regime, which accounts for effects of solids acceleration and energy dissipation by solids collisions.

15.4 Limitation of this Study and Future Research Directions

Although some innovative work has already been done in this study, more research work needs to be done to fully understand the recently discovered core-annulus-wall flow structure in CFB risers. More experimental measurements, especially more information on solid concentration, particle and gas velocities, and pressure drop distribution, both in the longitudinal and radial directions, and under different operation conditions would be beneficial to further understanding of the mechanism. More detailed modeling work, including a more accurate physical description is also necessary. Finally, 3D real time numerical simulation could also provide valuable information.

CHAPTER 16

SUMMARY AND FUTURE STUDIES

16.1 Summary

A comprehensive study of fluidization of nanoparticle agglomerates with and without an external force field has been performed in this study. Both experiments and a theoretical analysis have been carried out to investigate the fundamental mechanisms of a gravity-driven fluidized bed of nanoparticle agglomerates without any additional external forces. Extensive experiments have also been conducted to investigate the effects of coupling aeration with an external force field, including sound waves and a magnetic field, on the fluidization of nanoparticle agglomerates.

In the experimental study of fluidization of nanoparticle agglomerates, a laboratory-scaled fluidized bed system with sound excitation and magnetic excitation has been built, and eleven different types of nanoparticles have been tested. A laser/lamp-light assisted visualization system have been developed, which enables capturing images of fluidized nanoparticle agglomerates near the fluidized bed surface for the purpose of size measurement. All the experiments have been performed with both APF and ABF nanoparticles. Both sound waves and an oscillating magnetic field to assist in the fluidization have been investigated, and parametric studies have been performed on various parameters such as sound intensity and frequency, magnetic field intensity and frequency, and mass ratio of magnets to nanoparticles.

A simple and effective method has been derived to estimate the average size of the agglomerates and the bed voidage around the agglomerates which can then be used in to determine the minimum fluidization velocity, pressure drop and other pertinent variables of the fluidization process. In addition, a simple model has also been derived to estimate the drag force correction factor for the hydrodynamic force on a highly porous floc-like agglomerate in a swarm of other similar agglomerates.

Based on the fractal hollow structure and other favorable properties, it appears that snanoagglomerates can perform as well (high collection efficiency) as fiber-based HEPA filters, but with a much higher dust loading capacity. In this study, a set of experiments using fractal nanoaprticle agglomerates has been performed to test the filtration of submiron solid particles and liquid droplets.

In addition, the formation mechanisms of the newly discovered core-annulus-wall structure in a circulating fluidized bed riser has been described, and an analytic model has been developed for quantifying this type of flow structure in the developing regime, especially the solids concentration in the core region. An evaluation of the effect of solids acceleration on the solid holdup measurement that is determined from pressure gradient measurements in a CFB riser has also been proposed.

16.2 Major Contribution and Findings

16.2.1 Conventional Fluidization of Nanoparticle Agglomerates

The major contributions and finding of conventional fluidization of nanoparticle agglomerates are:

(1) Highly porous nanoparticle agglomerates exhibit two distinct fluidization behaviors, APF (smooth fluidization without bubbles at minimum fluidization) and ABF (bubbles observed at minimum fluidization).

(2) An in-situ optical measurement method is used to measure the agglomerate sizes on the fluidized bed surface, and experimental results show that typical sizes of the nanoparticle agglomerates are within the range of 200 to 600μm.

(3) For APF nanoparticles, a model based on the initial bed voidage around the agglomerates and the Richardson-Zaki equation was used to predict the mean agglomerate size in the fluidized bed, and the results agree fairly well with the experimental measurements.

(4) The Ergun equation, based on the agglomerate size and voidage at minimum fluidization predicted by the model, can be used to calculate the minimum fluidization velocity for APF nanoparticle agglomerates. The calculated results agree very well with the experimental results.

(5) A model for a permeable sphere in a swarm of permeable spheres (see Appendix) shows that fluidized APF nanoparticle agglomerates (at large ε_g) can be treated as solid particles for hydrodynamic analysis with little error.

(6) A classification criterion based on the value of a combination of dimensionless groups to differentiate between particulate and bubbling fluidization for classical solid fluidized particles appears to also predict remarkably well whether nanoparticles will behave as APF or ABF.

16.2.2 Sound Assisted Fluidization of Nanoparticle Agglomerates

The major contributions and finding of sound assisted fluidization of nanoparticle agglomerates are:

1. The external forces induced by the sound field can overcome the cohesive van der Waals forces of nanoparticle agglomerates so that large nano-agglomerates break into smaller agglomerates, which can be fluidized smoothly and homogeneously with negligible elutriation.
2. For the APF nanoparticles, with the assistance of a sound field, the minimum fluidization velocity can be significantly reduced, the fluidization quality can be significantly improved, and bed expansion increased.
3. For the ABF nanoparticles, with the assistance of a sound field, the minimum fluidization velocity also can be reduced, the fluidization quality can be improved, and the bed expansion also increased.
4. Both the bed expansion and the bubble characteristics are strongly dependent on the sound frequency. Within a certain range of the sound frequency, typically from 200 to 600 Hz, bubbling fluidization occurs. However sound has almost no impact on the fluidization, when the sound frequency is extremely high, above 2000 Hz.
5. Both the bed expansion and the bubble characteristics are strongly dependent on the sound pressure level. A relatively high sound pressure level (such as 115 dB) is needed to initiate the fluidization.

(6) The direct measurement of the agglomerate size has also been performed; with the assistance of sound, the average diameter of agglomerates can be significantly reduced.

16.2.3 Magnetic Assisted Fluidization of Nanoparticle Agglomerates

The major contributions and finding of magnetic assisted fluidization of nanoparticle agglomerates are:

(1) Silica nanoparticle agglomerates can be easily and smoothly fluidized with the assistance of magnetic particles in an oscillating magnetic field. Due to a significant reduction in the minimum fluidization velocity with magnetic assistance, both elutriation of nanoparticle agglomerates and gas bypass in the form of bubbles is greatly reduced.

(2) With magnetic excitation, hard (larger than 500 μm) agglomerates change their fluidization pattern from no fluidization to agglomerate particulate fluidization (APF) with large bed expansion.

(3) The minimum fluidization velocity of an 80% soft (smaller than 500 μm) and 20% hard agglomerate (80/20) mixture can also be significantly reduced, resulting in easier and more uniform fluidization.

(4) Magnetic excitation results in fragmentation of the agglomerates, so that the mean agglomerate size is significantly reduced.

(5) The ability to fluidize these fumed silica nanoparticle agglomerates depends on the mass ratio of magnets to nanoparticles, the intensity of the magnetic field, and the frequency of the magnetic field.

(6) For ABF nanoparticles (Degussa Aerosil® TiO_2 P25, and Degussa Aerosil® SiO_2 A90), there is no improvement observed by introducing magnetic excitation.

16.2.4 Filtration of Submicron Particles in Gas Stream Using Fractal Nanoparticle Agglomerates

The major contributions and findings in the filtration of submicron particles in gas stream using fractal nanoparticle agglomerates are:

(1) Fractal hierarchical structured nanoagglomerates, such as fumed silica Degussa Aerosil® A300, can be used as a substitute filter media in a HEPA filter, to remove submicron sized solid particles and liquid droplets.

(2) Nanoagglomerate-based HEPA filters can absorb a large amount of submicron particles, even as much as 8 times its own weight before becoming saturated, showing a much higher capacity than fiber-based HEPA filters.

(3) Nanoagglomerate-based HEPA filters result in low penetration for MPPS as for the two filters tested, at an acceptable pressure drop level, showing much higher efficiency (lower penetration) than a fiber-based HEPA filter. Both aerosol number and size measurements and SEM images support this observation.

(4) Nanoagglomerate-based HEPA filters work as a deep bed filter, rather than a cake-forming surface filter such as traditional fiber-based HEPA filters.

16.2.5 Modeling of the Core-Annulus-Wall Structure in Circulating Fluidized Bed Riser

The major contributions and findings in the modeling on the core-annulus-wall structure in circulating fluidized bed riser are:

(1) A new mechanistic model has successfully developed to interpret the core-annulus-wall flow structure in CFB risers. This structure originates from the wall region mixing of a down flow of solids from the top section of a riser and the upward flow of solids near the bottom of the riser. As a result, the solids transport distributions are highly non-uniform both in the axial and radial directions.

(2) An analytical model has also been developed to calculate the solids holdup in the developing regime, which accounts for effects of solids acceleration and energy dissipation by solids collisions.

16.3 Suggested Future Research Directions

The fundamental mechanism of either fluidization of nanoparticle agglomerates, especially with external excitations, and the filtration of submicron particles in gas stream are far from being fully understood. Also, complete clarification of the mechanism of the core-annulus-wall structure in circulating fluidized bed riser requires further study. Hence, in this section, several research topics are suggested to further understand these phenomena and provide more solid mechanistic explanations.

16.3.1 Conventional Fluidization of Nanoparticle Agglomerates

There are lots of unknowns in the study of conventional fluidization of nanoparticle agglomerates, which need extensive experimental investigations and more modeling efforts. One very much desired piece of information is the mechanism of agglomeration and de-agglomeration of nanoparticles, which can determine the size of stable fluidizing agglomerates and therefore provide information on the required external forces necessary to break up the agglomerates.

More experiments to test different types of nanoparticle agglomerates are recommended, which may provide more information on the fluidization patterns. For example, fluffy nano carbon black which could not be fluidized even with external force field assistance.

Finally, models to predict conventional fluidization of nanoparticle agglomerates, especially sub-models of inter-agglomerate and inter-sub-agglomerate hydrodynamic force, and the hydrodynamic force among primary nanoparticles, are definitely desired.

16.3.2 Sound and Magnetic Assisted Fluidization of Nanoparticle Agglomerates

More comprehensive experimental studies on effect of external force fields such as sound waves and magnetic field assistance on the fluidization of nanoparticle agglomerates are desired, and more types of nanoparticles could be tested in these experiments. And at the same time, more parametric experimental studies could be applied. For example why are large bubbles observed when the sound frequency is between 200 and 600 Hz , and no bubbles are observed below and above these frequencies.

The other suggested research topic is to study the mechanism of external force field excitations on fluidization of nanoparticles, and additional modeling based on fractal analysis and numerical simulations probably can provide useful information.

16.3.3 Filtration of Submicron Particles in Gas Stream Using Fractal Nanoparticle Agglomerates

Filtration of submicron particles using fractal nanoparticle agglomerates is a completely new area, and this study only performed some very preliminary qualitative experimental tests. Hence, to extend the research on this topic, there are lots of possible research directions, which may significantly influence the results in this area, such as the selection of optimum filter media properties and theoretical modeling.

Variables such as the size and specific surface area of the primary particles, surface treatment, hydrophobicity and hydrophilicity, porosity, mean size of the large agglomerates, subagglomerates (SA) and primary agglomerates (PA), and the selection of different types of nanoparticles will significantly influence the absorption efficiency and capacity for submicron particles. More experimental studies should be performed to optimize those parameters according to different target aerosol particles.

In order to predict the single particle collection efficiency and penetration of MPPS particles and be able choose the properties of fractal nanoagglomerates which will provide the best results, with respect to penetration, pressure drop and capacity, theoretical modeling needs to be developed.

16.3.4 Modeling on Core-Annulus-Wall Structure in Circulating Fluidized Bed Riser

With regard to the recently discovered core-annulus-wall flow structure in CFB risers, although many new important results have already been achieved in this study, more research work needs to be done. More detailed modeling work, including a more accurate physical description of the phenomenon is desired to further understand the mechanism of formation of this structure.

More experimental measurements, especially more information on solid concentration, particle and gas velocities, and pressure drop distribution, both in the longitudinal and radial directions, and under different operating conditions would be beneficial to e further understanding of the mechanism. Finally, 3D real time numerical simulation will also provide valuable information.

APPENDIX A

NUMERICAL SOLVER CODE

```
$DEBUG
PROGRAM CHOKING
        USE MSIMSL
        IMPLICIT    NONE
        INTEGER(KIND=4)::MXPARM, N
        PARAMETER  (MXPARM=60, N=4)

! SPECIFICATIONS FOR LOCAL VARIABLES
        INTEGER(KIND=4)::IDO, ISTEP,NNN, KSTEP,JSTEP
        REAL(KIND=8)::PARAM(MXPARM), Z, ZEND, TOL, Y(N),DZ
        REAL(KIND=8)::PI,G,M,BACKMIXING
        REAL(KIND=8)::GSDOT,HEIGHT,D,ROLG,ROLS,ALFASW0

        REAL(KIND=8)::TENSITY,E,G0,KAPA,EITA,RER,L2,KESI1,GGDOT,DEL
    &   TA,C1,USW2,ALFASW,UPT,USW,C2,C3,T1,T2

        REAL(KIND=8)::US,UGA,UGC,UGW,UG,DS,MUG,ALFASA,KESI,A,AW,
    &   AC,AA,R,RC,RA
        REAL(KIND=8)::ALFAS8,UG8
        PARAMETER  (PI=3.1415926,G=9.80665,M=1.0,BACKMIXING=0.333)
        PARAMETER
    &   INTENSITY=0.1,E=0.9,G0=1.0,KAPA=0.002,EITA=0.999998,L2=1.0,
    &   KESI1=0.3333,C1=0.5,C2=0.9,C3=1.0)


! SPECIFICATIONS FOR SUBROUTINES

       COMMON ROLG,ROLS,US,UGA,UGC,UGW,UG,DS,MUG,ALFASA,KESI
       COMMON A,AW,AC,AA,R,RC,RA,ALFASW0
       COMMON ISTEP,KSTEP,GGDOT,GSDOT,USW2,ALFASW,UPT,USW
       COMMON JSTEP,ALFAS8,UG8

        EXTERNAL  FCN


!  Set initial conditions
        Z = 0.0

        OPEN (7,FILE="D:\CHOKING\CODES\MODEL2\input.txt",
   &    STATUS="OLD")
```

```
        READ (7,*) UG,GSDOT,HEIGHT,D,ROLG,MUG,ROLS,DS,ALFASW0
        CLOSE (7)


!       Dimension adjustment
        D = D*0.0254
        DS = DS*1.0E-6
        R = D/2
        A = PI*R*R
!       End of dimension adjustment


!   CALCULATING INITIAL CONDITIONS        (REGION I)

        GGDOT = UG*ROLG
        RER = R*(GSDOT+GGDOT)/(MUG/(1-
        ALFASW0)**2.65+0.78*TENSITY*GSDOT*ALFASW0*DS)
        DELTA = R*70.0/(0.03325*RER**1.75)**0.5

        RA = R-DELTA
        AW = PI*R*R - PI*RA*RA
        KESI = AW/A
        AA = (A-AW)/(1+KESI1)

        AC = A-AW-AA
        RC = (AC/PI)**0.5

!        CALCULATING INITIAL CONDITIONS  (REGION II)

        Y(3) = ALFASW0*C1
        ALFASA = Y(3)*C2
        Y(1) = GSDOT*A/ROLS/(C3*ALFASA*AA+Y(3)*AC)
        Y(2) = Y(1)*C3
        UGW = 0
        T1 = ROLG*(1.0-ALFASA)*AA + ROLG*(1.0-Y(3))*AC*ALFASA/Y(3)
        T2 = GGDOT*A - ROLG*(1.0-Y(3))*AC*Y(1)+ROLG*(1.0-
        Y(3))*AC*ALFASA/Y(3)*Y(2)
        UGA = T2/T1

        UGC = Y(1) + ALFASA/Y(3)*(UGA-Y(2))

        Y(4) = 1.01E5

        ALFASW = ALFASW0
        USW2 = BACKMIXING * GSDOT/ROLS/ALFASW
        USW = 0.0
```

```
        UPT = ROLS*DS*DS*G/18.0/MUG

        UG8 = UG*A/(A-AW)
        ALFAS8 = GSDOT/ROLS/(UG8-UPT)


!  Set error tolerance
        TOL=1.0E-9
        DZ=1.0E-3
        NNN=INT(HEIGHT/DZ)

!  Set PARAM to default
        CALL DSET (MXPARM, 0.0, PARAM, 1)

! Select absolute error control
        PARAM(1)= 5.0E-4
        PARAM(2)= 0
        PARAM(3)= 2
        PARAM(4)= 2000000
        PARAM(10) = 1.0




!  Print header
         IDO = 1
         ISTEP = 0

         OPEN(12,FILE="D:\CHOKING\CODES\MODEL2\OUTput.txt")
         WRITE(12,*)'  Z  ','  ALFASC ','  ALFASA ','  ALFASW ',' USC    ',
     &   '   USA  ',' USW  ',' UGC   ',' UGA ',' P    ','    RC    ','  RA  ',
     &   '  KESI  '

         WRITE (12,'(13E10.4)') ZEND, Y(3), ALFASA, ALFASW, Y(1), Y(2), USW,
     &   UGC, UGA, Y(4), RC/0.0254, RA/0.0254, KESI

          OPEN (13,FILE="D:\CHOKING\CODES\MODEL2\RESULT.txt",
&         STATUS="OLD")
          WRITE(13,*)'  Z  ','  ALFASC ','  ALFASA ','  ALFASW ',' USC    ',
&         '   USA  ',' USW  ',' UGC   ',' UGA ',' P    ','    RC    ','  RA  ',
&         '  KESI  '


 10       CONTINUE
          JSTEP = 1
```

```
          KSTEP = 1
          ISTEP = ISTEP + 1
          ZEND = ISTEP*DZ
          WRITE(*,*)'DZ',DZ,'ISTEP',ISTEP

          CALL DIVPRK (IDO, N, FCN, Z, ZEND, TOL, PARAM, Y)

           IF ( ISTEP .LE. NNN)  THEN
           WRITE (12,'(13E11.4)') ZEND, Y(3), ALFASA, ALFASW, Y(1), Y(2),
&          USW, UGC, UGA, Y(4), RC/0.0254, RA/0.0254, KESI
           WRITE (13,'(13E11.4)') ZEND, Y(3), ALFASA, ALFASW, Y(1), Y(2),
&          USW, UGC, UGA, Y(4), RC/0.0254, RA/0.0254, KESI

           IF (  (HEIGHT-ZEND) .LE. (2*DZ) )THEN
                          GO TO 20
           END IF

           IF (ISTEP .EQ. NNN) IDO = 3
           GO TO 10

           END IF

20         CONTINUE

            CLOSE(13)
            CLOSE(12)

     END




         SUBROUTINE FCN (N, Z, Y, YPRIME)

         IMPLICIT NONE
         INTEGER(KIND=4)::N,KSTEP,ISTEP,JSTEP
         REAL(KIND=8):: Z, Y(N),YPRIME(N)
         REAL(KIND=8)::PI,G,M,BACKMIXING
         REAL(KIND=8)::GSDOT,ROLG,ROLS,ALFASW0,USW
         REAL(KIND=8)::TENSITY,E,G0,KAPA,EITA,L2,KESI1,GGDOT,C1,USW2
&        ,MSWDOT,ALFASW,UPT,C2
         REAL(KIND=8)::US,UGA,UGC,UGW,UG,DS,MUG,ALFASA,KESI,A,AW,
&        AC,AA,R,RC,RA
         PARAMETER  (PI=3.1415926,G=9.80665,M=1.0,BACKMIXING=0.333)
```

```
          REAL(KIND=8):: CDRATIOA,CDRATIOC,F0MAXA,F0A,F0MAXC,F0C,
     &    MSCDOT,F1,F2,DD,KA,KC
          REAL(KIND=8):: T1,T2,T3,T4
          REAL(KIND=8)::ALFAS8,UG8

          PARAMETER  (TENSITY=0.1,E=0.9,G0=1.0,KAPA=0.002,
     &    EITA=0.999998  ,L2=1.0,KESI1=0.3333,C1=0.5,C2=0.9)

          COMMON ROLG,ROLS,US,UGA,UGC,UGW,UG,DS,MUG,ALFASA,KESI,
     &    A,AW,AC,AA,R,RC,RA,ALFASW0
          COMMON ISTEP,KSTEP,GGDOT,GSDOT,USW2,ALFASW,UPT,USW,
     &    JSTEP,ALFAS8,UG8

!***** UNKNOWNS:

          KA = 0
          KC = 0
          DD = 0

          MSWDOT = AW*ALFASW*USW2*ROLS*(1-Z/L2)/PI/RA/L2

          MSCDOT = MSWDOT*(1.0-
     &    ALFASA*AA*Y(2)/(ALFASA*AA*Y(2)+Y(3)*AC*Y(1)))

          USW = USW2 * Z /L2

          IF (ALFASA .LT. 0.15) THEN
                CDRATIOA =  1.0
                ELSE
                CDRATIOA = -10.0/7.0*ALFASA+8.5/7.0
          ENDIF

          IF (Y(3) .LT. 0.15) THEN
                CDRATIOC =  1.0
                ELSE
                CDRATIOC = -10.0/7.0*Y(3)+8.5/7.0
           ENDIF

           F0MAXC = (1.0-UPT/CDRATIOC/(UGC-Y(1)))/0.15/GSDOT/(DS/MUG)
     &     /(1-E*E)
           F0C = F0MAXC*EITA

           T2 = MSWDOT*2*PI*RA*(USW-Y(2))/Y(3)/Y(2)/ROLS/AA
           F0MAXA = (1.0-UPT*(1.0-T2*Y(2)/G)/CDRATIOA/(UGA-
     &     Y(2)))/0.15/GSDOT/(DS/MUG)/(1-E*E)
           F0A = F0MAXA*EITA
```

```
!*****  ODE EQUATIONS (1) USC (2) USA  (3) ALFASC, (4) P

        T1 = 1+4.0*Y(3)*G0+7.8*Y(3)**1.3333*G0*TENSITY
        T2 = MSCDOT*2*PI*RC*(Y(2)-Y(1))/Y(3)/Y(1)/ROLS/AC
        T3 = 18.0*MUG/ROLS/DS/DS*CDRATIOC*(UGC/Y(1)-1.0)
        T4 = 1.0 -0.15*GSDOT*DS/MUG*(1-E*E)*F0C*((Y(3)-
&       ALFAS8)/(C1*ALFASW0-ALFAS8))**KAPA

        F1 = (T2+T3*T4 - G/Y(1) )/T1

        IF( JSTEP .LE. 1) THEN
        WRITE (13,*) 'F1',F1,'   T1',T1,'   T2',T2,'   T3',T3,'  T4',T4,'  T3*T4 –
&       G/Y(1)',T3*T4 - G/Y(1)
        ENDIF

        YPRIME(1) = F1

        T1 = 1+4.0*ALFASA*G0+7.8*ALFASA**1.3333*G0*TENSITY
        T2 = MSWDOT*2*PI*RA*(USW-Y(2))/ALFASA/ROLS/AA/Y(2)
        T3 = 18.0*MUG/ROLS/DS/DS*CDRATIOA*(UGA/Y(2)-1.0)
        T4 = 1.0 -0.15*GSDOT*DS/MUG*(1-E*E)*F0A*((ALFASA-
&       ALFAS8)/(C1*ALFASW0*C2-ALFAS8))**KAPA

        F2 = (T2+T3*T4 - G/Y(2) )/T1

        IF( JSTEP .LE. 1) THEN
        WRITE (13,*) 'F2',F2,'   T1',T1,'   T2',T2,'   T3',T3,'   T4',T4
        ENDIF

        YPRIME(2) = F2

        T1 = MSCDOT*2*PI*RC/ROLS/AC/Y(1)
        T2 = Y(3)/Y(1)*F1
        IF( JSTEP .LE. 1) THEN
        WRITE (13,*) 'Y3',T1-T2,'   T1',T1,'   T2',T2
        ENDIF

        YPRIME(3) = T1 - T2

        T1 =  GSDOT*A/ROLS
        T2 = AW*ALFASW*USW*(2*Z/L2-Z*Z/L2/L2)
        T3 = -Y(3)*Y(1)*AC
        ALFASA = 1.0/Y(2)/AA*(T1+T2+T3)
```

```
        T1 = ROLG*(1.0-ALFASA)*AA + ROLG*(1.0-
     &  Y(3))*AC*ALFASA/Y(3)*CDRATIOA/CDRATIOC
        T2 = GGDOT*A - ROLG*(1.0-Y(3))*AC*Y(1)+ROLG*(1.0-
     &  Y(3))*AC*ALFASA/Y(3)*CDRATIOA/CDRATIOC*Y(2)
        UGA = T2/T1

        UGC = Y(1) + ALFASA/Y(3)*CDRATIOA/CDRATIOC*(UGA-Y(2))

        YPRIME(4) = -Y(3)*18.0*MUG/DS/DS*CDRATIOC*(UGC-Y(1))
        IF( JSTEP .LE. 1) THEN
        WRITE (13,*) 'Y4',  -Y(3)*18.0*MUG/DS/DS*CDRATIOC*(UGC-Y(1))
        ENDIF

        IF( JSTEP .LE. 1) THEN
        WRITE(13,*) '   MSWDOT', MSWDOT, '   MSCDOT', MSCDOT, '   USW',
     &  USW
        WRITE(13,*) 'STEP--1'
        WRITE(13,*) 'CDRATIOA',CDRATIOA
        WRITE(13,*) 'CDRATIOC',CDRATIOC
        WRITE(13,*) 'UPT',UPT,'   USC',Y(1),'   UGC',UGC,'   GSDOT',GSDOT
        WRITE(13,*) 'f0mAXC',F0MAXC,'   F0C',F0C
        WRITE(13,*) 'f0mAXA',F0MAXA,'   F0A',F0A
        WRITE(13,*) '   USC', Y(1), '   USA', Y(2), '   ALFASC', Y(3)
        WRITE(13,*) '   ALFASA', ALFASA, '   UGC', UGC,'   UGA',UGA,'
     &  P',Y(4)
        ENDIF

        JSTEP = JSTEP +1

        RETURN
      END
```

APPENDIX B

SAMPLE INPUT FILE

```
1.0
5.0
1.0
4.0
1.2
1.5E-5
1400.0
60.0
0.3
```

REFERENCES

1. Arnaldos, J., Casal, J., Lucas, A., Puigjamer, L.(1985). Magnetically stabilized fluidization: modeling and application to mixtures. Powder Technology; 44, 57-62.

2. Chaouki, J., Chavarie, C., Klvana, D.(1985). Effect of interparticle forces on the hydrodynamic behavior of fluidized aerogels. Powder Technology; 43, 117-125.

3. Chirone, R., Massimilla, L., Russo, S.(1992). Bubbling fluidization of a cohesive powder in an acoustic field. Fluidization VII; 545-553.

4. Chirone, R., Massimilla, L., Russo, S.(1993). Bubble-free fluidization of a cohesive powder in an acoustic field. Chem. Eng. Sci.; 48, (1) 41-53.

5. Chirone, R., Massimilla, L.(1994). Sound-assisted aeration of beds of cohesive solids. Chem. Eng. Sci.; 49, 1185-1194.

6. Chirone, R., Russo, P.(1995). Resonant behavior of cluster-subcluster structures in sound assisted fluidization beds. Fluidization VIII; 389-397.

7. Coury, J. R., Thambimuthu, K. V., Clift, R.(1987). Capture and rebound of dust in granular bed gas filters. Powder Technology; 50(3) 253-265.

8. Davis, R. H., Birdsell, K.H.(1988). Hindered settling of semidilute monodisperse and polydisperserse suspensions. AIChE Journal; 34, 123-129.

9. Du, B., Warsito, W., Fan, L. S.(2004). ECT studies of the choking phenomenon in a gas-solid circulating fluidized bed. AIChE Journal; 50 (7), 1386.

10. El-Halwagi, M.M.(1990). Mathematical modeling of aerosol collection in fluidized-bed filters. Aerosol Science and Technology; 13, 102.

11. Fan, L. S., Zhu, C.(1998). Principles of Gas-solid Flows. Cambridge Series in Chemical Engineering.

12. Fayed, M.E., Otten, L.(1997). Handbook of Powder Science and Technology. Chapman & Hall.

13. Filippov, M.V.(1960). The effect of a magnetic field on a ferromagnetic particle suspension bed. Prik. Magnit. Lat. SSR.;12, 215.

14. Flagen, R.C., Seinfeld, J.H.(1988). Fundamentals of Air Pollution Engineering. Prentice Hall, Englewood Cliffs, NJ.

15. Ganzha, V.L., Saxena, S. C.(1998). Heat-transfer characteristics of magnetofluidized beds of pure and admixtures of magnetic and nonmagnetic particles. International Journal of Heat and Mass Transfer; 41, 209-218.

16. Happel, J.(1958). Viscous flow in multiparticle systems: slow motion of fluids relative to beds of spherical particles. AIChE. Journal; 4, 197-201.

17. Heck, J., Onken, U.(1987). Hysteresis effects in suspended solid particles in bubble columns with and without a draft tube. Chemical Engineering Science; 42, 1211-1212.

18. Herrera, C.A., Levy, E.K.(2001). Bubbling characteristics of sound-assisted fluidized beds. Powder Technology; 119, 229-240.

19. Herrera, C.A., Levy, E.K.(2002). Characteristics of acoustic standing waves in fluidized beds. AIChE Journal; 48 (3), 503-513.

20. Iwadate, Y., Horio, M.(1998). Prediction of agglomerate sizes in bubbling fluidized beds of group C powders. Powder Technology; 100, 223.

21. Jung, J., Gidaspow, D.(2002). Fluidization of nano-size particles. Journal of Nanoparticle Research; 4, 483-497.

22. Levy, E.K., Shnitzer, H., Masaki, T., Salmento, J.(1997). Effect of an acoustic field on bubbling in a gas fluidized bed. Powder Technology; 90, 53-57.

23. Li, H., Hong, R., Wang, Z.(1999). Fluidizing ultrafine powders with circulating fluidized bed. Chemical Engineering Science; 54, 5609-5615.

24. Liang, S.C., Hong, T., Fan, L. S.(1996). Effects of particle arrangements on the drag force of a particle in the intermediate flow regime. Int. J. Multiphase Flow; 22, 285.

25. Liu, Y.A., Hamby, R.K., Colberg, R.D.(1991). Fundamental and practical developments of magnetofluidized bed: A review. Powder Technology; 64, 3-41.

26. Loezos, P. N., Costamgna, P., Sundaresan, S.(2002). The role of contact stresses and wall friction on fluidization. Chemical Engineering Science; 57, 5123-5141.

27. Lu, X., Li, H.(2000). Fluidization of $CaCo_3$ and Fe_2O_3 particle mixtures in a transverse rotating magnetic field. Powder Technology; 107, 66-78.

28. Matsuda, S., Hatano, H., Muramota, T., Tsutsumi, A.(2001). Particle and bubble behavior in ultrafine particle fluidization with high G. Fluidization X Eng. Found.; 501- 508.

29. Matsuda, S., Hatano, H., Tsutsumi, A.(2002). Modeling for size reduction of agglomerates in nanoparticle fluidization. AIChE 2002 Annual Meeting, November 3-8, Indianapolis, Indiana, 138e.

30. Matsuda, S., Hatano H., Tsutsumi, A.(2001). Ultrafine particle fluidization and its application to photocatalytic NO_x treatment. Chemical Engineering Journal; 82, 183-188.

31. Morooka, S., Kusakabe, K., Kobata, A., Kato, Y.(1988). Fluidization state of ultrafine powders. J. of Chem. Eng. of Japan; 2141-2146.

32. Morse, R.D.(1955). Sonic energy in granular solid fluidization. Ind. Eng. Chem., 47 (6), 1170-1175.

33. Nam, C., Pfeffer, R., Dave, R. N., Sundaresan, S.(2004). Aerated vibrofluidization of silica nanoparticles. AIChE Journal; 50, 1776-1785.

34. Neale, G., Epstein, N., Nader, W.(1973). Creeping flow relative to permeable spheres. Chemical Engineering Science; 28, 1865-1874.

35. Pacek, A.W., Nienow, A.W.(1990). Fluidisation of fine and very dense hard metal powders. Powder Technology; 60, 145-158.

36. Peng, Y., Fan, L.T.(1995). Hysteresis in liquid-solid tapered fluidized beds. Chemical Engineering Science; 50, 2669-2671.

37. Penicot, P., Thomas, D., Contal, P., Leclerc, D., Vendel, J.(1999). Clogging of HEPA fibrous filters by solid and liquid aerosol particles: An experimental study. Filtration & Separation; 36 (2), 59-64.

38. Petrovic, D., Posarac, D., Skala, D.(1989). Hysteresis effects of minimum fluidization velocity in a draft tube airlift reactor. Chemical Engineering Science; 44, 996-998.

39. Quevedo, J. A., Nam, C., Dave, R. N., Pfeffer, R.(2004). Fluidization of nanoparticle agglomerates in a rotating fluidized bed, in preparation.

40. Rhodes, M. J., Sollaart, M., Wang, X. S.(1998). Flow structure in a fast fluid bed. Powder Technology; 99, 194.

41. Rosensweig, R.E.(1995). Process concepts using field stabilized two-phase flow. Journal of Electrostatics; 34, 163-187.

42. Rosensweig, R. E., Jerauld, G. R., Zahn, M.(1981). Structure of magnetically stabilized fluidized solids. North-Holland, Amsterdam, 137-144.

43. Russo, P., Chirone, R., Massimilla, L., Russo, S.(1995). The influence of the frequency of acoustic waves on sound-assisted fluidization of beds of fine particles. Powder Technology; 82, 219-230.

44. Saxena, S.C., Ganzha, V. L., Rahman, S.H., Dolidovich, A. F.(1994). Heat Transfer and relevant characteristics of magnetofluidized bed. Adv. Heat Transfer; 25, 151.

45. Sun, G., Chao, Z., Fan, Y., Shi, M.(1999). Hydrodynamic behavior in the bottom region of a cold FCC riser. Circulating Fluidized Bed 6; 179, German.

46. Tardos, G. I., Gutfinger, C., Pfeffer, R.(1979). Triboelectric effects in filtration of small dust particles in a granular bed. I&EC Fundamentals; 18, 433.

47. Tien, C.(1989). Granular filtration of aerosols and hydrosols. Butterworth-Heinemann series in Chemical Engineering. Boston, MA,USA.

48. Tung, T. C. W., Chao, C.Y.H., Burnett, J.(1999). A methodology to investigate the particulate penetration coefficient through building shell. Atmospheric Environment; 33(6), 881-893.

49. Wang, Y., Gu, G., Wei, F., Wu, J.(2002). Fluidization and agglomerate structure of SiO_2 nanoparticles. Powder Technology; 124, 152-159.

50. Wang, Y., Wei, F., Jin, Y., Luo, T.(2000). Agglomerate particulate fluidization and E-particles. Proceedings of the Third Joint China/USA Chemical Engineering Conference (CUChE-3), 12-006, Beijing, China.

51. Wang, Y., Wei, F., Yu, H., Gu, G.(2002). The large-scale production of carbon nanotubes in a nano-agglomerate fluidized-bed reactor. Chemical Physics Letters; 364, 568-572.

52. Wang, Z., Kwauk, M., Li, H.(1998). Fluidization of fine particles. Chemical Engineering Science; 55, 377-395.

53. Wu, R. M., Lee, D. J.(1998). Hydrodynamic drag force exterted on a moving floc and its implication to free-settling tests. Water Research; 32,760-768.

54. Wu, R. M., Lee, D. J.(2001). Hydrodynamic drag on non-spherical floc and free-settling tests. Water Research; 35, 3226-3234.

55. Wu, W. Y., Navada, A., Saxena, S. C.(1997). Hydrodynamic characteristics of a magnetically stabilized air fluidized bed of an admixture of magnetic and non-magnetic particles. Powder Technology; 90, 39-46.

56. Yu, Q., Quevado, J., Pfeffer, R., Dave, R., Zhu, C.(2005). Enhanced Fluidization of Nanoparticles in an Oscillating Magnetic Field. AIChE Journal; 51, 1-9.

56. Zhou, T., Li, H.(1999). Estimation of agglomerate size of cohesive particles during fluidization. Powder Technology; 101, 57-62.

57. Zhou, T., Li, H.(2002). Force balance modeling for agglomerating fluidization of cohesive particles. Powder Technology; 111, 60-65.

58. Zhu, C., Liang, S. C., Fan, L. S.(1994). Particle wake effects on the drag force of an interactive particle. Int. J. Multiphase Flow; 20, 117.

59. Zhu, C., Liu, G., Yu, Q., Pfeffer, R., Dave, R. N., Nam, C.(2004). Sound assisted fluidization of nanoparticle agglomerates. Powder Technology; 141, 119-123.

60. Zhu, C., Yu, Q., Pfeffer, R., Dave, R. N.(2005). Gas fluidization characteristics of nanoparticle agglomerates. AIChE Journal; 51, 426-439.